Investigating human grid-cell-like representations and path integration in the context of cognitive aging

Dissertation

zur Erlangung des akademischen Grades

doctor rerum naturalium
(Dr. rer. nat.)

genehmigt durch die Fakultät für Naturwissenschaften
der Otto-von-Guericke Universität Magdeburg

von **Mag. rer. nat. Matthias Stangl**
geboren am 13.9.1984 in Rottenmann (Österreich)

Gutachter: Prof. Dr. Thomas Wolbers
Asst. Prof. Arnold Bakker, Ph.D.

eingereicht am 19. Juni 2018
verteidigt am 17. Oktober 2018

Gewidmet meinen Eltern

ACKNOWLEDGEMENTS

First of all, I would like to thank my supervisor Thomas Wolbers for his support and guidance throughout the last years. Thank you very much for giving me the chance to work in such an excellent research environment, to pursue my scientific interests, and to learn from both your experience and your exceptional research skills.

Next, I want to thank my dear labmates and friends from the Aging & Cognition Research Group of the DZNE Magdeburg. Most notably, I thank Jon Shine, Paula Vieweg, Nadine Diersch, Esther Kühn, and Martin Riemer (aka "The Mensa Gang") for all their support and for both useful and useless discussions about research and other (un-)important things in life. Many thanks also to Ruojing Zhou, not only for being a wonderful office buddy but also a great climbing partner. Moreover, I want to thank Anett Kirmeß for her help with administrative matters, as well as Asema Hassan and Johannes Achtzehn for their invaluable programming work.

Over the past years, many people also helped me with project administration, participant recruitment, and data acquisition: Renate Blobel, Caroline Dietrich, Viktoria Friesen, Mareen Hanelt, Susann Hantzsche, Patrick Hauff, Karin Huber, Marko Kirbach, Mandy Knoll, Svende Kübler, Claudia Marx, Swantje Pertersen, Mona Reißberg, Christin Ruß, Denise Scheermann, Fabian Schmidt, and Franziska Schulze. Thank you very much for your strenuous efforts. I would not have been able to finish my projects without your help.

I also thank all my collaborators and colleagues from the IKND Magdeburg (David Berron and Emrah Düzel), the University Clinic Magdeburg (Claus Tempelmann), the Max-Planck-Institute Tübingen (Tobias Meilinger), the University College London (Julio Acosta-Cabronero), and the University of Texas at Austin (Ingmar Kanitscheider and Ila Fiete), for enlightening discussions and fruitful collaborative work. A special thanks goes to Ingmar Kanitscheider for his patience in answering all of my countless mathematical and computational modeling questions.

Finally, I want to thank all of my friends and my family for their endless support and for reminding me of what really counts in life.

ABSTRACT

Grid cells in the entorhinal cortex are a central component of the brain's spatial navigation circuit. They are largely thought to support the continuous tracking of one's position in space by integrating self-motion cues, a function called path integration. Analyzing the putative firing of grid cells (i.e., grid-cell-like representations) in human neuroimaging data, however, is a non-trivial endeavor, given the methodological complexity and the absence of standard software tools for this analysis. In Project A of this thesis, we therefore developed the Grid Code Analysis Toolbox (GridCAT), a MATLAB-based open-source software for the automated analysis of human grid-cell-like representations in functional magnetic resonance imaging (fMRI) signals, and made this software openly available to the neuroscience community. In Project B of this thesis, we then applied the GridCAT to fMRI data from young and older adults, in order to investigate age-related changes in grid-cell-like representations. We found that grid-cell-like representations in the entorhinal cortex were compromised in old age, and this effect was mainly driven by a reduced stability of grid orientations over time. Building on this finding, in Project C we then investigated whether compromised grid-cell-like representations might be associated with path integration deficits in old age. Indeed, we found that individual magnitudes of grid-cell-like representations were predictive of age-related deficits in a behavioral path integration task, in which participants had to navigate based on integrating body-based or visual self-motion cues. On the one hand, these findings demonstrate that compromised grid-cell-like representations might be a key mechanism to explain reduced path integration performance in old age. On the other hand, however, it remained to be determined whether and to what extent other sources of error might also contribute to path integration errors in young and older adults. To address this, in Project D we used a computational modeling approach in order to decompose path integration errors into distinct causes that can corrupt path integration computations. We identified internal noise in path integration computations and a biased gain in estimating the speed of self-motion as the main error sources across both young and older adults, with an increase in internal noise accounting for the majority of age-related path integration deficits. Together, the work in this thesis not only advances our understanding of the specific contributors to path integration error, it also helps elucidate the mechanisms that underlie age-related decline in navigational functions.

TABLE OF CONTENTS

1. GENERAL INTRODUCTION 11
   1.1 Population aging 11
   1.2 The aging navigational system 12
      1.2.1 The brain's spatial representation system 16
      1.2.2 Age-related changes in neuronal representations of space 20
   1.3 Investigating grid cell function in humans 23
   1.4 Path integration 26
      1.4.1 Age-related path integration deficits 27
      1.4.2 Computational models of path integration 28
   1.5 Aims of this thesis 30
      1.5.1 Project A 30
      1.5.2 Project B 31
      1.5.3 Project C 31
      1.5.4 Project D 32

2. PROJECT A: The Grid Code Analysis Toolbox (GridCAT) 33
   2.1 Project introduction 33
   2.2 Grid code analysis 37
      2.2.1 Functional image preprocessing for grid code analysis 38
      2.2.2 Specifying grid events 38
      2.2.3 Partitioning the grid code data into estimation and test sets 38
      2.2.4 Estimating grid orientations in the BOLD signal 39
      2.2.5 ROI selection 41
      2.2.6 Quantifying the magnitude of the grid code response 41
      2.2.7 Analysis of grid code stability 43
      2.2.8 Control analyses 44
   2.3 Analysis of example dataset 44
      2.3.1 Methods 45
      2.3.2 Results 48
   2.4 Discussion 54
   2.5 License statement 56
   2.6 Contributions and acknowledgements 57

3. PROJECT B: Grid-cell-like representations in old age 59
   3.1 Project introduction 59
   3.2 Method 61
      3.2.1 Participants 61
      3.2.2 Object-location memory task 61
      3.2.3 MRI scanning parameters 66
      3.2.4 fMRI data preprocessing 67
      3.2.5 Correction for head movement during scanning 67
      3.2.6 Entorhinal cortex region of interest masks 67
      3.2.7 Analysis of grid-cell-like representations 69

3.2.8 Analysis of representational stability 71
3.2.9 Control analyses 72
3.2.10 Quantification and statistical analysis 74
3.3 Results 74
3.3.1 Grid-cell-like representations in young and older adults 74
3.3.2 Control analyses 78
3.4 Discussion 82
3.5 Contributions and acknowledgements 85

4. PROJECT C: Compromised grid-cell-like representations as a mechanistic explanation for age-related path integration deficits 87
4.1 Project introduction 87
4.2 Method 90
4.2.1 Participants 90
4.2.2 Path integration task 91
4.2.3 Path integration data analysis 97
4.2.4 Neuropsychological tests 99
4.2.5 Quantification and statistical analysis 101
4.3 Results 101
4.4 Discussion 106
4.5 Contributions and acknowledgements 109

5. PROJECT D: Sources of path integration error in young and older adults 111
5.1 Project introduction 111
5.2 Method 113
5.2.1 Participants 113
5.2.2 Path integration task 114
5.2.3 Path integration data analysis 119
5.2.4 Computational modeling 121
5.2.5 Quantification and statistical analysis 123
5.3 Results 124
5.4 Discussion 132
5.5 Contributions and acknowledgements 135

6. GENERAL DISCUSSION 137
6.1 Summary 137
6.2 Limitations 141
6.2.1 Limitations related to the Grid Code Analysis Toolbox 141
6.2.2 Limitations related to our scientific findings 142
6.3 Implications and future perspectives 145

REFERENCES 151

APPENDIX 1: The GridCAT Manual 159

APPENDIX 2: Computational modeling details 181

LIST OF ABBREVIATIONS 189

DECLARATION / ERKLÄRUNG 191

1. GENERAL INTRODUCTION

1.1 Population aging

According to the *World Population Ageing Report* (2015) of the United Nations, the number of people in the world older than 60 years is predicted to more than double its size between 2015 and 2050, and the number of people aged 80 or older is predicted to grow even faster and more than triple within that timeframe. Moreover, the number of older adults is growing faster than the number of people in all other age groups, leading to a progressively increasing proportion of older adults relative to the rest of the society (**Figure 1**). For example, both in Europe and Northern America, predictions indicate that older adults (those aged 60 years or over) will account for more than 25% of the population by 2030.

This development can be expected to have far reaching economic, social and political implications. One of the major challenges in this context will be that a significant proportion of older adults will have to cope with health issues, including normative or pathological cognitive decline. This does not only have consequences for the affected individuals, but might also lead to increasing costs for health systems, as a growing number of people with cognitive decline also implies an increasing demand for care as well as for services and technologies that help to treat age-related diseases and chronic conditions. It is therefore imperative for researchers to elucidate the mechanisms underlying age-related loss of cognitive abilities, as providing such insights is a necessary precondition for designing efficient interventions and therapeutic approaches to counteract cognitive decline in old age.

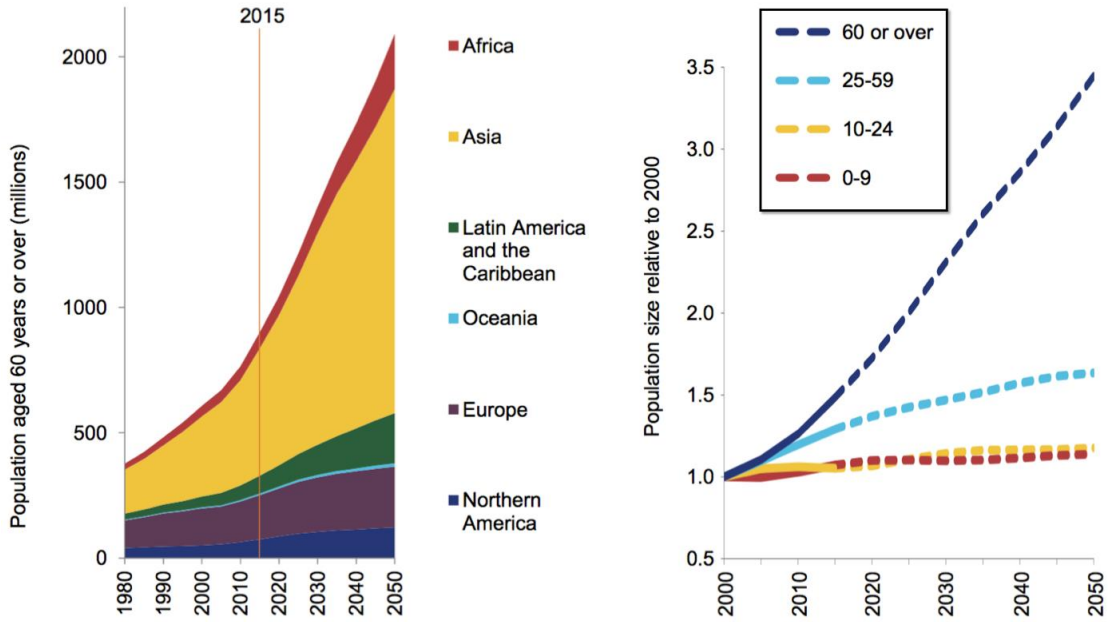

Figure 1: Population aging in recent years and projections for the coming decades

Left: *Worldwide, the number of older adults (aged 60 years or over) has increased substantially in recent years and this growth is expected to continue and even accelerate in the near future.* ***Right:*** *Population size relative to the year 2000, separately for different age groups. It is evident that the number of older adults is growing faster than the numbers of people in any other age group.*

Figure adapted from the United Nations' World Population Ageing Report (2015).

1.2 The aging navigational system

Some cognitive processes that are known to decline with age, such as memory and executive functions, attention, or working memory, have been studied extensively in the past. Surprisingly, however, spatial navigation abilities received relatively little attention in cognitive aging research, even though the ability to navigate within an environment is one of the most fundamental behaviors in both humans and animals. In fact, spatial navigation abilities are necessary for successful functioning in everyday life and impairments in navigational functions can have severe consequences for individuals, such as impaired mobility, reduced social participation, and isolation.

Spatial navigation is a particularly complex behavior that involves a multitude of cognitive functions and computations, such as storage and recall of information and integration of a variety of sensory and proprioceptive stimuli. In general, spatial navigation can be based on processing environmental cues or self-motion cues (Gallistel, 1990). Environmental cues are usually static and comprise stable objects in the environment, such as landmarks (i.e., salient features of the environment) or boundaries. Such environmental cues can be used to determine one's position and orientation within an environment. By contrast, self-motion cues are usually dynamic and comprise optic flow (i.e., the pattern of apparent motion of objects, surfaces and edges) arising from visual perception, as well as body-based cues derived from proprioceptive and vestibular information, and motor efference copies that are produced during movement (Etienne & Jeffery, 2004). After being processed in the sensory systems, these cues are integrated in brainstem nuclei and cortical structures (i.e., the medial superior temporal area "MST") to allow an estimation of angular and linear movement velocity (Bassett & Taube, 2001; Biazoli et al., 2006; Britten, 2008; Clark et al., 2012; Cullen, 2012; Butler & Taube, 2015). Consequently, self-motion information from body-based cues and optic flow enables the continuous tracking of one's position and orientation during movement, a function called path integration (Mittelstaedt & Mittelstaedt, 1980).

Together, environmental cues and self-motion cues can inform both allocentric and egocentric reference frames (for a review, see Colombo et al., 2017). An allocentric reference frame involves spatial information about the position of objects within the environment relative to each other. Locations are described in object-to-object relationships independently of the navigator's point of view. An egocentric reference frame, on the other hand, involves spatial information about the navigator's position within the environment, and locations are described in self-to-object relationships that are encoded relative to the navigator.

It is widely known that aging has deleterious consequences on spatial navigation abilities, as some of the key regions within the brain's spatial navigation circuit are particularly vulnerable to neurodegenerative processes, both in normal and

pathological aging (Lester et al., 2017). As illustrated in **Figure 2**, these key regions include for example the entorhinal cortex and the hippocampus, which are both known to be amongst the earliest regions in which pathological forms of proteins, such as amyloid-β plaques and tau in neurofibrillary tangles, accumulate during normal aging as well as during the development of Alzheimer's disease (Braak & Del Tredici, 2015; Mufson et al., 2016; Jagust, 2018).

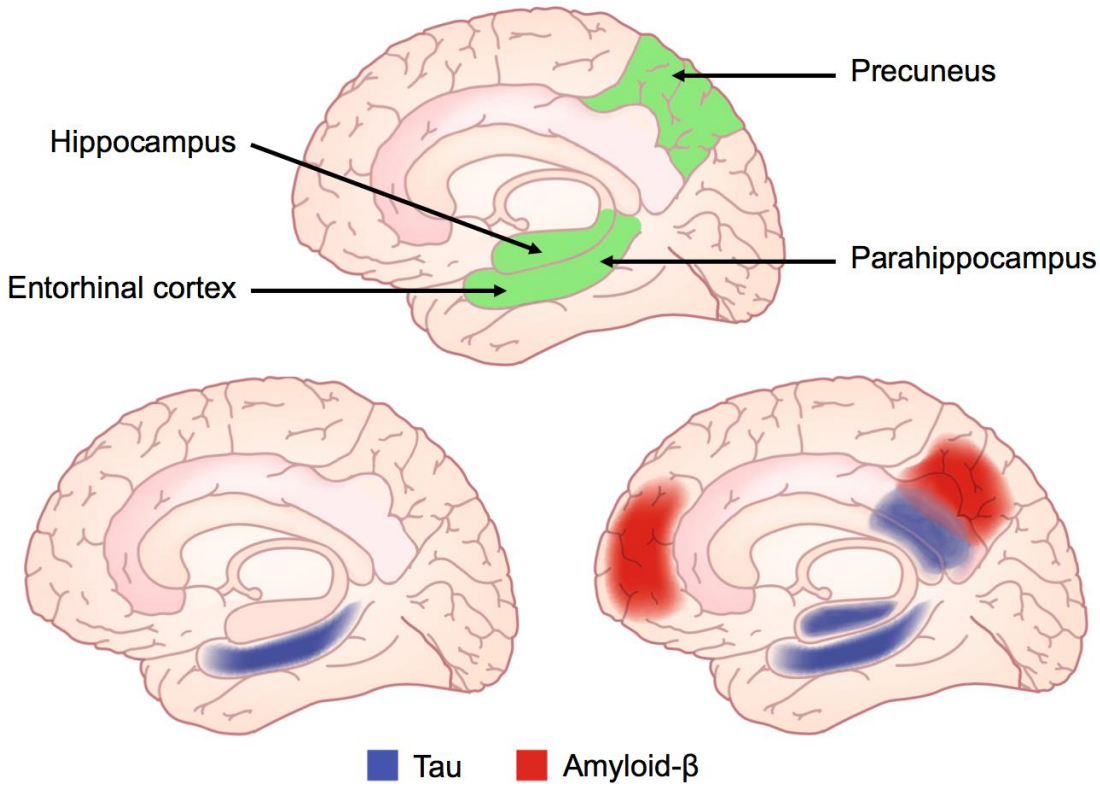

Figure 2: Key regions of the brain's navigation circuit are particularly vulnerable to age-related neurodegeneration

Some of the brain's key regions for navigation (green) are particularly vulnerable to neurodegenerative processes during aging, such as an increased accumulation of harmful amyloid-β and tau proteins. For example, increased tau deposition is already seen in the entorhinal cortex of cognitively normal older adults (bottom left), and pathological tau and amyloid-β deposition in several brain regions, including those of the brain's navigation circuit, are known as hallmark lesions of Alzheimer's disease (bottom right).

Figure (top panel) adapted from Vann et al. (2009). Figure (bottom panel) adapted from Jagust (2018).

Consequently, numerous studies demonstrated deficits of older adults in a variety of spatial navigation tasks and with respect to a broad range of specific navigational functions. For example, in route navigation tasks, which are widely used to test spatial navigation abilities in humans, studies have demonstrated age-related deficits in route learning and wayfinding (Wilkniss et al., 1997; Moffat et al., 2001; Head & Isom, 2010; Wiener et al., 2012).

Another task that revealed spatial navigation deficits in older adults is the Morris Water Maze task. In its original form, this task is used extensively in rodents, to test their ability to locate a hidden platform in a sparse environment that is visible in its entirety with little or no movement (Morris, 1984). In a virtual analogue of the task that was designed to test humans, older adults showed navigational deficits in the form of reduced accuracy, slower learning rates, and a less accurate representation of the environment when asked to reproduce a map after testing (Moffat & Resnick, 2002; Daugherty et al., 2015), indicating that older adults have difficulties with formation and retrieval of long-term memory traces about an environment's spatial layout.

Several studies also revealed age-related difficulties related to the use of landmarks. Specifically, older adults showed difficulties in memorizing correct sequences of encountered landmarks during navigation (Wilkniss et al., 1997; Head & Isom, 2010; Wiener et al., 2012), reduced ability to retrace a recently traveled route based on encountered landmarks (Liu et al., 2011; Wiener et al., 2012), and less accurate binding of directional knowledge to landmarks (Head & Isom, 2010; Liu et al., 2011; Wiener et al., 2012; Zhong & Moffat, 2016).

Moreover, a number of studies demonstrated that intrinsic self-motion-related computations such as path integration are impaired in old age (Mahmood et al., 2009; Adamo et al., 2012; Harris & Wolbers, 2012; Bates & Wolbers, 2014). As path integration abilities are a main focus of this thesis, a more detailed discussion of research on path integration including findings regarding age-related path integration deficits will be provided in subsequent sections (see Section 1.4).

In sum, these results give an exemplary overview over age-related navigational deficits in humans. Together with numerous further studies that are not discussed here in more detail, they provide abundant evidence for a progressive age-related loss of a wide range of spatial navigation abilities both in humans and animals (for a review, see Lester et al., 2017). But despite all of these findings, little is known about the neuronal mechanisms underlying this decline.

1.2.1 The brain's spatial representation system

Recent breakthroughs in understanding how the mammalian brain forms spatial representations of the environment on a neuronal level, led to a deeper understanding of navigational mechanisms and therefore provide an opportunity to investigate specific age-related neuronal changes in the navigation network. Prominent candidates that could mechanistically contribute to age-related navigational deficits are functionally classified neurons that show spatially modulated firing properties, and are therefore thought to form the brain's spatial representation system (Moser et al., 2008).

First evidence for the existence of such neurons was the discovery of so-called place cells in the rat hippocampus (O'Keefe & Dostrovsky, 1971). The firing of these place cells is tuned to the animal's location within an environment (**Figure 3**). While the firing of a single place cell is increased at a specific environmental location, different place cells are tuned to different locations covering the whole environment. Following this discovery, neurons with similar firing properties have also been found in other mammalian species, including mice (McHugh et al., 1996), bats (Ulanovsky & Moss, 2007), nonhuman primates (Feigenbaum & Rolls, 1991), and humans (Ekstrom et al., 2003).

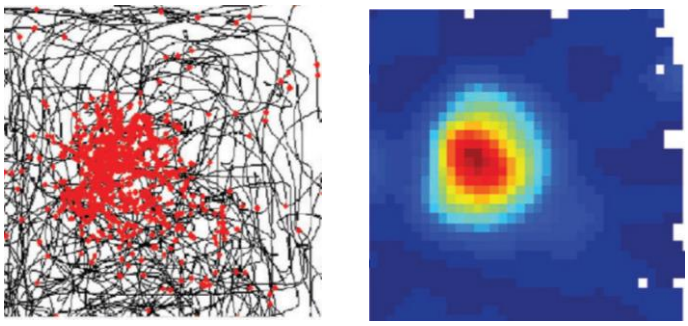

Figure 3: Place cell firing pattern

When an animal is navigating within an environment, a place cell fires whenever the animal enters a particular place in its environment; this place is known as the place field. ***Left:*** *A square environment shown from top-down perspective. Firing locations (red dots) of a typical place cell are superimposed on the animal's trajectory (black lines) in the environment.* ***Right:*** *A different way to illustrate the firing pattern of a place cell is the so-called "rate map". In such a rate map, warmer colors indicate increased cell firing at a particular location of the environment (red indicates maximum firing, dark blue indicates zero).*

Figure adapted from Moser et al. (2015).

Similar to place cells, the firing of so-called grid cells is also modulated by an animal's location within the environment. A grid cell, however, does not only show increased firing in one but multiple locations across the environment. These multiple firing fields show a remarkably regular organization, forming tessellating equilateral triangles that effectively "tile" the world's navigable surface in a hexagonal lattice (**Figure 4**). The equally spaced and repetitive firing means that, for each firing field of a grid cell, the six adjacent fields are arranged in 60° intervals, creating a six-fold symmetry. Originally, grid cells have been discovered in the medial entorhinal cortex of rats (Hafting et al., 2005). Later studies have also provided evidence for grid cells in other brain regions (i.e., subiculum, pre- and parasubiculum), and in different mammalian species, including bats (Yartsev et al., 2011), non-human primates (Killian et al., 2012) and humans (Jacobs et al., 2013). The firing patterns of different grid cells can differ in several ways (**Figure 5**), such as their spatial scale (distance between two neighboring firing fields), orientation (angular tilt relative to an external reference axis in the environment), and phase (displacement in Cartesian coordinates relative to an external reference point in the environment). While the

phase of grid cells appears to randomly vary across different cells, there is evidence that the firing patterns of neighboring grid cells are more similar in terms of their orientation and spatial scale relative to grid cells located further apart (Hafting et al., 2005); distal cells, however, can still show coherence in the orientation of their grids, even though their spatial scales may differ (Barry et al., 2007). The spatial scale has been shown to change depending on the cell's specific anatomical location, with a monotonically increasing scale from dorsomedial to ventrolateral locations of the medial entorhinal cortex in rats (Hafting et al., 2005). In addition, it has been shown that grid cells are often modulated by the animal's heading direction (Sargolini et al., 2006) and velocity (Kropff et al., 2015). Importantly, the work of Doeller et al. (2010) provided first evidence that the putative firing of grid cells (i.e., grid-cell-like representations) can be detected also with a neuroimaging approach in humans using functional magnetic resonance imaging (fMRI). As the method of measuring grid-cell-like representations in humans is a major focus of this thesis, the specifics of this method will be discussed in more detail in subsequent sections (see Section 1.3 and Section 2.2).

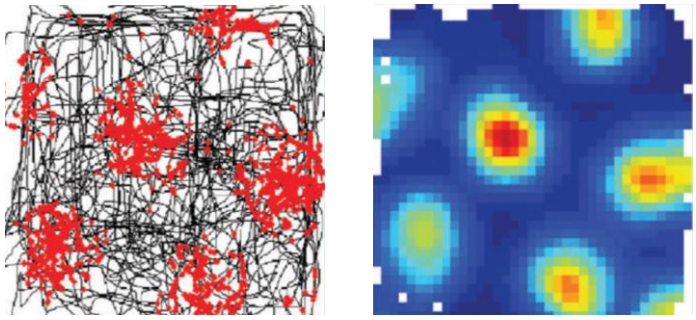

Figure 4: Grid cell firing pattern

When an animal is navigating within an environment, the firing locations (i.e., firing fields) of a grid cell show a remarkably regular organization, forming tessellating equilateral triangles that effectively "tile" the world's navigable surface in a hexagonal lattice. ***Left:*** *A square environment shown from top-down perspective. Firing locations (red dots) of a typical grid cell are superimposed on the animal's trajectory (black lines) in the environment.* ***Right:*** *Rate map of the same grid cell's firing pattern, illustrating the typical regular organization of the grid cell's firing fields (red indicates maximum firing, dark blue indicates zero).*

Figure adapted from Moser et al. (2015).

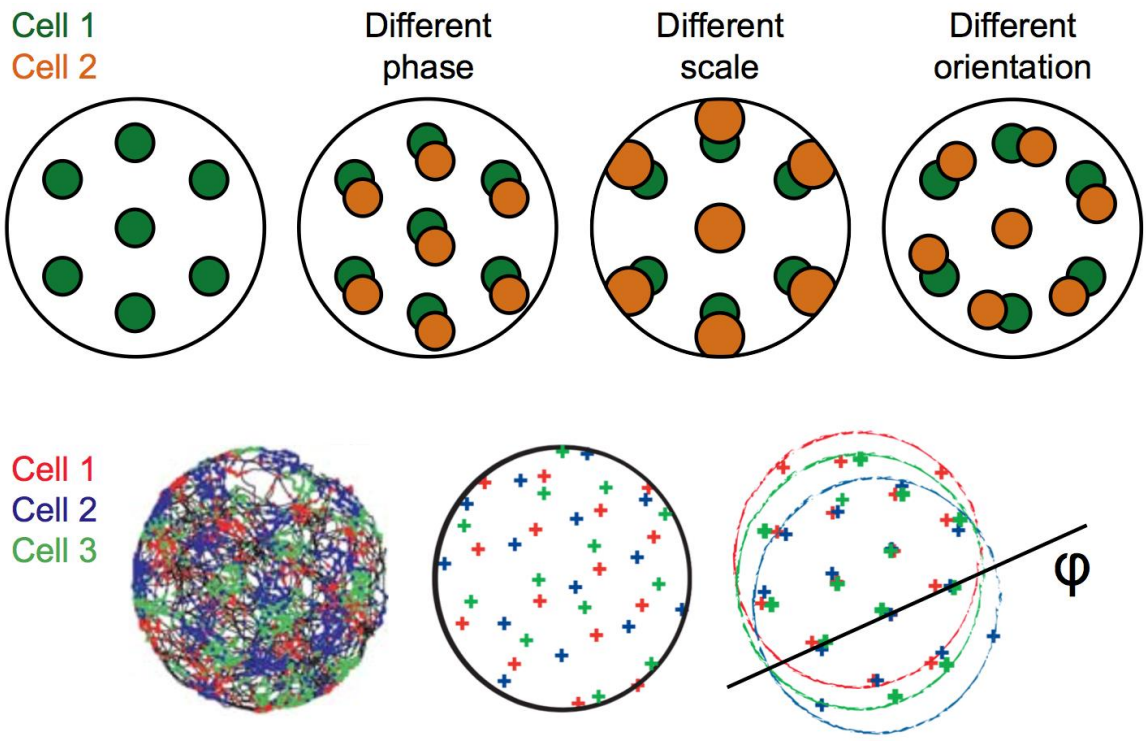

Figure 5: Properties of grid cell firing patterns

Schematic representations of grid cell firing patterns in a circular environment from top-down perspective. ***Top panel:*** *Schematic representation of two grid cell firing patterns (Cell 1 - green vs. Cell 2 - orange). The firing patterns of different grid cells can differ in several ways, such as their phase (displacement in Cartesian coordinates relative to an external reference point in the environment), scale (distance between two neighboring firing fields), and orientation (angular tilt relative to an external reference axis in the environment).* ***Bottom panel:*** *There is evidence that the firing pattern of neighboring grid cells (e.g., Cell 1 - red, Cell 2 - blue, Cell 3 - green) are similar in terms of their orientation (φ), even though their phase and spatial scale may differ (Hafting et al., 2005; Barry et al., 2007). Colored crosses indicate centers of grid cell firing fields.*

Figure (bottom panel) adapted from Hafting et al. (2005).

Another important spatially modulated type of neuron has been found to fire depending on an animal's heading direction (**Figure 6**). Specifically, these so-called head direction cells show increased firing whenever an animal is facing a particular orientation (i.e., the cell's "preferred direction") within the environment. Head direction cells have been found in a network of brain structures, including the pre- and parasubiculum, thalamic nuclei, mammillary bodies, retrosplenial cortex and entorhinal cortex of rodents (Taube, 2007). Moreover, a recent

neuroimaging study also provided evidence for similar head direction coding in humans (Shine et al., 2016).

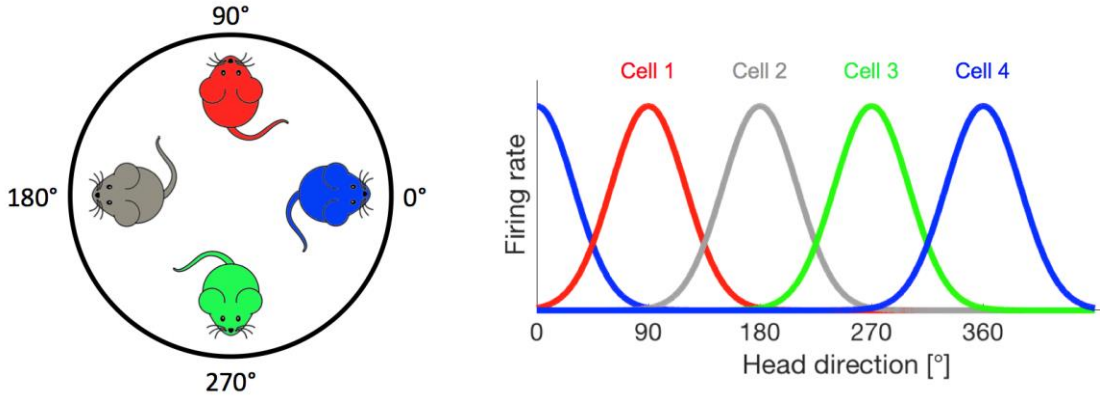

Figure 6: Head direction cell firing

While navigating within an environment, a head direction cell increases its firing rate whenever the animal's head is pointing in the cell's "preferred direction". The schematic example shows the firing rate of four different cells (Cell 1 - 4). For example, Cell 1 (red) fires, whenever the animal faces "North" (90°) in the local environment, while Cell 2 (grey) shows increased firing whenever the animal faces "West" (180°).

Figure adapted from Sharp et al. (2001).

Together with several other functionally classified types of neurons, such as speed cells (which change their firing rate depending on running speed; Kropff et al., 2015) and border cells (which fire in relation to the distance and direction of environmental boundaries; Solstad et al., 2008; Lever et al., 2009) the spatially modulated firing of place-, grid-, and head direction cells is thought to collectively provide the neuronal basis for computations of spatial navigation functions.

1.2.2 Age-related changes in neuronal representations of space

To date, little is known about whether and how firing properties of spatially tuned cells are changing in old age. In the case of head direction cells, no single human or animal study has investigated age-related changes in the head direction cell system so far.

Some evidence was provided for age-related changes in place cell firing: In young rats, place cell firing has been described as consistent across multiple exposures to the same environment, and distinct environments are expected to evoke different place cell firing patterns (O'Keefe & Conway, 1978; Thompson & Best, 1990). Old rats, however, have been reported to occasionally change their place cell firing pattern and generate new and distinct patterns for a familiar environment (Barnes et al., 1997; Schimanski et al., 2013), suggesting an inability to represent an identical environment as one and the same place. On the contrary, when old rats are exposed to different environments, they have been reported to show similar place cell firing patterns across these environments, indicating a deficit in appropriately updating their place cell representation to changes in the environment (Wilson et al., 2006).

Moreover, previous studies reported age-related deficits in so-called experience-dependent place field plasticity, a plasticity mechanism based on which the firing fields of hippocampal place cells increase in size from an initial exposure to repeated traversals of a route (Mehta et al., 1997, 2000; Shen et al., 1997). Due to expanded place fields, this mechanism leads to increased overlap of adjacent firing fields of different place cells along a traveled route, resulting in longer concurrent firing periods of place cells that code for adjacent locations. Consequently, this mechanism is thought to link locations together and to enable a sequential learning of traversed locations along a route. Deficits in place field expansion plasticity, as seen in old animals, could therefore explain age-related deficits in storing spatial sequences.

Direct evidence for age-related changes of grid cell firing characteristics is scarce. Several findings, however, suggest that the grid cell system could be compromised in old age: First, the entorhinal cortex is known to be particularly vulnerable to neurodegenerative processes during both healthy and pathological aging. For example, Gomez-Isla et al. (1996) reported that the number of entorhinal cortex neurons is strongly reduced in Alzheimer's patients, already at very early stages of the disease. Neuroimaging studies using fMRI also showed profound entorhinal cortex volume decrease in patients with Alzheimer's disease

or Mild Cognitive Impairment (MCI; a condition hypothesized to be prodromal to Alzheimer's disease; Du et al., 2001; Pennanen et al., 2004). Moreover, Fjell et al. (2014) investigated cortical thickness of healthy older adults and Alzheimer's patients both cross-sectionally and longitudinally, and demonstrated that accelerated cortical thinning in the entorhinal cortex does not uniquely signify pathological neurodegenerative processes but can be part of healthy aging. Together, these studies highlight the vulnerability of the entorhinal cortex to age-related neurodegeneration. As grid cells have been shown to be primarily located in the entorhinal cortex, it is likely that these neurodegenerative processes also affect the functioning of the grid cell system.

Second, it is known that the entorhinal cortex is one of the major sources of excitatory input to all hippocampal subfields via the perforant pathway (Witter et al., 2000), and previous work provided evidence for coordinated temporal dynamics of entorhinal grid cells and hippocampal place cells (Fyhn et al., 2007). A series of theoretical studies further suggested that the firing pattern of hippocampal place cells could be generated by combining grid firing patterns with different spatial scales (O'Keefe & Burgess, 2005; Fuhs & Touretzky, 2006; Solstad et al., 2006; Rolls et al., 2006; Hayman & Jeffery, 2008; Molter & Yamaguchi, 2008; de Almeida et al., 2009; Si & Treves, 2009; Hasselmo, 2009; Savelli & Knierim, 2010; Monaco & Abbott, 2011; Lyttle et al., 2013), and the study of Brun et al. (2008) demonstrated impaired place cell firing due to entorhinal cortex lesions. Together, these findings imply that place cell firing might – at least to some extent – be driven by input from the grid cell system. Consequently, the structural and functional interconnections between the hippocampal place cell and the entorhinal grid cell system suggest that alterations seen in the firing of hippocampal place cells of old animals (as discussed above) could also be represented in the grid cell system and that age-related changes in place cell firing may be even driven by compromised input from grid cells.

Third, Fu et al. (2017) investigated entorhinal grid cell function in a transgenic mouse model of Alzheimer's diseases expressing mutant human tau pathology.

They found that tau pathology not only induced spatial memory deficits but was also accompanied by deficits in grid cell function, such as reduced firing rates, reduced periodicity and altered network activity of entorhinal grid cells in old mice.

In sum, while none of these studies directly investigated whether healthy human aging is associated with changes in the firing characteristics of grid cells, they nevertheless give rise to the idea that age-related neurodegenerative processes might also impair the entorhinal cortex and entorhinal grid cell function in healthy older adults, which in turn might be linked to spatial navigation deficits in old age.

1.3 Investigating grid cell function in humans

Investigating grid cells in humans is a non-trivial endeavor. One approach that provides an opportunity to use experimental methods analogous to those routinely used in behavioral neuroscience (i.e., recording directly from neurons) is to use intracranial recordings in humans. Surgically implanting electrodes into the human brain, however, is only done in rare and exceptional cases, such as in patients with drug-resistant epilepsy. Consequently, only a limited number of research institutions worldwide have the opportunity to apply this method in order to directly identify grid cell firing in humans, and therefore such studies are scarce and often comprise only small sample sizes. Jacobs et al. (2013) directly recorded from cells in the entorhinal cortex of patients with intractable epilepsy as they completed an object-place memory task requiring them to navigate a virtual environment. Consistent with the rat electrophysiology, there was evidence of cells with a six-fold symmetry in their firing rate, demonstrating that the grid cell appears to be preserved across different mammalian species, including humans.

fMRI is commonly used to investigate the neural correlates of higher-order cognitive processes in large samples of healthy subjects, and this method has been applied to the study of grid-cell-like representations in healthy human subjects (Doeller et al., 2010). Although fMRI is able only to detect changes in

signal over thousands of neurons, several properties of grid cell firing suggested it would be possible to detect grid-cell-like representations in the blood oxygenation level dependent (BOLD) response at the macroscopic level: First, as described earlier, even though grid cells are arranged topographically, the grid orientation of distal cells may still be coherent (Barry et al., 2007). Second, the firing rate of a subpopulation of grid cells, known as “conjunctive grid cells”, is further modulated by the animal’s movement direction in the environment. Specifically, similar to head direction cells, the firing rate of conjunctive grid cells is increased when the animal travels in the cell’s “preferred” direction relative to other travel directions (Sargolini et al., 2006). Furthermore, the preferred firing direction of conjunctive grid cells is aligned with the main axes of the grid (Doeller et al., 2010). Together, these differences in the dynamics of grid cell firing could be reflected in a six-fold sinusoidal pattern observable in the BOLD response (i.e., grid-cell-like representations) when participants performed translations either aligned or misaligned with the grid’s axes (**Figure 7**). Using an object-place memory task in a virtual environment, Doeller et al. (2010) found exactly this pattern of data in several brain regions, including the entorhinal cortex. Consistent with the results of rodent electrophysiology, the BOLD signal showed a six-fold symmetry, with greater activity associated for translations in which the travel direction was aligned with the mean grid orientation, compared to when the travel path was misaligned with a grid axis (the precise methods for estimating the mean grid orientation, and testing the model, are described in detail in Section 2.2 of this thesis). This study, therefore, was critical in demonstrating that fMRI could be used to study grid-cell-like representations in humans.

Despite increasing interest in the role of grid cells in human cognition, there remain relatively few studies investigating human grid-cell-like representations so far, perhaps due to the complex analysis methods, which are not included in standard fMRI analysis packages and require a range of skills, including advanced computer programming, and knowledge of specific mathematical techniques.

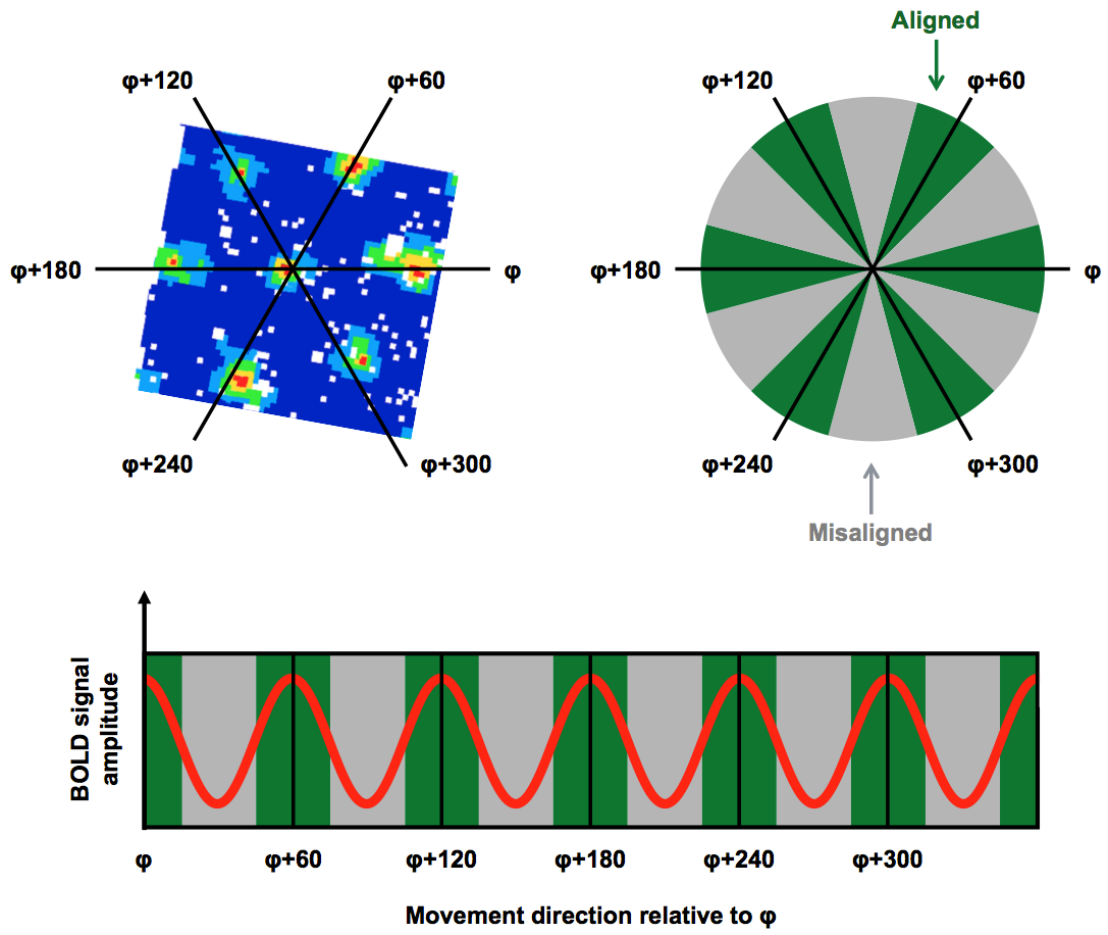

Figure 7: The analysis logic for measuring grid-cell-like representations in human fMRI signals

Top left: *Rate map of a typical grid cell firing pattern in a square environment (shown from top-down perspective). The firing pattern shows a specific orientation (φ) relative to an external reference axis in the environment.* ***Top right:*** *Movement directions within the environment can be categorized either as aligned (green) or misaligned (grey) with the grid cell's firing orientation φ.* ***Bottom:*** *The red curve shows the expected pattern of the BOLD signal amplitude modulated by movement direction relative to φ. High signal peaks are expected for movements aligned with φ or a 60° multiple of φ (green sectors). Figure adapted from Doeller et al.* (2010).

Nevertheless, the identification of human grid-cell-like representations using fMRI has already generated a number of promising new research questions. For example, the measurement of grid-cell-like representations has been shown to have potential clinical applications with reduced grid-cell-like representation magnitudes evident in those at increased genetic risk of Alzheimer's disease (Kunz et al., 2015). Furthermore, although there appear to be commonalities in

the neural mechanisms supporting navigation across diverse species, the study of grid-cell-like representations in fMRI has demonstrated that these spatial codes may be used more flexibly in humans (Horner et al., 2016). Specifically, Horner et al. found evidence of the sinusoidal pattern in the BOLD response when participants imagined navigation in a virtual environment, despite the absence of visual input. Constantinescu et al. (2016) demonstrated that recently acquired conceptual knowledge is organized using the same six-fold spatial symmetry. Most recently, two studies demonstrated that grid-cell-like representations are involved also in the encoding of visual space and potentially contribute to memory-guided viewing behavior (Julian et al., 2018; Nau et al., 2018). In humans, therefore, grid-cell-like representations may be used more abstractly in service of higher-order cognitive processes beyond pure spatial navigation.

1.4 Path integration

Ever since their discovery, grid cells were thought to provide a metric for space and therefore play a key role in navigational computations. Specifically, given their periodic hexagonal firing pattern together with observations that their firing is modulated by both heading direction and running speed (Fyhn et al., 2004; Hafting et al., 2005; Sargolini et al., 2006), grid cells could, theoretically, enable the integration of self-motion information about distance, orientation, and speed during movement. An extensive body of both theoretical and mathematical models therefore postulated that grid cells would provide the neuronal basis for path integration computations, i.e., allow for keeping track of one's position in the environment based on the continuous integration of self-motion information, such as body-based cues and optic flow (Fuhs & Touretzky, 2006; McNaughton et al., 2006; Burgess et al., 2007; Guanella et al., 2007; Hasselmo, 2008; Burak & Fiete, 2009; Giocomo et al., 2011; Zilli, 2012; Widloski & Fiete, 2014).

This hypothesis received indirect support from studies in rodents with brain lesions identifying the entorhinal cortex as a key region for path integration

(Parron & Save, 2004; Van Cauter et al., 2013; Jacob et al., 2017). In addition, self-motion information was shown to be conveyed to the rodent's medial entorhinal cortex (i.e., the grid cell's predominant location) via multiple pathways involving cortical areas and subcortical structures (Rochefort et al., 2013; Hitier et al., 2014; Jacob et al., 2014). Direct empirical evidence for the involvement of grid cells in path integration computations, however, is scarce. Most recently, Gil et al. (2018) showed that the disruption of grid cell firing by removing NMDA glutamate receptors from the retro-hippocampal region leads to impaired path integration performance in mice, and therefore provided first experimental evidence supporting the hypothesis that grid cell function is linked to path integration abilities.

In humans, a specific task that is commonly used to study path integration abilities is the so-called triangle completion task (Loomis et al., 1993). In this task, participants are led along two segments of an imaginary triangular path, before they are asked to "complete the triangle" by returning to the origin of the path. Path integration performance can then be quantified by measuring how accurately they could re-locate the path's origin. Previous studies applied this task in various versions, such as blindfolding participants and restricting them to body-based cues only (e.g., Allen et al., 2004; Adamo et al., 2012), moving them in a wheelchair so that only vestibular cues could be used (e.g., Allen et al., 2004), or using navigation in virtual environments that allows for visual but not body-based cues to be integrated (e.g., Mahmood et al., 2009; Adamo et al., 2012; Harris & Wolbers, 2012).

1.4.1 Age-related path integration deficits

As described before, it is known that aging has deleterious consequences on path integration abilities and that older adults often show relatively strong difficulties in path integration tasks. For example, studies have demonstrated age-related path integration deficits in the triangle completion task when only body-based, vestibular, or visual information could be used (Allen et al., 2004; Mahmood et al., 2009; Adamo et al., 2012; Harris & Wolbers, 2012). Moreover,

older adults showed lower path integration performance even when additional landmark information was available (Harris & Wolbers, 2012; Bates & Wolbers, 2014). Similarly, older adults have been reported to be less accurate in reproducing traveled distances and rotations, respectively (Mahmood et al., 2009; Adamo et al., 2012; Harris & Wolbers, 2012).

Despite this clear evidence for path integration deficits in old age, little is known about the underlying sources and neuronal mechanisms of this decline. Given the particular vulnerability of the entorhinal cortex to neurodegenerative processes during aging, and the presumed importance of entorhinal grid cells for path integration and navigational computations, one could hypothesize that compromised grid cell function underlies impaired path integration performance in old age. Therefore, investigating the association between path integration abilities and grid cell function, or human grid-cell-like representations, may reveal whether changes in the aging grid cell system can provide a mechanistic explanation for age-related path integration deficits.

1.4.2 Computational models of path integration

Computational modeling provides another approach to study the specific contributors to path integration error, in order to understand the causes of inter-individual variability in path integration performance as well as age-related path integration deficits. A computational model describes path integration computations in mathematical terms, including the effects of different sources of error that may theoretically impact on path integration performance.

Previous work characterized human path integration behavior often by response compression or regression to the mean, for example an overshooting for small and an undershooting for larger distances. To explain this behavior, the encoding error model (Fujita et al., 1993) incorporated systematic errors in encoding distances and turns, in the computation of the homeward trajectory and in the execution of the motor response. Results from triangle completion experiments suggested that performance could be best described by individual encoding functions that assumed a fixed gain and intercept for the processing of self-

motion cues, while response computation and motor execution had little contribution (Fujita et al., 1993). However, the model could not well approximate performance when more complex paths involving several turns or crossing segments were used.

Another class of models has postulated that a “leaky” integrator might be responsible for path integration errors (Lappe et al., 2007, 2011), and identified a greater leak in older adults as a potential source of age-related path integration deficits (Harris & Wolbers, 2012). Leaky path integration proposes that humans continuously track a state variable, such as the current distance from the starting point, and this variable is updated with every step of the movement. However, because the integration is leaky, some small percentage of the state variable’s value is deducted in every step. These models can successfully explain underestimation effects when subjects have to indicate the distance to start following visual movement along straight or curved outbound paths (Lappe et al., 2007, 2011).

While both encoding error and leaky integrator models assume fixed parameters across an experiment, Petzschner and colleagues have suggested that path integration errors could be the result of a system that dynamically incorporates knowledge about prior experience into the current estimate of displacement (Petzschner & Glasauer, 2011; Petzschner et al., 2015). Specifically, the observed behavior could reflect the fusion of a noisy displacement estimate with an experience-dependent prior expectation, which is dynamically updated in the course of an experiment. With this approach, it is possible to not only explain regression to the mean but also range effects, because the behavior for a given trial type can vary depending on the characteristics of the preceding trials.

1.5 Aims of this thesis

First, this thesis focuses on the analysis method for measuring grid-cell-like representations in human fMRI signals, and on the development of an open source software tool for this analysis. Applying this software, we then investigated whether grid-cell-like representations are compromised in old age. Moreover, we tested whether magnitudes of grid-cell-like representations are associated with individual path integration abilities, and whether compromised grid-cell-like representations might serve as a mechanistic explanation for age-related path integration deficits. Finally, we used a computational modeling approach in order to disentangle and characterize the different contributors to path integration errors in young and older adults.

Within this thesis, these topics are addressed in four separate research projects (Projects A-D).

1.5.1 Project A: The Grid Code Analysis Toolbox (GridCAT)

Given the methodological complexity of investigating grid-cell-like representations in humans, Project A aimed to lay the methodological foundation and to implement a software for this analysis that can be used for further research projects within the lab and also shared with other researchers from the field. In this project, we have therefore developed the MATLAB-based open-source Grid Code Analysis Toolbox (GridCAT), which performs an automated analysis of grid-cell-like representations in fMRI data. Moreover, the current literature in the field of fMRI research on grid-cell-like representations is reviewed, with a particular focus on the different analysis options that have been implemented. Key features of the GridCAT are demonstrated via analysis of an example dataset, which is also provided online together with a detailed manual, so that users can replicate the results presented here, and explore the GridCAT's functionality. By making the GridCAT available to the wider neuroscience community, we believe that it will prove invaluable in elucidating the role of grid codes in higher-order cognitive processes.

1.5.2 Project B: Grid-cell-like representations in old age

The development of the GridCAT provided the methodological framework to analyze grid-cell-like representations in human fMRI data. Applying this framework, Project B then aimed to investigate grid-cell-like representations in healthy young and older adults. Specifically, we tested whether the magnitude of grid-cell-like representations was reduced in older as compared to young adults, and whether properties of grid-cell-like representations (such as their spatial or temporal stability) were different between age groups. Moreover, as cognitive aging is known to be accompanied by many behavioral and neurophysiological changes, we tested whether age differences in confounding factors, such as fMRI signal quality, task performance, entorhinal cortex volume, or movement artifacts during fMRI scanning, could serve as alternative explanations for any potential age-related differences in grid-cell-like representations.

1.5.3 Project C: Compromised grid-cell-like representations as a mechanistic explanation for age-related path integration deficits

Both theoretical assumptions and computational models have long suggested a link between grid cells and path integration abilities (Fuhs & Touretzky, 2006; McNaughton et al., 2006; Burgess et al., 2007; Guanella et al., 2007; Hasselmo, 2008; Burak & Fiete, 2009; Giocomo et al., 2011; Zilli, 2012; Widloski & Fiete, 2014). Empirical evidence for this hypothesis, however, is scarce. In Project C, we investigated whether performance in a path integration task was associated with grid-cell-like representations, both in young and older adults. This should, on the one hand, provide further support for the hypothesis that grid cells underlie path integration computations. On the other hand, linking path integration performance with grid-cell-like representations in older adults should reveal whether impairments in grid-cell-like representations might provide a mechanistic explanation for age-related path integration deficits.

1.5.4 Project D: Sources of path integration error in young and older adults

After Project C established the association between grid-cell-like representations and age-related path integration deficits, in Project D we investigated whether and which other sources of error might also contribute to path integration errors in both young and older adults. We combined tests of path integration performance in subjects of different ages with a novel computational model, which allowed us to decompose path integration errors into distinct sources – including leak, noise, biases, and reporting errors – that can corrupt path integration computations. Characterizing the impact of these individual sources of error aimed not only to advance our understanding of the specific contributors to path integration error, but also uncover the mechanisms that could underlie age-related decline in navigational functions.

2. PROJECT A

The Grid Code Analysis Toolbox (GridCAT)

The output of this project has been previously published as an Open Access article in the journal "*Frontiers in Neuroinformatics*" (Stangl et al., 2017). While all results presented here stay unchanged to the original publication, some paragraphs, figures, and corresponding figure captions have been edited, in order to meet the structure, scope, and formatting standards of this thesis.

When publishing this article, we used the term "grid code" to describe the putative signature of grid cell firing in fMRI signals, as the term "grid-cell-like representations" was not established in the literature at this time. Therefore, the term "grid code" can be seen as analogous to the term "grid-cell-like representations" that is used throughout the rest of this thesis.

2.1 Project introduction

Identifying the neural mechanisms supporting spatial navigation remains a key goal for neuroscience. In recent years, significant progress has been made with the discovery of the grid cell in the rat medial entorhinal cortex, a neuron exhibiting firing properties that could provide a spatial metric underlying navigational functions such as path integration (Hafting et al., 2005). Grid cells have been found subsequently in a diverse range of mammalian species (for a review, see Rowland et al., 2016), and, more recently, the putative signature of grid cell firing, which we refer to as the grid code throughout this project, has been identified also in healthy human subjects using fMRI (Doeller et al., 2010; Kunz et al., 2015; Constantinescu et al., 2016; Horner et al., 2016). Given the increasing interest in the role of grid cells in human cognition, and the absence of standard analysis tools to examine grid codes in fMRI, we have developed the Grid Code Analysis Toolbox (GridCAT), which generates grid code metrics from

functional neuroimaging data. The GridCAT is openly available at the Neuroimaging Informatics Tools and Resources Clearinghouse (NITRC) and can be downloaded from: http://www.nitrc.org/projects/gridcat

Grid code analyses are distinctly non-trivial, requiring a range of skills, including advanced computer programming, and knowledge of specific mathematical techniques (e.g., quadrature filter techniques). Not all cognitive neuroscientists who wish to examine cognitive processes related to grid cell firing in humans possess these skills. To cater for these researchers, the GridCAT provides a simple graphical user interface (**Figure 8**), meaning that the user is not required to work directly with the source code. Moreover, given that no standard analysis package offers the necessary algorithms to detect grid codes in fMRI data, even researchers who are capable of reproducing all necessary analysis steps may find it a demanding and time-consuming task to write the source code required for this type of analysis. The GridCAT addresses these issues by performing automatically all steps in the grid code analysis pipeline (as summarized in **Figure 9**). By removing the need to develop source code independently, the toolbox opens up this exciting research area to the wider neuroscience community, and saves researchers time, allowing them to address novel research questions regarding the role of grid cells in human cognition.

A further aim of this project is to provide, for the first time, a comprehensive overview of the different analysis strategies that have been used to date. By synthesizing these different approaches, we hope to inform researchers who are new to the field about the different possible ways in which the fMRI data can be modeled to assess grid code metrics. Finally, by making a number of analysis options available in the toolbox, the GridCAT will also help to standardize analyses across the research community, making data analysis pipelines more comparable across different labs, and stimulating discussion in this exciting and rapidly developing research area.

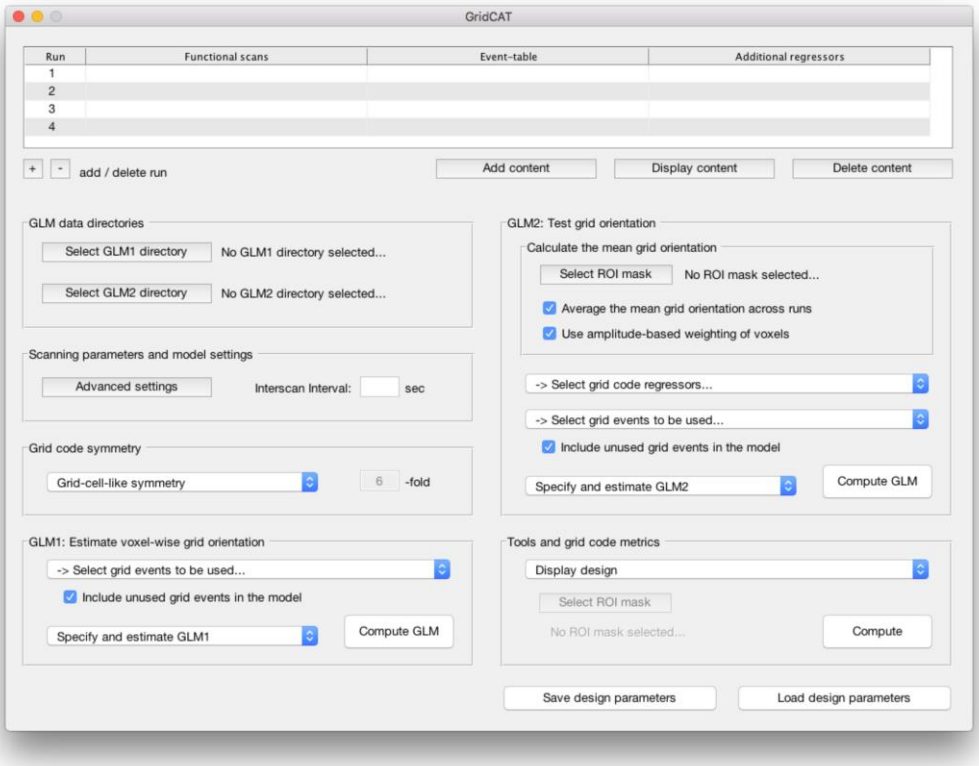

Figure 8: The graphical user interface (GUI) of the GridCAT

A grid code analysis can be carried out via the GUI by specifying data, parameters, and settings, depending on the individual experimental design and research question. The GUI offers all analysis options of the grid code analysis pipeline as well as a set of additional tools to generate grid code metrics, visualize results, and export the resulting data. A detailed explanation of all GUI options and how to use all functions of the GridCAT via the GUI, is provided in the GridCAT user manual that is distributed along with the open-source code. Please note that the visual appearance of the GUI might differ between operating systems and versions of MATLAB.

The GridCAT allows users to input easily their study design and performs all analyses to estimate the grid code in functional images and generates automatically grid code metrics. Results can be visualized using built-in plotting functions, and the data can be exported for further analyses depending on the user's needs. It requires only a basic MATLAB installation (i.e., no additional Mathworks toolboxes are required), SPM12 (http://www.fil.ion.ucl.ac.uk/spm/), and it is compatible with Windows, Linux, and Mac OS. A detailed manual (see

Appendix 1) guides users through all steps of a grid code analysis and an example dataset is provided with the GridCAT to explore its functionality.

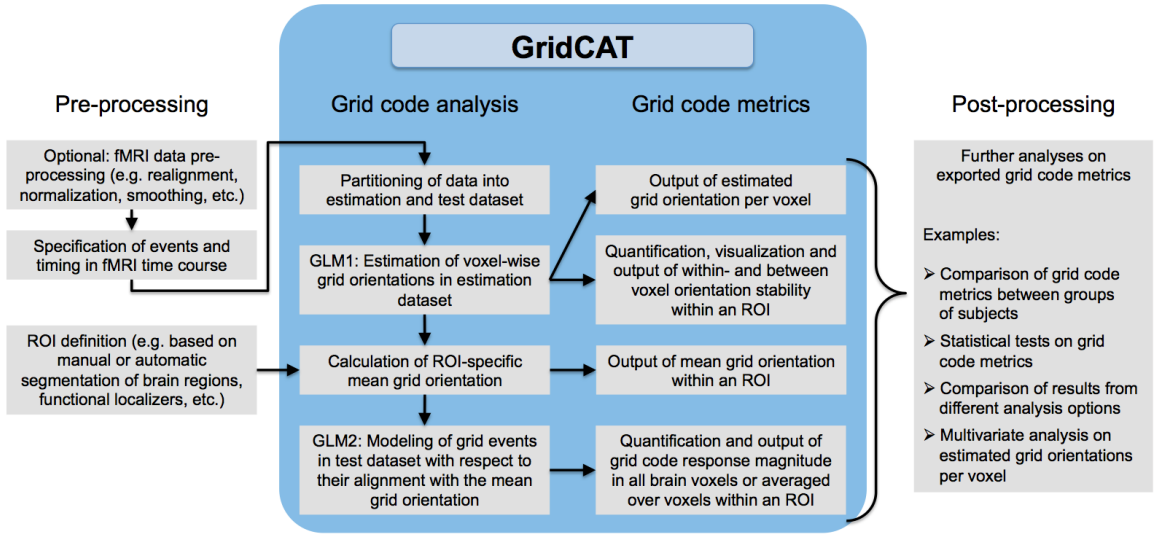

Figure 9: Grid code analysis pipeline

All that is required to perform a grid code analysis are functional brain images (which, depending on the user's wishes, may have undergone standard fMRI data preprocessing such as smoothing etc.) together with a file detailing events of interest during the fMRI time course and their corresponding timing information. The GridCAT partitions these data into an estimation dataset and a test dataset, offering multiple options as to how to split the data depending on the experimental design and the user's needs. Using the estimation dataset, the GridCAT then estimates voxel-wise grid orientations of the grid code in a first general linear model (GLM1). As a result, voxel-wise grid orientations are stored and can be plotted using the GridCAT's specific plotting options to visualize grid code stability both within and between voxels, or can be exported in several formats for further analysis such as group level analyses, statistical testing, or voxel-wise multivariate analysis methods. Moreover, within any region of interest (ROI), the GridCAT can calculate an ROI-specific mean grid orientation, providing that the mask image (e.g., anatomically or functionally defined) and functional data are registered to one another. Finally, in a second general linear model (GLM2) the GridCAT allows events in the test dataset to be modeled with respect to their alignment with the ROI-specific mean grid orientation, in order to quantify the grid code response magnitude individually for all brain voxels or averaged over voxels within an ROI. All results and grid code metrics can be exported for further use with statistical and neuroimaging analysis tools of the researcher's choice.

Although there are similarities across fMRI studies in the methods used to estimate grid code metrics, there is as yet no standard analysis pipeline. Because of this, the GridCAT has been designed to be flexible in accommodating a number of different analysis options; decisions regarding a

researcher's own pipeline will depend upon paradigm-specifics and the research question of interest. We note that a recent grid code study examined the neural signal associated with imagined trajectories in the environment (Bellmund et al., 2016). We do not discuss this experiment here, however, because, rather than the mass univariate method commonly used in the study of grid codes, they used multivariate representational similarity analysis, for which there are already several toolboxes available (Nili et al., 2014; Oosterhof et al., 2016). In the following section, we review extant methods for deriving grid codes in fMRI, and highlight differences in analysis approaches. The aim of this review is to inform the GridCAT user of the different analysis options that have been used previously, and that are available in the toolbox, rather than to provide a critique as to best practice for deriving grid code metrics.

2.2 Grid code analysis

Although analysis pipelines for the examination of grid codes using fMRI differ in several aspects (see Sections 2.2.1 - 2.2.8), the overall procedure is relatively similar. First, events of interest for the grid code analysis (i.e., so-called "grid events") are specified in the time course of the imaging data. Second, the imaging data are then partitioned into estimation and test datasets. Third, a general linear model (GLM) is fit to the estimation dataset to estimate voxel-wise orientations of the grid code (i.e., GLM1 – see Section 2.2.4). Fourth, these voxel-wise orientation values are then averaged over voxels in a region of interest (ROI) to generate a mean grid orientation used for a second GLM in which grid events of the test dataset are modeled with respect to their alignment with the mean grid orientation (i.e., GLM2 – see Section 2.2.6). Finally, grid code metrics are computed, such as the magnitude of grid code response as well as measures of between- or within-voxel orientation coherence of the grid code (see Section 2.2.7). In the following sections, we provide more information regarding these individual steps of the grid code analysis pipeline (see also **Figure 9** for a comprehensive overview).

2.2.1 Functional image preprocessing for grid code analysis

The GridCAT is agnostic with regards to the nature of the preprocessing carried out on functional images prior to the grid code analysis. For example, the analysis can be conducted using a participant's normalized, and smoothed, functional images (Doeller et al., 2010; Constantinescu et al., 2016; Horner et al., 2016). Alternatively, one could work in the individual subject's native functional space (Kunz et al., 2015). Motivations for normalizing to standard space prior to analysis include the desire to examine group-level, cluster-statistics (e.g., Constantinescu et al., 2016), whereas researchers concerned about spatial distortions or interpolation errors in their data resulting from normalization to a standard template might choose to perform the grid code analysis in the participant's native space. fMRI preprocessing can be carried out in the researcher's neuroimaging analysis package of choice.

2.2.2 Specifying grid events

Before the grid code can be estimated, it is necessary to specify grid events within the fMRI time course. For example, grid events could comprise periods of translational movement (e.g., Doeller et al., 2010; Kunz et al., 2015; Horner et al., 2016) within a virtual environment. For each grid event, an angle relative to a nominal 0° reference point (e.g., a fixed landmark in the virtual environment) is then defined, resulting in the "grid event angle". More details as to how grid events are defined for use in the GridCAT analysis pipeline are provided in the GridCAT manual (see Appendix 1).

2.2.3 Partitioning the grid code data into estimation and test sets

Given that the functional data are labeled either as estimation or test data, researchers must decide how to perform this partition. One method is to split the data run-wise into odd and even runs (Doeller et al., 2010; Kunz et al., 2015), performing the estimation in the odd runs and testing in the even ones (or vice-

versa). Alternatively, one could split the data into a number of temporal bins, and perform the same analysis on these odd/even bins (Horner et al., 2016). As well as offering these data partitioning methods, the GridCAT also provides options to separate grid events within each scanning run into odd and even events, or to split each scanning run into two halves so that estimation and test are calculated on the first and second halves of runs, respectively. Furthermore, if these default partitioning options are not suitable for a particular experiment, bespoke partitioning schemes can be specified in the GridCAT event-table (which is described in detail in the GridCAT manual), allowing the user to specify whether a particular grid event should be assigned either to the estimation or test dataset.

2.2.4 Estimating grid orientations in the BOLD signal

For the estimation data (GLM1), the grid event angle is used to create two parametric regressors for the grid events, using $\sin(\alpha_t*6)$ and $\cos(\alpha_t*6)$, respectively, where α_t represents the grid event angle. The multiplication term (*6) used in the calculation of these two regressors transforms the grid event angle into 60° space, mirroring the hexagonal symmetry observed in grid cell firing. By including these parametric regressors in the general linear model, voxels with time courses showing modulation of their signal according to six evenly spaced 60° intervals would have parameter estimates (i.e., beta weights that have been estimated for a regressor in the GLM, with higher parameter estimates indicating a better model fit) with high absolute amplitudes. When calculating GLM1, the GridCAT allows users to include additional regressors (e.g., nuisance regressors, such as movement parameters), add time and dispersion derivatives of the hemodynamic response function (HRF), and change modeling parameters (e.g., high-pass filtering, microtime onset and resolution, masking threshold), depending on the individual experimental design (**Figure 10**). More details about these options can be found in the GridCAT manual (see Appendix 1).

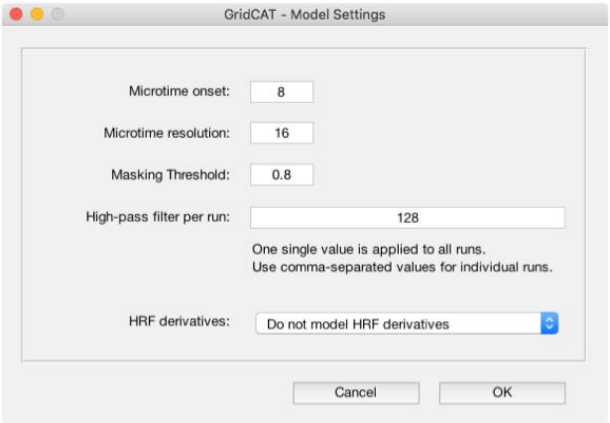

Figure 10: GridCAT dialog window to adapt GLM settings

Before calculating a GLM with the GridCAT, users can and add time and dispersion derivatives of the hemodynamic response function (HRF), and adapt model settings (microtime onset, microtime resolution, masking threshold, high-pass filters) via a dialog window.

Voxel-wise grid orientations resulting from GLM1 can be visualized using the GridCAT's specific plotting options, and different grid code metrics such as grid code stability both within voxels (e.g., over time) and between voxels (e.g., coherence of grid orientations within an ROI) can be calculated (see Section 2.2.7). Plots can be saved in different file-formats, so that users can subsequently load them into any image processing software and adapt their visual appearance, depending on individual needs. For further analysis such as group level analyses, statistical testing, or multivariate analysis methods on voxel-wise grid orientations, these data can be exported in several formats (e.g., as a data vector, or as a 3D NIfTI image).

Following GLM1, the GridCAT can then calculate the mean grid orientation across all voxels in an ROI. To compute the mean grid orientation, the beta estimates (β_1 and β_2) associated with the two parametric regressors are each averaged over all voxels in the ROI, and the resulting two values submitted to: $\arctan[\text{mean}(\beta_1)/\text{mean}(\beta_2)]/6$. Once the mean grid orientation has been calculated, this value can be used to categorize individual grid event angles in

the test data (GLM2) to determine the magnitude of the grid code response. For example, grid event angles could be classified either as aligned or misaligned with the mean grid orientation (see Section 2.2.6).

2.2.5 ROI selection

As described above, the mean grid orientation can be calculated in any chosen ROI, providing that the mask and functional data are registered to one another. Popular choices of ROI include anatomical masks, such as the entorhinal cortex (Doeller et al., 2010; Kunz et al., 2015; Horner et al., 2016), however it is possible also to input to the GridCAT a functionally-defined mask from an orthogonal contrast (e.g., Constantinescu et al., 2016), or localizer dataset.

2.2.6 Quantifying the magnitude of the grid code response

The greatest degree of heterogeneity in analysis pipelines of fMRI grid code studies stems from how the grid code is quantified, or the choice of grid code metric. This relates, in part, to the research question of interest, and we outline here the different methods that have been used thus far in the published literature. It is worth noting that these methods are not mutually exclusive, and a researcher may want to use a combination of different approaches to test a number of different hypotheses.

In the following sections (2.2.6.1 and 2.2.6.2), we describe different methods to set-up GLM2 where grid events are modeled with respect to their alignment with the ROI-specific mean grid orientation. Irrespective of the method used, additional regressors can be added to GLM2, and modeling parameters can be changed depending on the individual experimental design (as described for GLM1).

Following GLM2, estimates of the grid code response magnitude can be exported either as a 3D NIfTI image containing estimates for all individual brain voxels or as an average of the grid code response magnitude within an ROI, so

that researchers can conduct further analyses on these data using statistical or neuroimaging data analysis and visualization tools of their choice.

2.2.6.1 Parametric modulation

In the original study reporting grid codes in the fMRI signal, Doeller et al. (2010) fitted a parametric regressor to the grid events in the test data to examine whether voxels in an entorhinal cortex ROI showed evidence of a six-fold sinusoidal pattern of activity. The parametric regressor was calculated by taking each grid event angle (α_t), and determining its difference from the mean grid orientation (φ) by calculating $\cos[6*(\alpha_t - \varphi)]$, which resulted in values ranging between "1", for grid event angles aligned perfectly with the mean grid orientation (or a 60° multiple of it), and "-1" for values completely misaligned with the grid code phase (i.e., mean grid orientation + 30°, plus any 60° multiple of this value). Using cluster statistics, Doeller et al. reported voxels at the group-level showing modulation of their signal according to this sinusoidal function. A similar analysis was used in Horner et al. (2016), with the exception that they used a contrast to look for brain regions in which the sinusoidal model fits significantly better for one condition versus another (i.e., imagined navigation versus stationary periods).

2.2.6.2 Comparing activity associated with aligned versus misaligned events

It is possible also to compare parameter estimates associated with aligned versus misaligned grid events. For example, in a subsequent analysis, Doeller et al. (2010) separated grid events into two regressors comprising those translations aligned within 15° of a grid axis versus those more than 15° from a grid axis, and again showed that significantly greater activity in the entorhinal cortex was associated with events aligned with grid axes. This analysis strategy was used also by Kunz et al. (2015) who found that participants at increased genetic risk of Alzheimer's disease show reduced BOLD response, relative to control participants, when contrasting trials "aligned > misaligned" with the grid axis (i.e., a reduction in the ability to detect the grid code). Constantinescu et al. (2016) used a variation of the aligned versus misaligned analysis by sorting the grid event angles into 12 different regressors, each representing a 30° bin. Six regressors comprised aligned trials, those events within ±15° of the mean grid

orientation (or a 60° multiple of it). The remaining six regressors comprised misaligned trials, that is events offset from the mean grid orientation by 30° (plus a 60° multiple of this value) ±15°, and parameter estimates were extracted for each regressor.

2.2.7 Analysis of grid code stability

The ability to detect the grid code in fMRI can be affected by the stability of the estimated grid orientation either between voxels within an ROI, or within voxels across different scanning runs and/or conditions (e.g., stability over time or different spatial environments, respectively). In terms of grid orientation stability between voxels within an ROI, if all voxels provide a different orientation value, then the resulting mean grid orientation would be random, and the coding of grid events in the test data depending on their deviation from the mean grid orientation would be arbitrary. To test whether there was evidence of coherence in the orientation of the grid code between different voxels in their entorhinal cortex ROI, Doeller et al. (2010) submitted all voxel orientation values to Rayleigh's test for non-uniformity of circular data. Doeller et al. reported significant clustering of estimated orientations in around three-quarters of their participants.

Alternatively, an inability to detect grid codes in the fMRI signal could result from instability of the estimated grid orientation within a voxel over time. Kunz et al. (2015) tested the stability of the grid orientation over time by extracting the orientation of a voxel in one half of the data and comparing this to the same voxel's orientation in the second half of the data. These data were scored such that if the values were within ±15° of one another, then the grid orientation for the voxel was classified as stable. At the ROI level, the percentage of voxels showing stability in their estimated orientation over time could then be calculated. Even though participants at risk of Alzheimer's disease showed coherence in grid orientation between voxels within a single scanning run, over time the orientation estimates for a given voxel differed. It was concluded, therefore, that

the reduced ability to detect grid codes in the risk group resulted from instability in the orientation within-, but not between-, voxels in the Alzheimer's risk group.

2.2.8 Control analyses

Given that grid cells identified in rodents show a strict six-fold symmetry in their firing, it is necessary to test whether the best fit for the grid code analysis in fMRI is also a six-fold model, or whether other sinusoidal models fit the data equally well. In all studies published to date, the six-fold model has proven a better fit to estimate the orientation of the grid code in comparison to other symmetrical models (three-, four-, five-, seven- and eight-fold models; Doeller et al., 2010; Kunz et al., 2015; Constantinescu et al., 2016; Horner et al., 2016). These different models can be implemented in the GridCAT, allowing the user to examine whether the six-fold model provides a better fit to the data.

An alternative control analysis, which can be carried out using the GridCAT, is to test for the grid code in regions where one would not expect to observe this signal (e.g., the visual cortex). Although this type of control analysis has been used previously (Doeller et al., 2010), it may be difficult to predict exactly where in the brain one would expect to see this pattern of data. For example, using an orthogonal localizer contrast, Constantinescu et al. (2016) found evidence of the sinusoidal response in a number of different regions including the ventromedial prefrontal cortex, and the posterior cingulate cortex.

2.3 Analysis of example dataset

To demonstrate some of the key features of the GridCAT, we detail here the analysis of functional data from an example participant who was scanned whilst completing a spatial navigation task. The dataset of this example participant is available for download, so that the complete analysis pipeline described here can be reproduced using the GridCAT, giving the user the opportunity to explore

its tools and functions. Furthermore, all necessary steps to analyze the example dataset are described in detail in the GridCAT manual (see Appendix 1).

2.3.1 Methods

The example participant was 28 years old, right handed, had normal vision and no history of psychiatric or neurological disorders. Informed consent was obtained in writing before the measurements, and the experiment received approval from the Ethics Committee of the University of Magdeburg.

2.3.1.1 Spatial navigation task

Prior to scanning, the participant was asked to navigate a square virtual space (160 x 160 virtual meters [vm]) using a joystick and learn the location of three target objects. Afterwards, the participant underwent two separate runs of fMRI scanning during which the participant navigated in the same virtual space. Each trial had the following structure: At the start, all target objects disappeared and an image of one of them was shown at the bottom of the screen (**Figure 11**). The participant was asked to navigate to the position of the cued target object and confirm their choice of location with a button-press. After the button-press, feedback was given to the participant via the target object appearing at its correct location and a smiley-face displayed on the screen that was either green (if the error distance between the correct location and the participant's response was below 20 vm), yellow (for error distances between 20 and 30 vm), or red (for error distances larger than 30 vm). After each trial, the participant was automatically transported to a random position within the virtual space. Each scanning run lasted 16 minutes, and the participant was asked to complete as many trials as possible.

Figure 11: Example trial during fMRI scanning

Prior to scanning, the participant learned the locations of three target objects in a virtual environment. ***Left:*** *During scanning, one of the target objects was cued (e.g., a football) and the participant was asked to navigate to its location.* ***Right:*** *After the participant pressed a button to confirm their choice of location, the target object appeared at its correct location and a smiley-face provided feedback as to the accuracy of the response.*

2.3.1.2 Scanning parameters

T2*-weighted functional images were acquired on a 3 Tesla Siemens Magnetom Prisma scanner using a partial-volume echo-planar imaging (EPI) sequence with the following parameters: repetition time (TR) = 1500 ms, echo time (TE) = 30 ms, slice thickness = 2 mm, in-plane-resolution = 2 x 2 mm, number of slices = 24, field of view = 216 mm, flip angle = 80°, slice acquisition order = interleaved.

For manual delineation of the entorhinal cortex, a high-resolution T2-weighted structural image was acquired using a turbo-spin-echo (TSE) sequence with the following parameters: TR = 6000 ms, TE = 71 ms, slice thickness = 2 mm, in-plane-resolution = 0.5 x 0.5 mm, number of slices = 64, field of view = 224 mm, flip angle = 120°, slice acquisition order = interleaved.

2.3.1.3 Analysis pipeline

Prior to analyses using the GridCAT, the functional images for the two runs were realigned and smoothed (5mm FWHM) using SPM12. Anatomical masks of the right and left entorhinal cortices were traced manually (following Ding et al., 2016) on the participant's T2-weighted image using ITK-SNAP (http://www.itksnap.org/), and co-registered to the EPI data. These two anatomical masks were used as separate ROIs for all following analyses.

As detailed in Section 2.2, there are a number of different ways grid codes can be examined in fMRI data, which are available to the GridCAT user. It is beyond the scope of this thesis to demonstrate all possible combinations of modeling options; therefore, we chose a subset of parameters for the grid code analysis detailed here. The first parameter relates to the way in which the mean grid orientation is calculated. In GLM1, the GridCAT generates an image containing voxel-wise grid orientations, which can then be used to determine the mean grid orientation for a given ROI. The mean grid orientation can be calculated by averaging over voxels in the ROI either within individual scanning runs, or across multiple runs. For example, if one predicts that the grid orientation will change over runs, perhaps due to an experimental manipulation that could induce grid cell remapping (Fyhn et al., 2007), it would be sensible to estimate the grid orientation within individual runs, rather than averaging across them. Although we did not predict that there would be any changes in grid orientation over the two runs in our paradigm, we demonstrate the effect of estimating the mean grid orientation within versus across runs.

We examined also two different ways in which the grid events (i.e., translational movements within the virtual environment) can be modeled in GLM2. In one model, grid events were modeled using a single parametric modulator regressor (e.g., Doeller et al., 2010). In an alternate model, replicating the analysis of Kunz et al. (2015), grid events were separated into two regressors – aligned or misaligned with the mean grid orientation – and contrasted with one another ("aligned > misaligned"). The approach used by Constantinescu et al. (2016) in which grid events are separated into 12 different regressors comprising 30° bins was not used here because our paradigm allowed for free exploration of the environment and therefore it is possible that not all directions were sampled equally. In all GLMs, we included as regressors of no interest the feedback phase in the paradigm, head motion parameters (x, y, z, yaw, pitch, and roll) derived from realignment in SPM12, and the unused grid events (i.e., the grid events for GLM2 when fitting GLM1, and vice-versa).

Finally, we show how different symmetrical models (four-, five-, six-, seven-, and eight-fold) affect the model fit, with the prediction that the six-fold symmetrical model should provide the highest parameter estimates, given that this reflects grid cell firing symmetry.

2.3.2 Results

Consistent with the analysis strategy of Doeller et al. (2010), in GLM1 we found that the orientations of grid codes in voxels of both right and left entorhinal cortex showed significant non-uniformity, or clustering (see **Figure 12**). The GridCAT produces polar histogram plots, which indicate the different orientations derived from voxels in a given ROI, and the number of voxels sharing similar orientations. In these interactive plots (**Figure 13**), the mean grid orientation of all voxels within the ROI can also be calculated and plotted by the GridCAT. Moreover, Rayleigh's test for non-uniformity of circular data can be carried out (applying code from the open-source toolbox CircStat2012a; Berens, 2009), in order to test whether the orientations of the grid code in voxels within an ROI show greater clustering than would be expected by chance. The example data suggest, therefore, that there is stability in grid orientation between voxels within the entorhinal cortex. As can be seen in **Figure 12**, the voxel-wise orientations estimated in the two separate runs were similar to one another, suggesting that the mean grid orientation could be calculated across both runs and used to categorize grid events in GLM2. If, however, these plots had indicated that the mean grid orientations changed over runs, the user might consider estimating and testing grid orientations within individual runs so that the categorization of grid events in GLM2, according to their alignment with the mean grid orientation, was more accurate. Furthermore, the GridCAT allows for the export of voxel-wise orientation values within an ROI, in order for additional analyses and/or statistical tests to be conducted on these data, depending on the user's specific research question.

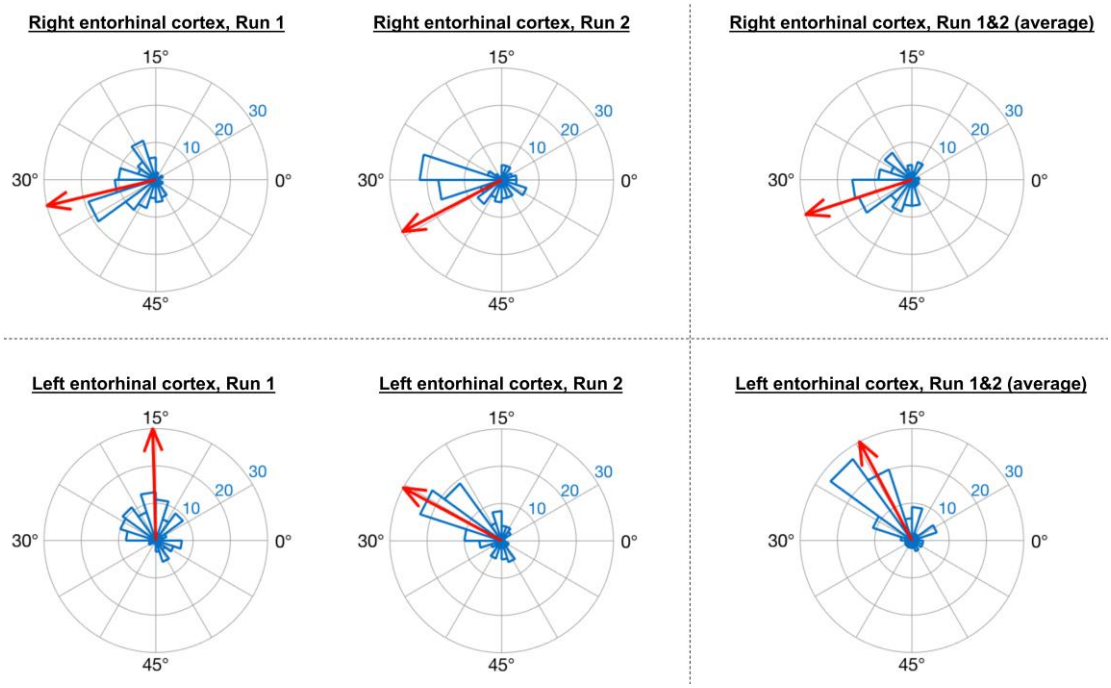

Figure 12: Between-voxel coherence of grid orientations

GridCAT polar histogram plots showing coherence of the grid orientation between voxels in right and left entorhinal cortex ROIs. The length of each bar indicates the number of voxels that share a similar grid orientation, and the blue numbers indicate the number of voxels represented by each ring of the polar plot. The GridCAT also allows the user to calculate and visualize the mean grid orientation (red arrow) for each plot (which is used in GLM2 to model grid events with respect to their deviation from the mean grid orientation). Depending on the user's choice of model, the mean grid orientation can be calculated separately for run 1 (left column) and run 2 (middle column), or alternatively, the mean grid orientation over multiple runs (right column) can be calculated by averaging the parameter estimates. Furthermore, users can choose to carry out Rayleigh's test for non-uniformity of circular data. Rayleigh's test indicated that voxels in both the right (top row) and left (bottom row) entorhinal cortex showed significant clustering (i.e., coherence) in their orientations (all $p < 0.00001$).

The GridCAT can test also the within-voxel stability of the grid orientation across different scanning runs and/or conditions. When the user inputs two different voxel-wise orientation images derived from GLM1, and an ROI, the toolbox generates a plot comprising two polar plot rings (see **Figure 14**). For the analysis presented here, each ring represents a different scanning run, and circle markers denote the grid orientation of individual voxels; straight lines connect grid orientations of the same voxel across different runs.

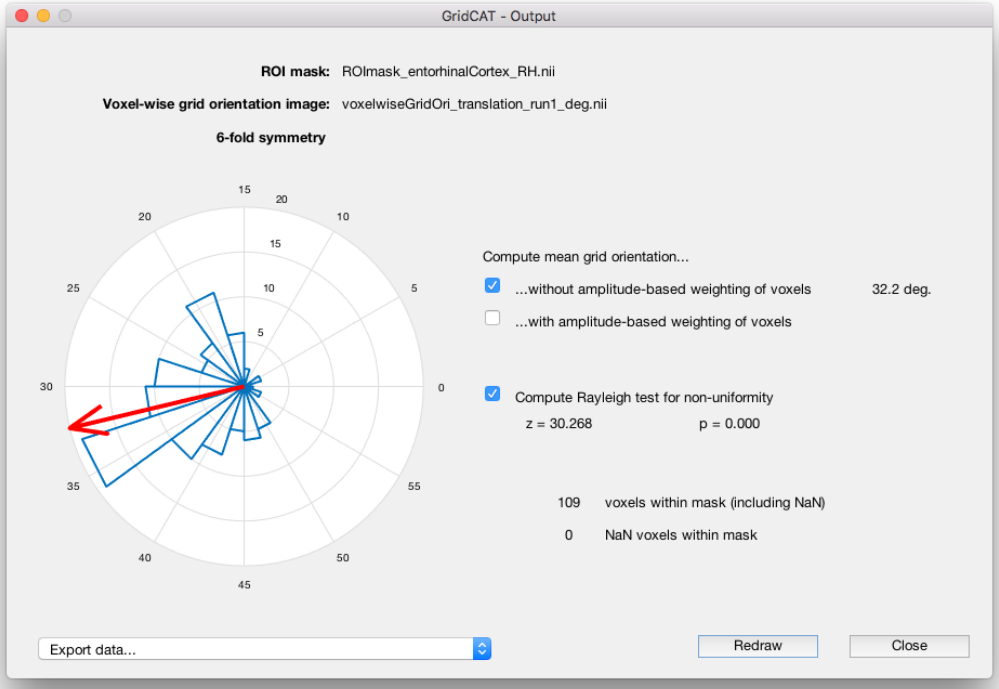

Figure 13: GridCAT dialog window for between-voxel orientation coherence

In an interactive dialog window, the GridCAT visualizes the between-voxel coherence of grid orientations within an ROI in a polar histogram plot. In addition, the mean grid orientation of all voxels within the ROI can be calculated and displayed. Rayleigh's test for non-uniformity of circular data can be carried out, in order to test for clustering of grid orientations. Results and underlying data (i.e., voxel-wise orientation values) can be exported, in order to conduct additional analyses and/or statistical tests.

By default, the orientation of the grid code in a voxel is considered stable if the two values are within ±15° of one another (i.e., the same threshold used in Kunz et al., 2015), and the GridCAT outputs the proportion of voxels within an ROI surviving this threshold. The stability of individual voxels is also displayed via the color of the connecting line; here, the GridCAT has displayed stable voxels in green and unstable voxels in red. Consistent with Kunz et al. (2015), the grid orientation for the example participant was consistent across the two runs, such that 75% of voxels in the right entorhinal cortex, and 60% of voxels in the left entorhinal cortex, maintained a stable orientation. The GridCAT provides the user with several other options in an interactive plot (**Figure 15**), including the

ability to change the threshold value for stability (i.e., ±15°) if the researcher wishes to be more conservative or liberal with this estimate. Moreover, the user can specify several aesthetics of the plot, such as the colors and styles of the lines and markers.

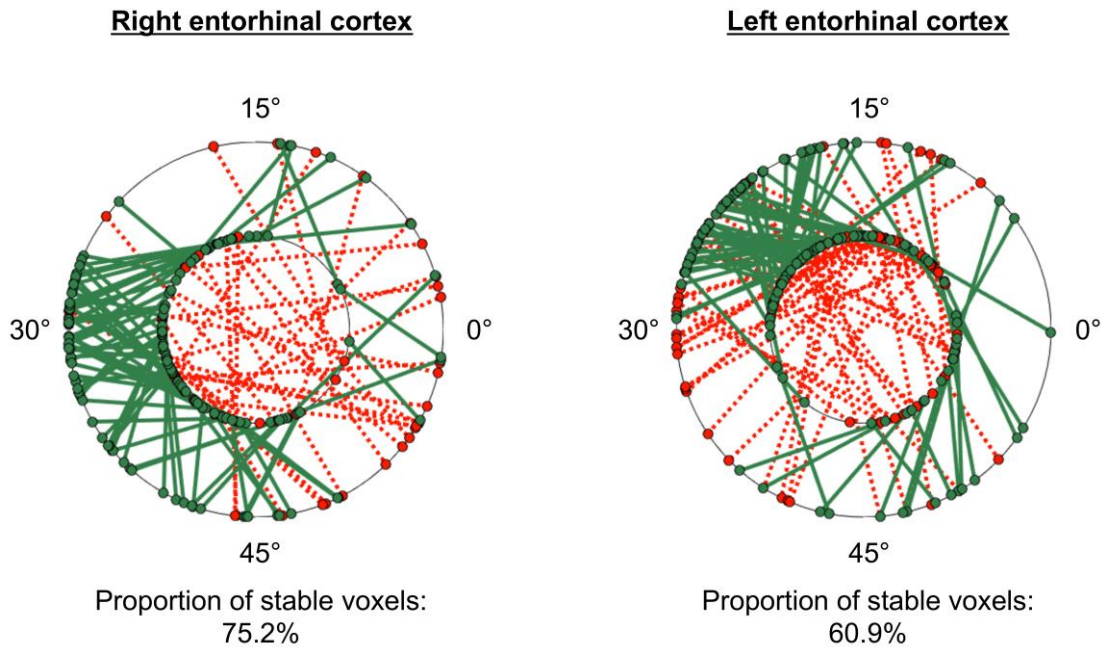

Figure 14: Within-voxel coherence of grid orientations

GridCAT polar plots showing coherence of the grid orientation within voxels, across runs 1 and 2, in right and left entorhinal cortex ROIs. In both the right and left entorhinal cortex, the majority of voxels maintained the same grid orientation (±15°) across the two runs; the proportion of voxels maintaining the same orientation across runs is calculated automatically for the user. The two black rings in each plot represent the two different runs (inner ring: run 1, outer ring: run 2), and the orientation of the grid code for each voxel is indicated with a circular marker; a line connects the orientations of each voxel. Green solid lines indicate voxels with stable orientations, whereas red dotted lines indicate voxels with unstable orientations. The GridCAT allows the user also to customize the plots, including the color schemes, line styles, as well as adapting the threshold for classifying a voxel as stable.

For the test data in GLM2, the GridCAT allows users to model grid events either with a parametric modulation regressor (e.g., Doeller et al., 2010), or by separating grid events into trials aligned versus misaligned with the mean grid orientation and contrasting these values ("aligned > misaligned"; see Section 2.2.6 for more details).

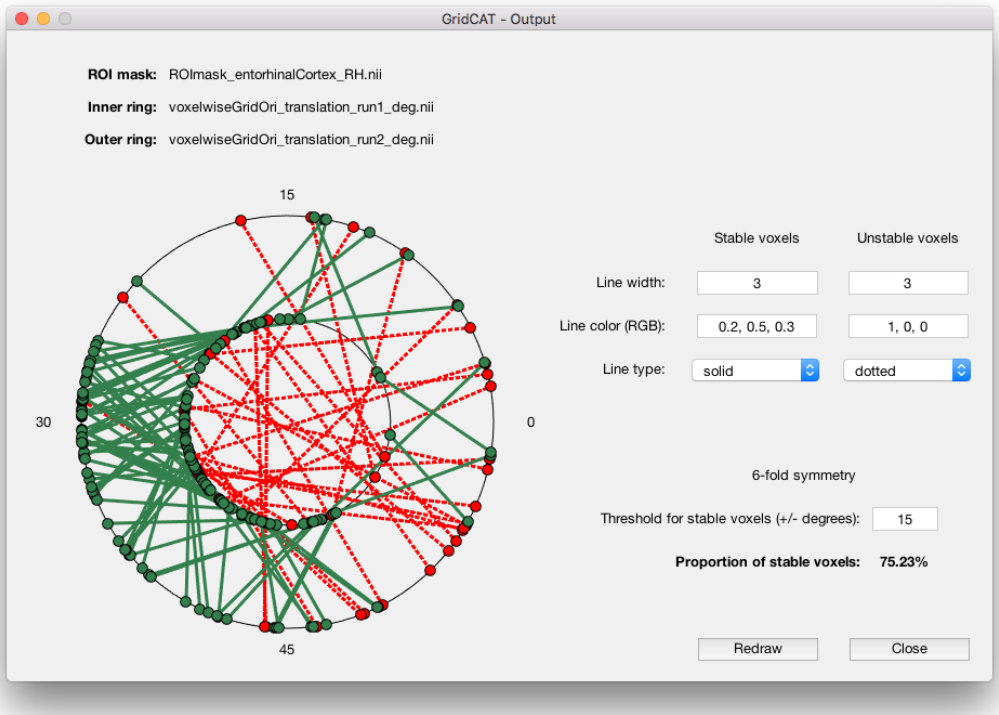

Figure 15: GridCAT dialog window for within-voxel orientation coherence

The within-voxel coherence of grid orientations can be visualized by the GridCAT. The proportion of stable voxels within an ROI is calculated automatically, and the stability-threshold for this calculation can be individually adapted, depending on the user's needs and research questions. Moreover, the several aesthetics of the plot can be specified and changed, such as the colors and styles of the lines and markers.

The two methods resulted in comparable parameter estimates in the right entorhinal cortex ROI, with the "aligned > misaligned" contrast method associated with slightly higher parameter estimates relative to the parametric modulator (see **Figure 16**). In the left entorhinal cortex, there were less obvious differences between methods, however the "aligned > misaligned" contrast again yielded the highest parameter estimate, but only when the mean average grid orientation was calculated using the data from both runs in GLM1. That the grid code metrics appear generally stronger in the right hemisphere, in terms of between-voxel and within-voxel grid orientation coherence, and model fit in GLM2, supports previous findings (Doeller et al., 2010). It is unclear from a theoretical viewpoint, however, why this should be the case, and requires more

extensive comparisons within individual subjects to determine the consistency of this effect.

The control analysis tests for the fit of different symmetrical models, to examine whether the six-fold symmetry explains best the data. Consistent with the other results reported here, in right entorhinal cortex the six-fold symmetrical model resulted in the numerically highest parameter estimates relative to all other models. In the left entorhinal cortex, the six-, seven-, and eight-fold models all appear to fit the data equally well (**Figure 16**). It should be noted, however, that other papers reporting a better fit of the six-fold symmetrical model show effects at the group-level, rather than within individual subjects. Accordingly, there may be substantial variability in these estimates both inter-subject, as well as intra-subject, as demonstrated here by the difference between right and left hemispheres.

2.4 Discussion

The GridCAT is an open-source toolbox allowing researchers to examine the putative firing of grid cells (i.e., the grid code) in human fMRI data. The GridCAT provides a simple and user-friendly GUI, and accompanying open-source code, for the analysis of fMRI data, so that the user can conduct the entire grid code analysis pipeline. In order to learn and understand the functionality of the GridCAT, a detailed manual is provided to guide the user through all analysis steps, and the user can also follow the instructions to analyze an example dataset and reproduce the results presented here. Furthermore, example scripts are provided for those who do not want to use the GUI, but rather use and modify the existing open-source code of the GridCAT. The Support section of NITRC also provides a platform for discussion of issues relating to the toolbox, as well as the opportunity for users to submit any requests or report errors regarding the GridCAT.

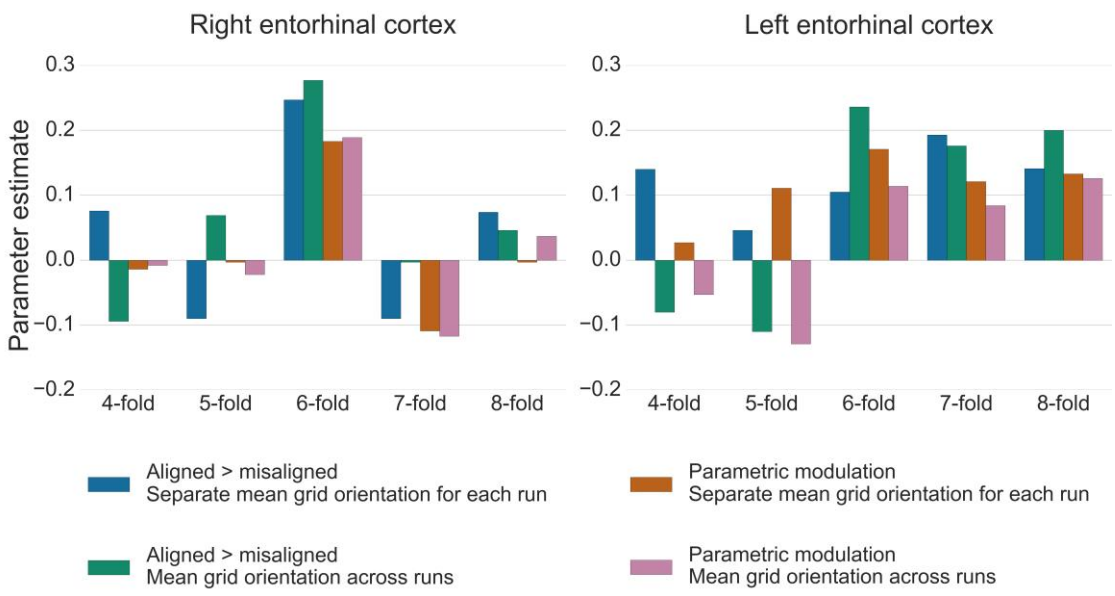

Figure 16: Parameter estimates from GLM2 associated with grid events using different model designs and grid code symmetries

In the right entorhinal cortex, the six-fold symmetrical model provided the best model fit, both for the "aligned > misaligned" contrast and for the single parametric modulation regressor. Calculating the mean grid orientation over two runs, versus using separate mean grid orientations for each run, made little difference to the parameter estimates. In the left entorhinal cortex, the effect of generating the mean grid orientation over multiple runs versus separate single runs was more variable and other symmetrical models provided equally good model fits for this hemisphere. All bars show the mean parameter estimate averaged over all voxels within the right and left entorhinal cortex, respectively.

Despite the great deal of research into grid cells using non-human animal species (for an overview see Rowland et al., 2016), there remain very few studies examining grid codes in human fMRI. Given that this cellular mechanism is now purported to support more than just pure spatial navigation behavior (Constantinescu et al., 2016; Julian et al., 2018; Nau et al., 2018), researchers now face the exciting challenge of elucidating exactly what role the grid code may play in other cognitive domains.

In humans, the architecture of grid cells is unknown, and it remains unclear whether there are multiple different grid codes (derived from the fMRI signal) that represent different types of information across the brain. For example, in terms of spatial navigation, in rodents there is evidence that grid cells are arranged in

different modules, with neurons within a module sharing a similar firing amplitude, preferred orientation, and spatial scale (Stensola et al., 2012). Although we can only study changes in signal at the macroscopic-level using fMRI, analysis of higher resolution imaging data, which would be supported also by the GridCAT, may reveal heterogeneity of the grid code within a single ROI (reflecting these different properties of grid cell modules). Furthermore, voxels showing a sinusoidal pattern in the BOLD signal have been identified across the brain in human fMRI studies (e.g., Constantinescu et al., 2016). It is unclear whether this activity in different brain regions reflects the same underlying process, or different types of information. Future studies in humans using different experimental paradigms and different imaging resolutions will help to elucidate whether the grid code is homogenous across the brain, or shows functional specialization.

Reproducing the grid code analyses from previous studies is a time-consuming and non-trivial endeavor that involves advanced computer programming and mathematical skills. The GridCAT, therefore, opens up this cutting-edge research area to researchers less comfortable with programming by allowing users to analyze data using a GUI. Because the open-source code for the GridCAT is available in the download, it can be adapted and extended as desired by the user. To do this, the user would need to be competent in MATLAB programming skills (either in MATLAB's proprietary programming language, or in other MATLAB-compatible programming languages such as C or Fortran), have a MATLAB license, and download the freely available SPM12 toolbox (http://www.fil.ion.ucl.ac.uk/spm/). Extensively commented example scripts are delivered with the GridCAT's open-source code that show how functions and algorithms are programmatically called in the course of the grid code analysis pipeline. Furthermore, they also demonstrate how new functions and algorithms can be added to the GridCAT.

Relative to other standard fMRI analysis software packages, the unique contribution of the GridCAT is that it provides the algorithms necessary to detect the grid code in the BOLD signal, and that it synthesizes analysis pipelines that

have been used previously. Specifically, these include different ways in which the data can be partitioned for GLM1 and GLM2, using either the GridCAT's automated, or a user-defined partitioning scheme. The GridCAT then automatically estimates voxel-wise orientations of the grid code from the BOLD signal. Using these orientation values, the magnitude of grid code response can be calculated, as well as grid code metrics such as within- and between-voxel orientation coherence. Results can be visualized by using specific plotting tools offered by the GridCAT. Furthermore, it offers the option to statistically test for non-uniformity or clustering of voxel-wise grid orientation data, which has been used in previous grid code publications but is not commonly included in standard statistical software packages. Moreover, all data generated by the GridCAT can be exported using its data export tools, providing flexibility in terms of further statistical testing, comparisons, and visualization, depending on the individual research questions and the researcher's needs.

As noted above, although it is beyond the scope of this project to compare the results of all different model selection parameters, we believe that this is an important goal for the field so that researchers will have a better idea as to the factors that aid detection of these signals in fMRI data. By making all of these options available to the user, and the wider neuroscience community, the GridCAT has provided the first step in achieving this goal and has the potential to accelerate grid code research in humans.

2.5 License statement

The GridCAT is openly available at the Neuroimaging Informatics Tools and Resources Clearinghouse (NITRC) and can be downloaded from: http://www.nitrc.org/projects/gridcat

The GridCAT is free software and can be redistributed and/or modified under the terms of the GNU General Public License as published by the Free Software Foundation, either version 3 of the License, or (at your option) any later version.

A copy of the GNU General Public License is distributed along with the GridCAT, or can be found online at: http://www.gnu.org/licenses/

2.6 Contributions and acknowledgements

Matthias Stangl (MS) carried out this project in a collaborative effort with Jonathan Shine (JS) and Thomas Wolbers (TW). MS, JS and TW conceptualized the toolbox. MS implemented and designed the toolbox. MS and JS acquired the data. MS analyzed the data and visualized the results. MS and JS drafted the manuscript (Stangl et al., 2017). All authors edited the manuscript. MS wrote the GridCAT's user manual. TW supervised the work.

We express our gratitude to Denise Scheermann and Claus Tempelmann for their help with data acquisition.

This work was supported by the European Research Council Starting Investigator Grant AGESPACE (335090) and by the Collaborative Research in Computational Neuroscience Grant (01GQ1303) of the German Ministry of Education and Research (BMBF).

3. PROJECT B

Grid-cell-like representations in old age

The output of this project has been previously published as an Open Access article (together with output from Project C) in the journal "*Current Biology*" (Stangl et al., 2018). While all results presented here stay unchanged to the original publication, some paragraphs, figures, and corresponding figure captions have been edited, in order to meet the structure, scope, and formatting standards of this thesis. Moreover, this thesis contains some additional figures and paragraphs that were not included in the original publication due to the journal's limitations regarding text length and number of display items.

3.1 Project introduction

Numerous studies have reported a progressive loss in a broad range of navigational abilities with aging, but we have only a limited understanding of the neuronal mechanisms underlying this decline (Lester et al., 2017). As grid cells in the entorhinal cortex are a central component of the brain's navigation circuit (Rowland et al., 2016), impaired grid cell firing could, theoretically, provide a mechanistic explanation for navigational deficits in old age. To date, however, it is unclear whether the firing properties of entorhinal grid cells change in the course of aging.

Despite the lack of studies investigating effects of healthy aging on grid cell function, several related findings suggest that the grid cell system might be compromised in old age: First, as discussed in more detail in Section 1.2.2 of this thesis, it is known that the entorhinal cortex is particularly vulnerable to neurodegenerative processes during aging and Alzheimer's disease (Braak & Braak, 1991; Gómez-Isla et al., 1996; Du et al., 2001; Pennanen et al., 2004; Masdeu et al., 2005; Stranahan & Mattson, 2010; Fjell et al., 2014; Khan et al.,

2014). Given that the entorhinal cortex has been identified as the primary location of grid cells (Hafting et al., 2005), there is reason to believe that age-related neurodegenerative processes also affect grid cell function. And indeed, Fu et al. (2017) recently found that tau pathology (indicative of Alzheimer's disease) in old mice induced both spatial memory deficits and impaired grid cell firing.

Second, studies have demonstrated age-related changes in the firing properties of hippocampal place cells (Barnes et al., 1997; Wilson et al., 2006; Schimanski et al., 2013). The entorhinal cortex is known to be a major input source to the hippocampus, and a number of theoretical studies suggested that the firing pattern of hippocampal place cells might be driven by input from the grid cell system (O'Keefe & Burgess, 2005; Fuhs & Touretzky, 2006; Solstad et al., 2006; Rolls et al., 2006; Hayman & Jeffery, 2008; Molter & Yamaguchi, 2008; de Almeida et al., 2009; Si & Treves, 2009; Hasselmo, 2009; Savelli & Knierim, 2010; Monaco & Abbott, 2011; Lyttle et al., 2013). In fact, studies have reported coordinated temporal dynamics of entorhinal grid cells and hippocampal place cells (Fyhn et al., 2007), and impaired place cell firing due to entorhinal cortex lesions (Brun et al., 2008). Cumulatively, these findings indicate that grid cell activity – at least to some extent – is associated with or might even drive place cell firing, and that observed age-related impairments in place cell firing might be a consequence of deficient information from a compromised grid cell system that is fed forward from the entorhinal cortex to the hippocampus.

In sum, the results of these studies give rise to the hypothesis that the grid cell system might be compromised in old age. In this project, we therefore measured the putative firing of grid cells (i.e., grid-cell-like representations) in young and older humans using fMRI, while they performed a virtual navigation task. Grid-cell-like representation magnitudes as well as further properties of grid-cell-like representations, such as their spatial and temporal stability, were quantified for each participant individually and compared between young and older adults, in order to investigate whether there is evidence for age-related impairments in grid cell function. Moreover, we ran a series of control analyses in order to test

whether age-related changes in grid-cell-like representations can be explained by alternative and confounding factors, such as behavioral and neurophysiological differences between young and older adults, unrelated to grid cell function per se.

3.2 Method

3.2.1 Participants

41 healthy humans took part in this study. The group of young adults consisted of 20 participants (10 woman, 10 men) aged between 19 and 30 years (M = 24.5, SD = 3.3 years), whereas the group of older adults consisted of 21 participants (11 woman, 10 men) aged between 63 and 81 years (M = 69.3, SD = 4.8 years). Only participants with no reported history of neurological or psychiatric disease and no reported motor deficits during normal walking or standing took part in this study. All participants reported right-handedness and had normal or corrected-to-normal eyesight.

Informed consent was obtained from all participants in writing before the measurements, and the experiment received approval from the Ethics Committee of the University of Magdeburg.

Prior to the study, all participants underwent the Montreal Cognitive Assessment (MoCA) screening tool for mild cognitive impairment (Nasreddine et al., 2005). Participants who did not exceed a MoCA cut-off score of 23 (following Luis et al., 2009) were excluded from the study and did not participate in any further measurements.

3.2.2 Object-location memory task

Grid-cell-like representations in humans, reflecting the 6-fold symmetric grid cell firing pattern routinely seen in electrophysiology studies, can be measured by fMRI during navigation in virtual environments (Doeller et al., 2010; Kunz et al.,

2015; Horner et al., 2016). Here, participants performed an object-location memory task in a virtual environment (**Figure 17**), using an MR-compatible joystick (Tethyx, Current Designs, www.curdes.com). Given that older adults often have less experience in using computers and gaming (Kelley & Charness, 1995), the task was designed to be relatively simple in order to allow for similar task performance between young and older adults. In this task, participants were asked to complete multiple trials in a square virtual room with the dimensions 160 x 160 vm, in which three target objects (soccer ball, plant, trash bin) were placed in random locations. Each trial had the following structure: At the start, all target objects disappeared, and a cue image of one target object was shown at the bottom of the screen. Participants were asked to navigate to the position of the cued target object and confirm their choice of location with a button-press. After the button-press, the so-called "error distance" (i.e., the Euclidean distance between the target object's correct location and the participant's response) was calculated automatically as an indicator for the accuracy of the response (**Figure 18**). Feedback was given to the participant via a smiley-face displayed on the screen that was either green (if the error distance between the correct location and the participant's response was below 20 vm), or yellow (for error distances between 20 and 30 vm), or red (for error distances larger than 30 vm). If the error distance was larger than 20 vm, the target object reappeared and had to be collected, allowing for (re-)encoding of its correct location. After each trial, the participant was automatically transported to a random position within the virtual room before the next trial started.

Participants were explicitly instructed that the main goal during the task was to complete as many trials as possible while attempting to always get green smiley face feedback (i.e., as a response to error distances below 20 vm), but not to focus on being as accurate as possible (i.e., avoiding to spend time on fine tuning of their position at presumed target locations). The order of trials was pseudo-randomized, but the same order was used for all participants. Movement speed was constantly set to 15 vm per second, and it was not possible to make translational and rotational movements at the same time (i.e., it was not possible to walk curves but just straight lines). Rotation speed was constantly set to 50

degrees per second. Height of the virtual camera was set to 1.7 vm. The object-location memory task was developed using the WorldViz Vizard 5.1 Virtual Reality Software (WorldViz LLC, www.worldviz.com).

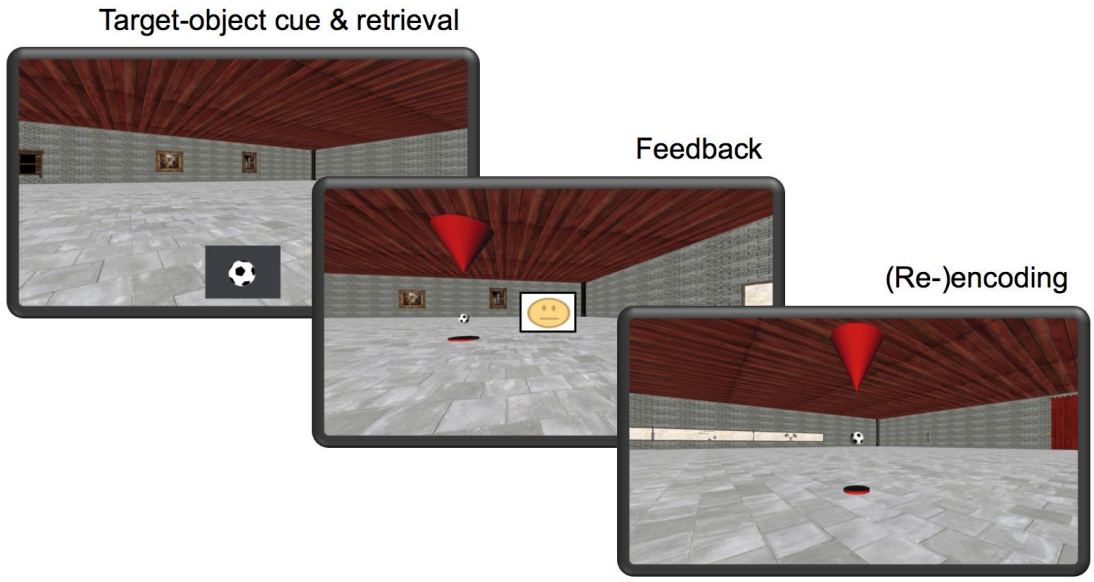

Figure 17: Example trial of the object-location memory task

First, all target objects disappeared, and a cue image of one target object was shown (e.g., a soccer ball). Participants navigated to the position of the cued target object and confirmed their choice of location with a button-press. A smiley face provided feedback as to the accuracy of the response. Participants were instructed to aim for green smiley face feedback (error distances < 20 vm), and avoid yellow smiley faces (error distances 20 to 30 vm) or red smiley faces (error distances > 30 vm). If the error distance was larger than 20 vm, the target object reappeared and had to be collected, allowing for (re-)encoding of its correct location. After each trial, the participant was automatically transported to a random position within the environment before the next trial started.

In order to learn step-by-step how to navigate a virtual environment using a joystick and how to perform the object-location memory task, all participants underwent an extensive preparatory session on a separate day before fMRI scanning. During the preparatory session, participants first got familiarized with joystick control by completing several training tasks in a different virtual environment. They were asked to freely navigate a virtual environment in a circular outdoor-arena with a diameter of 250 vm, enclosed by a wall and surrounded by a mountain range (see **Figure 19A**).

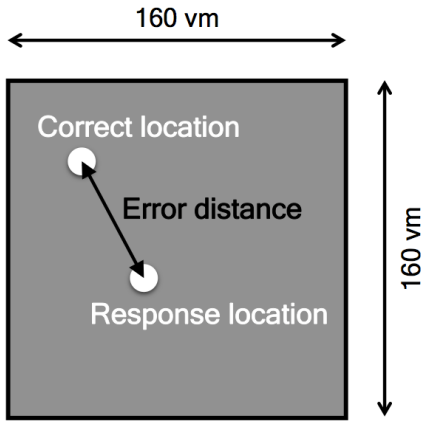

Figure 18: Calculation of accuracy in the object-location memory task

Multiple trials of the object-location memory task were performed in a virtual environment that had the dimensions 160 x 160 vm. In each trial, participants had to navigate to the location of one cued target object. Task accuracy was expressed for each trial by the "error distance", which was calculated as the Euclidean distance between the target object's correct location and the participant's response.

Then, they completed several training tasks in this environment, such as directly navigating to a cued object within the environment as quickly as possible (**Figure 19B**), or to navigate through a labyrinth of walls to find the cued object at the end of the track (**Figure 19C**). Subsequently, participants were familiarized with the procedure of the object-location memory task by performing several trials in a parallel task version, in which the procedure was identical to the fMRI scanning session, but the virtual room, target objects, and object locations were different (**Figure 19D**). Multiple trials were performed in this practice version of the task, until both the experimenter and the participant felt confident that the task was fully understood and could be performed correctly. Finally, participants performed the object-location memory task in the actual test version of the task (the same one they would later navigate during the fMRI scanning-session, including the same target objects and object locations; see also **Figure 17**). To ensure that each participant learned the target object locations with the required accuracy, this learning procedure continued until a participant identified each target object's location at least two times in a row with an error distance below 20 vm, and until they had received at least eight green smiley faces in a row. On the

day of scanning, to ensure that participants still remembered the location of the target objects, they first underwent another short block of trials outside the scanner, until they received five green smiley faces in a row. Then, each participant completed four runs of fMRI scanning while performing the object-location memory task. Each fMRI scanning run had a duration of 16 minutes.

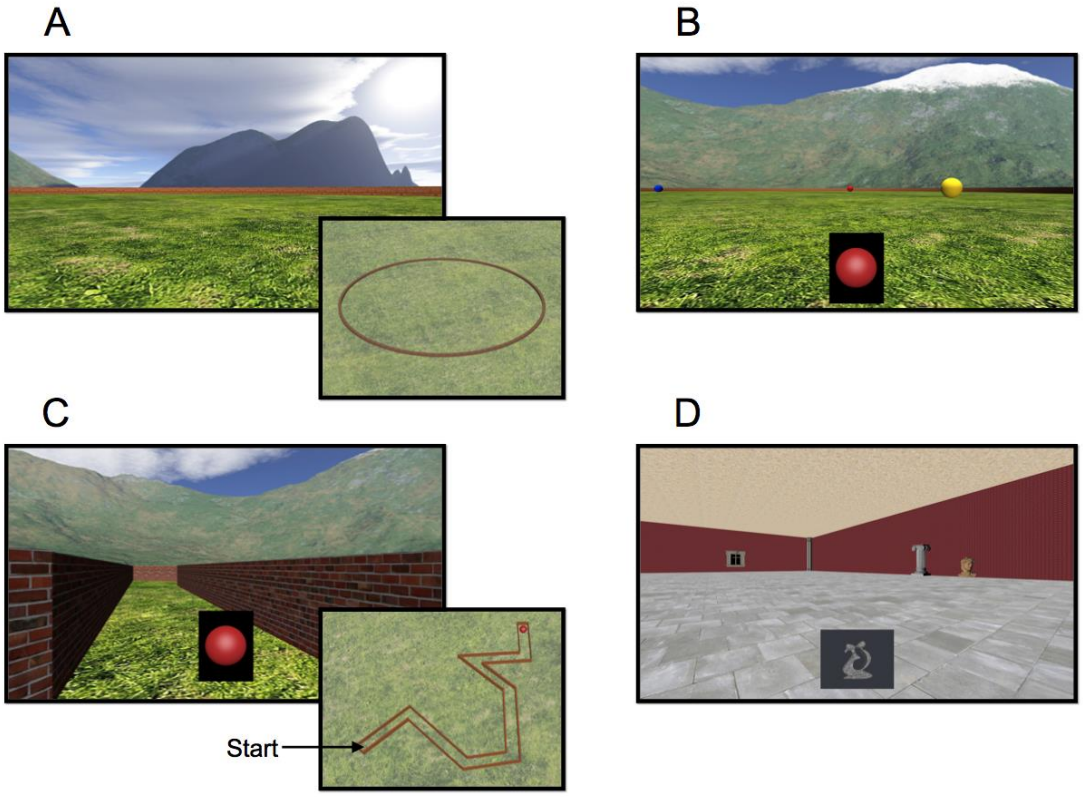

Figure 19: Virtual environments during preparatory session

A: *Circular arena surrounded by a mountain range from a first-person perspective (left) and birds-eye view (right; mountain range removed for display purposes).* ***B:*** *Example for a training task, in which participants had to navigate to a cued object within the environment as quickly as possible.* ***C:*** *Example for a training task, in which participants had to navigate from a starting point through a labyrinth of walls (shown left from a first-person perspective and right from birds-eye view) to find the cued object at the end of the track.* ***D:*** *Practice version of the object-location memory task.*

3.2.3 MRI scanning parameters

MRI data were acquired on a 3 Tesla Siemens Magnetom Prisma scanner equipped with a 64-channel phased array head coil. All sequences described below utilized parallel imaging with a GRAPPA acceleration factor of 2.

During the object-location memory task, T2*-weighted functional images were recorded with a partial volume EPI sequence with the following parameters: TR = 1500 ms, TE = 30 ms, slice thickness = 2 mm, in-plane-resolution = 2 x 2 mm, number of slices = 24, field of view = 216 mm, flip angle = 80°, slice acquisition order = interleaved. Slices were oriented parallel to the long axis of the hippocampus.

To facilitate an accurate co-registration of entorhinal cortex masks to partial volume EPI images, a whole brain EPI image was acquired with the following parameters: TR = 6000 ms, TE = 30 ms, slice thickness = 2 mm, in-plane-resolution = 2 x 2 mm, number of slices = 84, field of view = 216 mm, flip angle = 90°, slice acquisition order = interleaved. Slices were oriented parallel to the long axis of the hippocampus.

For manual delineation of the entorhinal cortex, a high-resolution T2-weighted structural image was acquired using a hyper echo TSE sequence with the following parameters: TR = 6000 ms, TE = 71 ms, slice thickness = 2 mm, in-plane-resolution = 0.5 x 0.5 mm, number of slices = 64, field of view = 224 mm, flip angle = 120°, slice acquisition order = interleaved. Slices were oriented orthogonal to the long axis of the hippocampus.

A structural T1-weighted image with isotropic resolution was acquired using an MPRAGE sequence with the following parameters: TR = 2500 ms, TE = 2.82 ms, inversion time (TI) = 1100 ms, slice thickness = 1 mm, in-plane-resolution = 1 x 1 mm, number of slices = 192, field of view = 256 mm, flip angle = 7°.

Moreover, a gradient-multi-echo sequence was acquired, which is not discussed here further.

3.2.4 fMRI data preprocessing

Functional images were realigned and smoothed with a 5 mm full-width-half-maximum gaussian kernel using SPM12 (http://www.fil.ion.ucl.ac.uk/spm/). In order to avoid spatial distortions or interpolation errors in the data resulting from normalization to a standard template, we did not apply normalization but images were further analyzed in each participant's native space.

3.2.5 Correction for head movement during scanning

Correction for head movement was performed at two levels: First, we applied the realignment algorithm of SPM12, which is specifically designed to account for head movement during fMRI scanning. This algorithm corrects for motion-related linear or angular displacement of scan images. Second, we included movement parameters for each scan volume (as calculated by the realignment algorithm) as regressors of no interest in every GLM that was carried out in order to calculate grid-cell-like representations. This approach corrects for movement-related signal artifacts (i.e. spin-history effects), so that other regressors in the GLM (e.g., like regressors testing for the 6-fold symmetric modulation) are not affected by movement-related changes of the BOLD signal.

3.2.6 Entorhinal cortex region of interest masks

Anatomical masks of the entorhinal cortex were traced manually on each participant's T2-weighted image using ITK-SNAP (http://www.itksnap.org/). For manual delineation of the entorhinal cortex (**Figure 20**), we followed the segmentation protocol of Berron et al. (2017). After manual delineation, ROI mask images were created using ITK-SNAP.

Together with the T2-weighted image, ROI mask images were co-registered to the participant's EPI data. Given that the EPI images were only partial volume slabs (see **Figure 21**, blue), the process of co-registering T2 images (**Figure 21**, grayscale) to the partial volume EPI images is non-trivial, as co-registration can only be computed on a relatively small portion of overlapping brain tissue

between the two different image modalities (**Figure 21**, red). Co-registration was therefore performed via one whole brain EPI image, in order to avoid co-registering images with little overlap of brain tissue, and consequently allow for a more accurate co-registration. This whole brain EPI image had similar imaging parameters as the partial volume EPI images, but a considerably higher TR to enable whole brain coverage (see Section 3.2.3). Co-registration of the T2 image to the partial volume EPI images included two separate steps: In a first step, the T2 image (together with the ROI masks) was co-registered to the whole brain EPI image. This co-registration step has the advantage that co-registration is facilitated by considerably more overlapping brain tissue between the two image modalities (i.e., T2 and whole brain EPI), as compared to directly co-registering the T2 image to the partial volume EPI images. In a second step, the whole brain EPI (together with the T2 image and ROI masks) was co-registered to the partial volume EPI images. This second co-registration step again has the advantage of more overlap between whole brain EPI and partial volume EPI images. Furthermore, whole brain EPI and partial volume EPI images share similar imaging parameters and therefore have widely similar properties, which also facilitates a more accurate co-registration.

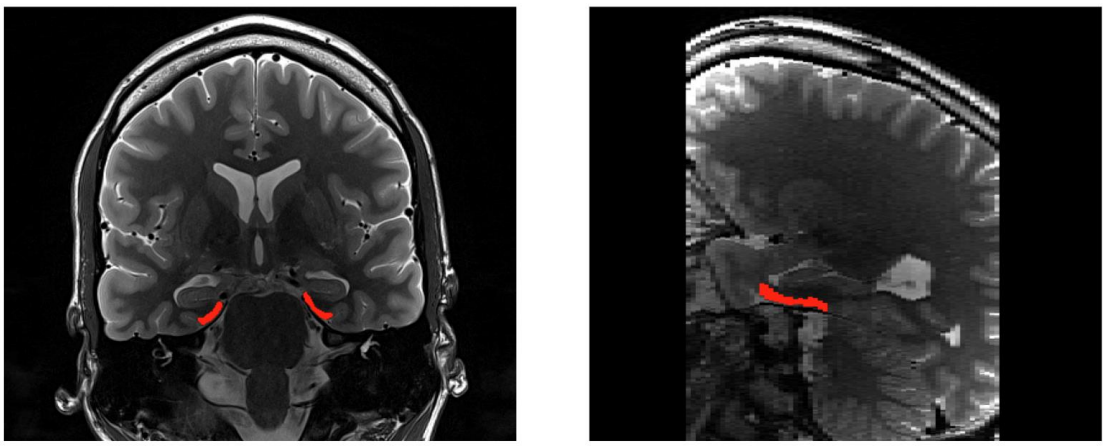

Figure 20: Entorhinal cortex region of interest mask

Example mask for the bilateral entorhinal cortex (red) of one participant, shown on the participant's individual T2-weighted structural image in coronal (left) and sagittal (right) view.

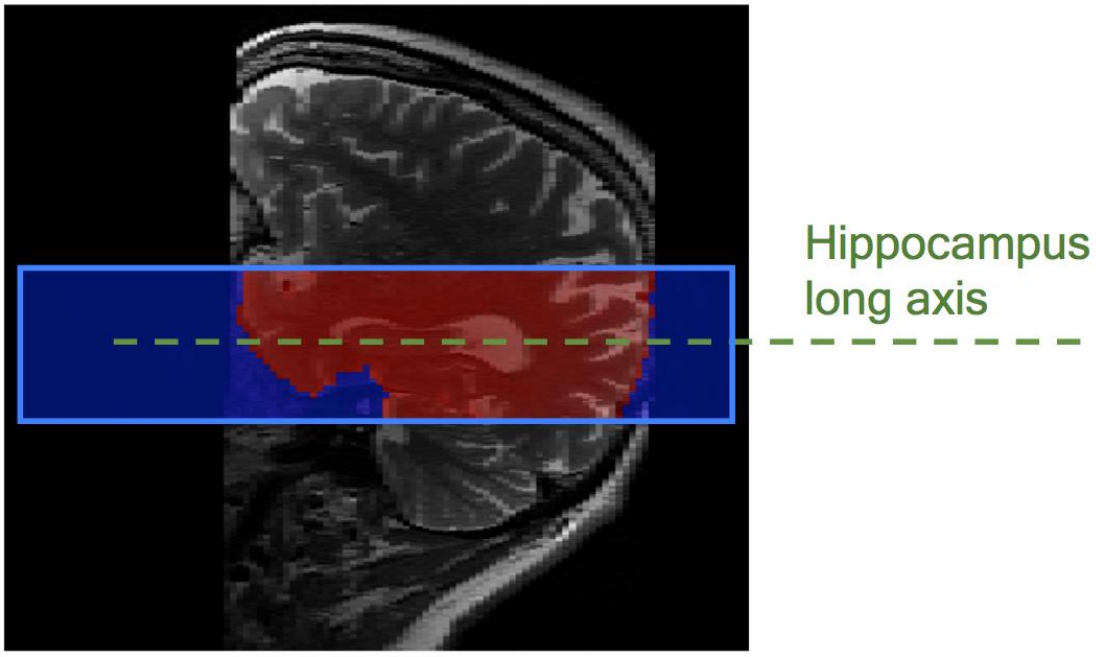

Figure 21: Overlap between partial volume EPI image and T2-weighted structural image

Partial volume size and orientation of an EPI image (blue) shown on the T2-weighted structural image (grayscale) of one participant in sagittal view. Overlap between partial volume EPI and T2 image is shown in red. Slices of the T2 image were acquired orthogonal to the long axis of the hippocampus (indicated by the green dashed line), whereas slices of partial volume EPI images were oriented parallel to the long axis of the hippocampus.

3.2.7 Analysis of grid-cell-like representations

For the analysis of grid-cell-like representations, we used the Grid Code Analysis Toolbox (GridCAT) with MATLAB 2016b (The MathWorks, Natick, MA, USA). The MATLAB source code that was used to carry out this analysis is freely and openly available (Stangl et al., 2017). The analysis followed the procedure of Doeller et al. (2010). First, we partitioned the four fMRI scanning runs into two data halves, using the first half of each scanning run as the estimation dataset and the second half of each scanning run as test dataset (**Figure 22**). Then, we estimated voxel-wise grid orientations by fitting the estimation data to a first general linear model (GLM1). This model included two parametric modulation regressors for all translation events, using $\sin(\alpha_t*6)$ and $\cos(\alpha_t*6)$, respectively,

where α_t represents an event's translation direction within the virtual environment. We then calculated the mean grid orientation (φ) within entorhinal cortex voxels, by averaging the beta estimates (β_1 and β_2) associated with the two parametric modulation regressors over all voxels in the left and right entorhinal cortex, and submitting the resulting two values to: $\arctan[\text{mean}(\beta_1)/\text{mean}(\beta_2)]/6$. Then, the remaining half of the data (test dataset) was modeled in a second general linear model (GLM2). This model included a parametric modulation regressor for all translation events, calculated by taking each event's translation direction (α_t), and determining its difference from the mean grid orientation (φ) by calculating $\cos[6*(\alpha_t - \varphi)]$. Finally, the magnitude of grid-cell-like representations in the entorhinal cortex was quantified by the average parametric modulation regressor's parameter estimates within entorhinal cortex voxels. Based on these model specifications, magnitudes of grid-cell-like representations are expected to be positive for changes in mean grid orientation of less than ±15° between data halves, or negative for changes of more than ±15°, given that grid orientations range from 0° to 60° and therefore the maximally detectable change in grid orientation is 30°.

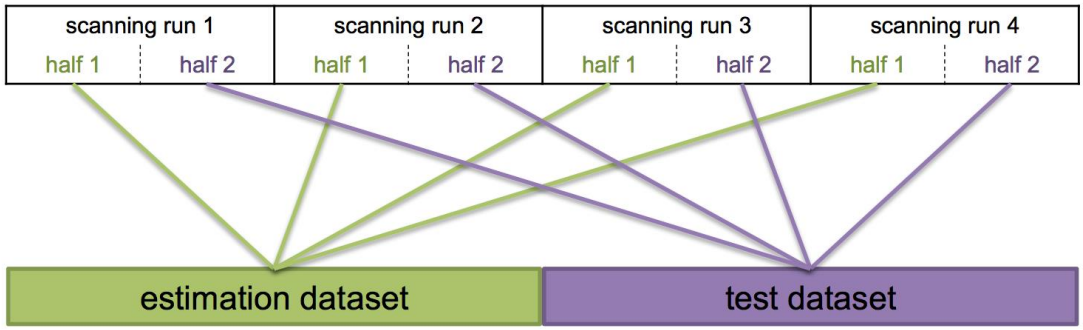

Figure 22: fMRI data partitioning scheme for the analysis of grid-cell-like representations

fMRI data were acquired in 4 consecutive scanning runs. For the analysis of grid-cell-like representations, data were partitioned in two data halves: an estimation dataset and a test dataset. The estimation dataset comprised the data from the first half of each scanning run and was used for estimating voxel-wise grid orientations in GLM1. The test dataset comprised the data from the second half of each scanning run and was used for testing the estimated grid orientations in GLM2 and for calculating the magnitude of grid-cell-like representations.

Importantly, in both GLM1 and GLM2, only translation events but not other events (such as stationary periods) were parametrically modulated by sine/cosine regressors with respect to their translation direction, in order to ensure that the calculation of voxel-wise grid orientations and magnitudes of grid-cell-like representations was only based on modeling events during which participants performed translational movements in the virtual environment.

In all GLMs, we included as regressors of no interest head motion parameters (x, y, z, yaw, pitch, and roll) derived from realignment in SPM12, the unused grid events (i.e., the parametrically modulated translation events for GLM2 when fitting GLM1, and vice-versa), and the feedback phase in the object-location memory task. Very short translation events (duration < 1 sec) were not modeled in the GLMs.

3.2.8 Analysis of representational stability

The ability to detect grid-cell-like representations in fMRI can be affected by the homogeneity of the estimated grid orientations across voxels within an ROI (i.e., spatial stability). Specifically, if all voxels within an ROI provide a different orientation value (i.e. high spatial instability), then the resulting mean grid orientation would be random, and the coding of translation events in GLM2 (in which translation events are modeled with respect to the deviation between their translation direction and the mean grid orientation), would then be arbitrary, resulting in a reduced grid-cell-like representation magnitude. Alternatively, an inability to detect grid-cell-like representation in the fMRI signal could result from instability of the estimated grid orientations over time (i.e., temporal stability).

Calculation of metrics for spatial and temporal stability of each participant's grid-cell-like representations followed the methods described in Kunz et al. (2015) and Stangl et al. (2017): In order to obtain a metric of spatial stability, we calculated the coherence of estimated voxel-wise grid orientations between all entorhinal cortex voxels by submitting the orientation values to Rayleigh's test for non-uniformity of circular data. Spatial stability is then statistically expressed by the resulting Rayleigh's z-value (with higher z-values indicating higher spatial

stability). To calculate temporal stability, we first estimated voxel-wise grid orientations for each half of a scanning run separately. For each individual voxel, we then compared the orientation between first and second data half, and classified each voxel's orientation as "stable" if the orientations were within ±15° of one another. Temporal stability is then indicated by the average proportion of stable voxels within the entorhinal cortex across all scanning runs. In a separate analysis using an alternative measure of temporal stability, we calculated the absolute change in grid orientation between data halves for each voxel separately, and then calculated the average change in orientation across all entorhinal cortex voxels.

3.2.9 Control analyses

Analyzing the behavioral data of the object-location memory task revealed that, relative to young adults, older adults spent more time per trial standing still and rotating in the virtual environment, which in turn led to a lower total duration of translation phases in older adults (see Section 3.3.2 for more details). Given that translation phases were used for the analysis of grid-cell-like representations (as described in Section 3.2.7), we re-analyzed grid-cell-like representations in young adults using only a proportion of their translation data, in order to match the data amount of older adults. Specifically, the amount of translation data we acquired from older adults was on average 80.16 percent of the data from young adults. Two different ways of reducing the data were implemented in two separate control analyses: First, we shortened each scanning run of young adults by discarding the last part of each run so that only 80.16 percent of translation data were taken into account. Second, we shortened each individual translation phase and modeled only the first 80.16 percent of each phase in a participant's GLMs to analyze grid cell-like representations.

Since there is evidence that task performance in fMRI studies might modulate age differences in brain activation (Nagel et al., 2009), we also checked whether accuracy in the object-location memory task had an impact on grid-cell-like representations. For these control analyses, task performance was quantified by

each participant's average error distance across all trials in the object-location memory task.

It has been shown that a reduction in entorhinal cortex volume might occur during both pathological and healthy aging (Fjell et al., 2014). Such a volume reduction in older adults could, theoretically, drive an age effect in grid-cell-like representations, as a reduced number of entorhinal cortex voxels might lead to a less reliable estimation of grid orientations and, consequently, to reduced temporal representational stability. We therefore checked whether entorhinal cortex volume might account for differences in grid-cell-like representation magnitudes between age groups. Entorhinal cortex volume was quantified by the number of entorhinal cortex voxels in each participant's individual T2-weighted structural image.

We also tested whether differences in grid-cell-like representations between young and older adults might be a general effect of lower fMRI signal quality in the entorhinal cortex of older adults. As an indicator for signal quality, we calculated the temporal signal-to-noise ratio (tSNR) within the entorhinal cortex of each participant. tSNR was quantified by the mean signal within the entorhinal cortex divided by the standard deviation of this signal over time.

In order to test whether head movement during fMRI scanning might account for differences in grid-cell-like representation magnitudes between age groups, we calculated each participant's average linear and angular displacement per scan volume. Motion parameters were extracted from the realignment procedure in SPM12, which specifically quantifies both linear and angular head movement during scanning. Individually for each participant, we calculated the sum of displacement per scan in all three linear dimensions (x + y + z) and then calculated the average linear displacement per scan across the fMRI time series. The same procedure was performed for angular displacement (yaw + pitch + roll).

3.2.10 Quantification and statistical analysis

All statistical analyses were carried out using MATLAB 2016b and the Statistics and Machine Learning Toolbox for MATLAB 2016b. Correlation values, where given, are Pearson correlations. Error bars in figures indicate standard errors of the mean (SEM). Statistical analyses were performed using a significance threshold of $p < 0.05$.

We used one-sample t-tests in order to test whether magnitudes of grid-cell-like representations (6-fold model) or symmetrical models with different periodicities (5-/7-fold) were significantly different from zero.

In young adults, paired-sample t-tests were used to compare magnitudes of grid-cell-like representations in the reduced translation data models versus the full data model.

Group comparisons between young and older adults were carried out using two-sample t-tests.

3.3 Results

3.3.1 Grid-cell-like representations in young and older adults

Before fMRI scanning, all participants received extensive pre-training in a preparatory session to ensure that they were able to continuously retrieve all target object locations with an error distance below 20 vm. This procedure proved successful, because the average error distance across all trials during fMRI scanning was below 20 vm for all participants, showing that they were able to perform the task with the required accuracy (**Figure 23**).

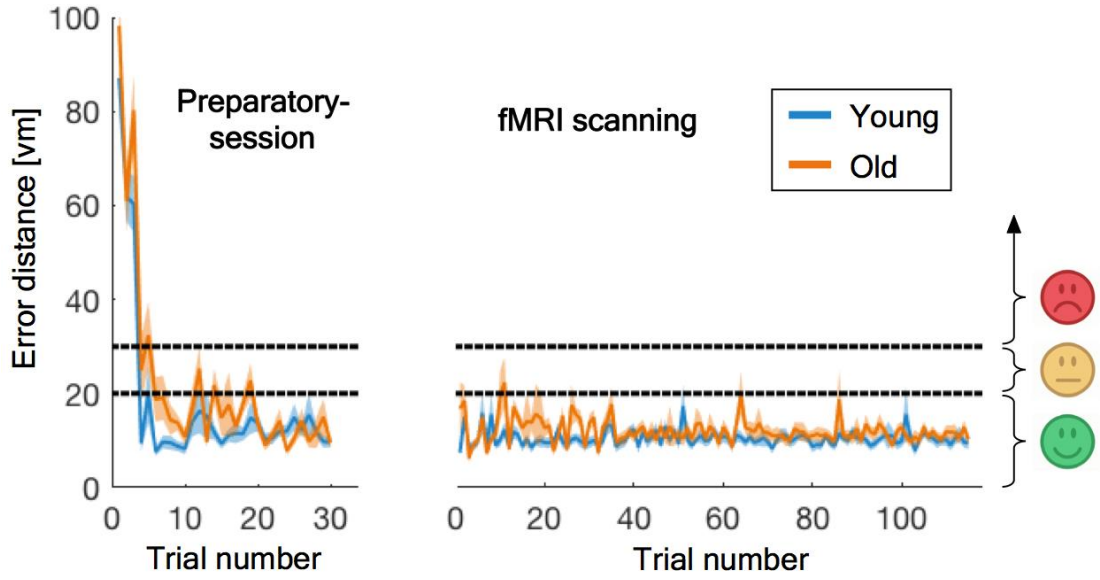

Figure 23: Task accuracy in the object-location memory task

After having learned the target object locations in the preparatory session (left panel), both young and older adults were able to perform the task with required accuracy during fMRI scanning (right panel). Blue and orange lines indicate group mean ± SEM; black dashed lines indicate error distance thresholds for different smiley face feedback. Plots show the first 30 trials of the preparatory session and 115 trials for fMRI scanning, which are the minimum numbers of trials that all participants completed.

For the analysis of grid-cell-like representations, fMRI data were split in two halves, using the first half to estimate voxel-wise grid orientations in the bilateral entorhinal cortex, and then testing these orientations on the other half of the data in order to quantify the magnitude of each individual participant's grid-cell-like representations. This procedure revealed a significant magnitude of grid-cell-like representations in the entorhinal cortex of young adults (**Figure 24A**). Specifically, this effect was only significant for the 6-fold symmetrical model (t_{19} = 3.71, p = 0.002), whereas effects in control analyses applying symmetrical models with different periodicities (**Figure 24B**) were not significantly different from zero (5-fold: t_{19} = 0.02, p = 0.983; 7-fold: t_{19} = 0.23, p = 0.822). Furthermore, we found that the magnitude of grid-cell-like representations in older adults was significantly reduced compared to young adults (t_{39} = -2.66, p = 0.011). In fact, we did not find any significant effect of grid-cell-like representations in older adults, either for the 6-fold symmetrical model (t_{20} = -

0.79, p = 0.438) or for the control models testing for other periodicities (5-fold: t_{20} = -0.08, p = 0.940; 7-fold: t_{20} = -0.62, p = 0.544).

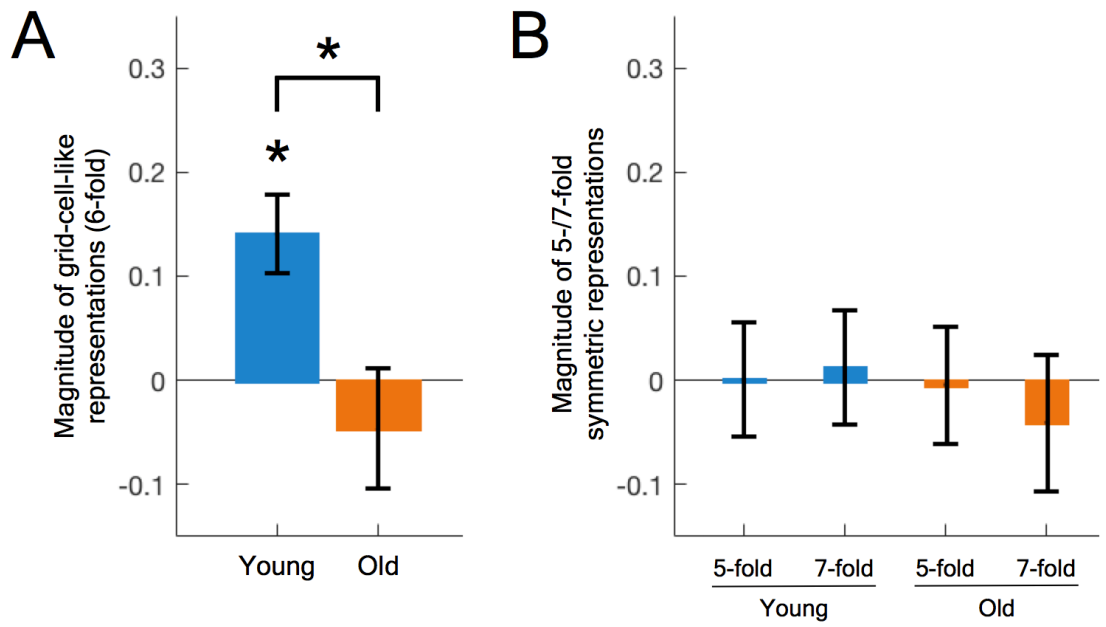

Figure 24: Grid-cell-like representations in the entorhinal cortex of young and older adults

A: *Higher magnitude of grid-cell-like representations in young relative to older adults. The magnitude of grid-cell-like representations in older adults was not significantly different from zero.* ***B:*** *In control analyses for different symmetrical models (5-fold/7-fold), representational magnitudes were not significantly different from zero, either for young or for older adults.*

*Units are parameter estimates. Error bars indicate SEM. * denotes significant effects (p < 0.05).*

As discussed previously (Kunz et al., 2015; Stangl et al., 2017), reduced grid-cell-like representations in older adults could result (i) from a lack of temporal stability (i.e., stability of voxel-wise grid orientations over time), or (ii) from insufficient spatial stability (i.e., homogeneity of voxel-wise grid orientations across all entorhinal cortex voxels). To further specify which of these two factors was driving the result of reduced grid-cell-like representations, we calculated indicators of temporal and spatial representational stability for each participant and compared these between age groups. We found significantly reduced temporal stability of grid orientations in older adults (**Figure 25A**; t_{39} = 4.01, p <

0.001). This result was also confirmed by a separate analysis showing that changes in estimated voxel-wise grid orientations over time were significantly larger in older than in young adults (**Figure 25B**; t_{39} = -4.29, p < 0.001). On the contrary, spatial stability scores did not differ between age groups (**Figure 26A**; t_{39} = 0.91, p = 0.370). Given that, theoretically, the lack of a difference in spatial stability could result from spatial smoothing of the fMRI time series, we also calculated spatial stability scores for unsmoothed data, but again, we did not find a significant difference between age groups (**Figure 26B**; t_{39} = 0.53, p = 0.597).

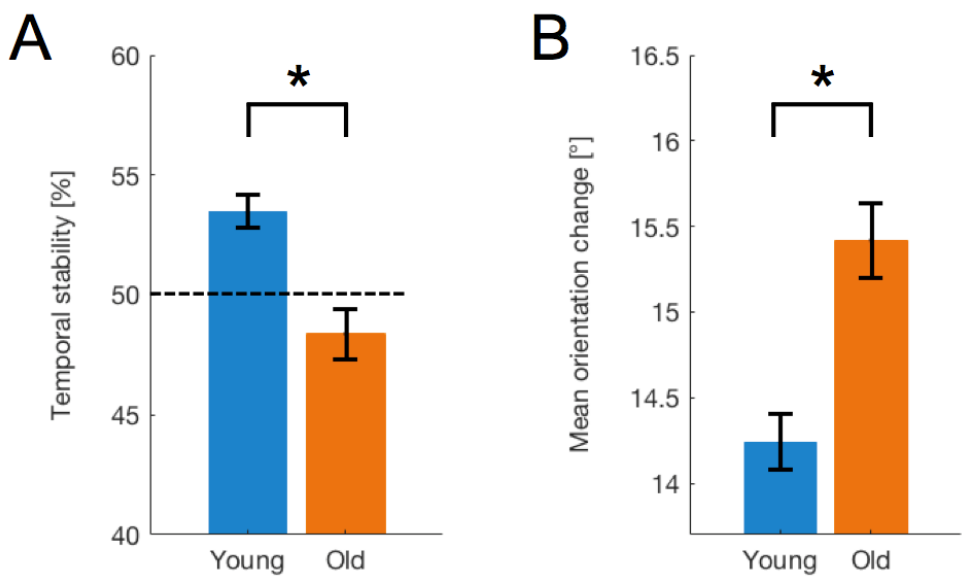

Figure 25: Temporal stability of grid-cell-like representations

A: *Lower temporal stability of grid-cell-like representations in older as compared to young adults. Dashed line indicates 50% chance level. Temporal stability scores were significantly different from chance level in young but not in older adults (young: t_{19} = 4.93, p < 0.001; old: t_{20} = -1.55, p = 0.136).* ***B:*** *Also the changes in estimated voxel-wise grid orientations over time were significantly larger in older relative to young adults.*

*Error bars indicate SEM. * denotes significant effects (p < 0.05).*

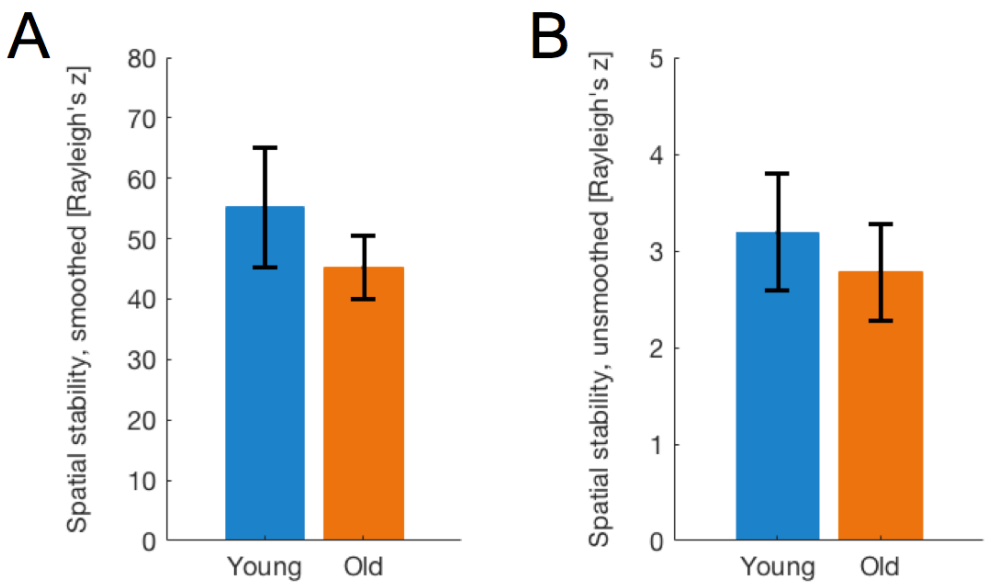

Figure 26: Spatial stability of grid-cell-like representations

A: *Spatial stability of grid-cell-like representations in entorhinal cortex voxels was not significantly different between young and older adults.* ***B:*** *Also for unsmoothed fMRI data, spatial stability scores were not significantly different between young and older adults.*

Error bars indicate SEM.

3.3.2 Control analyses

Cognitive aging is accompanied by many behavioral and neurophysiological changes that could serve as alternative explanations for our finding of reduced grid-cell-like representations in older adults. For example, we found that, relative to young adults, older adults spent more time per trial standing still (young: 1.8 ± 0.66 sec/trial, old: 4.91 ± 1.72 sec/trial; t_{39} = -7.55, $p < 0.001$) and rotating (young: 3.18 ± 0.87 sec/trial, old: 4.78 ± 1.19 sec/trial; t_{39} = -4.93, $p < 0.001$) in the virtual environment during the object-location memory task, presumably to determine their own and the target object's location by looking around. This in turn led to a lower total duration of translation phases in older adults (young: 1810 ± 123 sec, old: 1451 ± 200 sec; t_{39} = 6.88, $p < 0.001$). Consequently, the amount of translation data we acquired from older adults was on average 80.16 percent of the data from young adults. Given that translation phases were used

for the analysis of grid-cell-like representations, we checked whether the age difference in grid-cell-like representations might be driven by the different amounts of data between age groups. We re-ran the analysis of grid-cell-like representations for young adults, using only 80.16 percent of their translation data in order to match the data of older adults. Data reduction in young adults was implemented in two different ways, by shortening scanning runs and shortening translation durations, respectively (see Section 3.2.9). The results of these control analyses mirrored the original results using the full dataset (**Figure 27**): In both reduced datasets of young adults, we found a significant effect of grid-cell-like representations (shortened scanning runs: $t_{19} = 2.53$, $p = 0.021$; shortened translations: $t_{19} = 3.25$, $p = 0.004$) and the magnitude of grid-cell-like representations was not significantly different from the full dataset (shortened scanning runs: $t_{19} = -0.01$, $p = 0.992$; shortened translations: $t_{19} = 0.46$, $p = 0.653$), but remained significantly higher relative to older adults (shortened scanning runs: $t_{39} = -2.32$, $p = 0.026$; shortened translations: $t_{39} = -2.49$, $p = 0.017$). We therefore conclude that the difference in the amount of data did not drive the detected age difference in grid-cell-like representations, because this effect still persisted when modeling an identical amount of translation data for both age groups.

Second, the average error distance in the object-location memory task was slightly lower for young than for older adults (young: 10.3 ± 1.8 vm, old: 12.0 ± 2.6 vm; $t_{39} = -2.41$, $p = 0.021$). However, error distances and magnitudes of grid-cell-like representations were not correlated within either of the two groups (young: $r = -0.19$, $p = 0.417$; old: $r = -0.02$, $p = 0.934$), and an analysis of covariance confirmed that magnitudes of grid-cell-like representations were still significantly different between age groups when controlled for individual error distances ($F_{1,38} = 5.28$, $p = 0.027$). Therefore, it is unlikely that differences in task accuracy were driving the age difference in grid-cell-like representations.

Third, we did not find a difference between age groups in entorhinal cortex volume (see Section 3.2.9) that could potentially account for the observed difference in grid-cell-like representations (**Figure 28A**; $t_{39} = 1.38$, $p = 0.177$).

Also, there was no correlation between individual entorhinal cortex volume and grid-cell-like representation magnitude, either within young or older adults (young: r = -0.14, p = 0.554; old: r = 0.30, p = 0.186), and grid-cell-like representation magnitudes were significantly different between age groups in an analysis of covariance controlling for entorhinal cortex volume ($F_{1,38}$ = 6.01, p = 0.019).

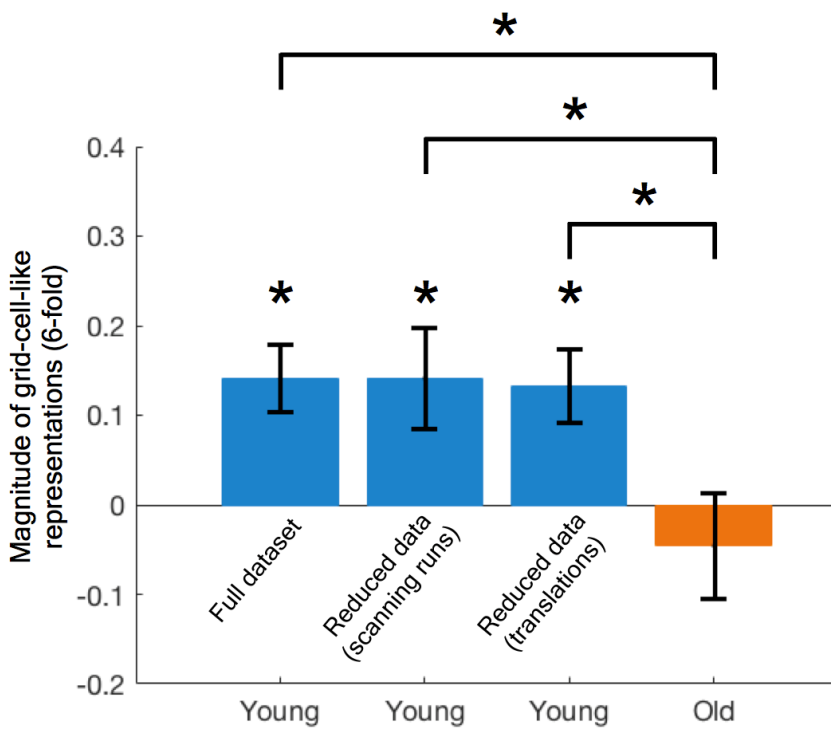

Figure 27: Grid-cell-like representations in young and old adults for full datasets versus models with reduced data

The magnitude of grid-cell-like representations was significantly reduced for older adults (orange bar "Old") as compared to young adults (blue bar "Young, Full dataset"). Re-analyzing the data from young adults with reduced data (i.e., mirroring the amount of translational data from old adults) confirmed this result, irrespective of whether the duration of scanning runs (blue bar "Young, reduced data - scanning runs") or whether the duration of individual translation events (blue bar "Young, reduced data - translations") was reduced.

*Units are parameter estimates. Error bars indicate SEM. * denotes significant effects (p < 0.05).*

Fourth, signal quality in the entorhinal cortex could not account for differences in grid-cell-like representations between young and older adults, as the tSNR (see

Section 3.2.9) did not significantly differ between age groups (**Figure 28B**; t_{39} = 1.63, p = 0.112), and magnitudes of grid-cell-like representations were not significantly correlated with tSNR within each group (young: r = 0.17, p = 0.484; old: r = 0.07, p = 0.776). Moreover, magnitudes of grid-cell-like representations remained significantly different between age groups in an analysis of covariance controlling for tSNR ($F_{1,38}$ = 5.71, p = 0.022).

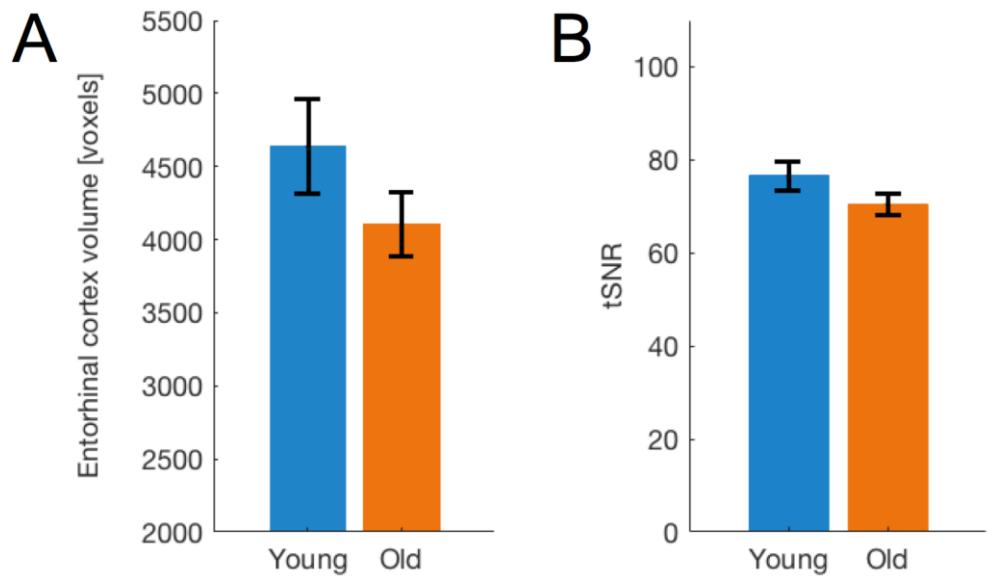

Figure 28: Entorhinal cortex volume and signal quality

A: *Volume size of the entorhinal cortex was not significantly different between young and older adults. Volume size was measured by the number of entorhinal cortex voxels in each participant's individual T2-weighted structural image.* ***B:*** *tSNR in the entorhinal cortex was not significantly different between young and older adults. tSNR was quantified by the mean signal within the entorhinal cortex divided by the standard deviation of this signal over time.*

Error bars indicate SEM.

Finally, we found that, compared to young adults, older adults made more linear and angular head movements during fMRI scanning (**Figure 29**; linear: t_{39} = -3.97, p < 0.001; angular: t_{39} = -3.26, p = 0.002; see Section 3.2.9 for more details). However, head movement is unlikely to account for group differences in grid-cell-like representations, as it did not correlate with grid-cell-like representation magnitudes within either of the two groups (young/linear: r = -0.16, p = 0.496; young/angular: r = -0.05, p = 0.842; old/linear: r = -0.05, p =

0.829; old/angular: r = -0.01, p = 0.976), and an analysis of covariance confirmed that magnitudes of grid-cell-like representations were still significantly different between age groups when controlled for both linear and angular head movement ($F_{1,38}$ = 6.91, p = 0.012).

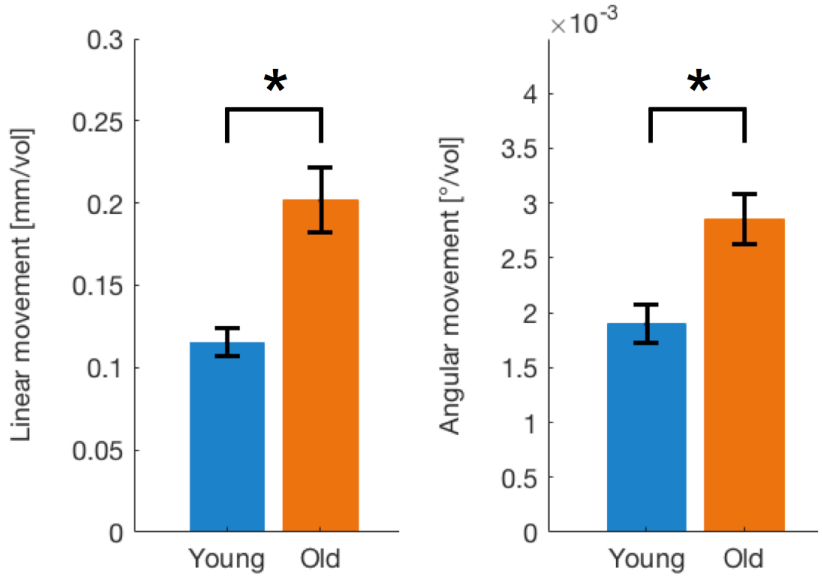

Figure 29: Head movement during fMRI scanning

Older adults showed more linear and angular head movement during fMRI scanning. Head movement was quantified by mean displacement per scan volume.

*Error bars indicate SEM. * denotes significant effects (p < 0.05).*

3.4 Discussion

In the present study, we found a significant magnitude of grid-cell-like representations in the entorhinal cortex of young adults. These grid-cell-like representations showed the typical 6-fold symmetric modulation of the BOLD signal that is expected from the putative firing pattern of grid cells, rather than other periodicities (i.e., 5-fold or 7-fold symmetric representations) that were tested in alternative control models. Moreover, we have demonstrated that grid-cell-like representations in the entorhinal cortex are compromised in old age.

Specifically, grid-cell-like representations were less stable over time in older as compared to young adults.

In further control analyses, we also tested whether the age-related difference in grid-cell-like representations could be driven by other confounding factors that might serve as alternative explanations for this finding. These control analyses, however, showed that our finding of reduced grid-cell-like representations in old age is unrelated to entorhinal cortex volume, fMRI signal quality in the entorhinal cortex, head movement during scanning, individual performance during the object-location memory task, as well as different amounts of translation data due to different task behavior between young and older adults. These results further underline the specificity of our finding of reduced grid-cell-like representations in old age, as it cannot be explained by these other general behavioral and neurophysiological changes that accompany the cognitive aging process.

Recently, grid-cell-like representations have also been investigated in young adults at increased genetic risk for Alzheimer's disease (Kunz et al., 2015). We note that this Alzheimer's risk group showed a remarkably similar pattern of data (i.e., both reduced magnitudes of grid-cell-like representations and reduced temporal stability) as compared to the older adults in the present study. Thus, the present data suggests that impaired grid cell function is not only related to pathological neurodegenerative processes, but also occurs during normal healthy aging.

While no previously reported study has investigated changes of the grid cell system in healthy old age, there is evidence that hippocampal place cells also show temporal instability of spatial representations in old rats (Barnes et al., 1997; Schimanski et al., 2013). Given the strong interconnections between the entorhinal cortex and the hippocampus (Amaral & Witter, 1995; Zhang et al., 2014), and previous findings showing coordinated temporal dynamics of entorhinal grid cells and hippocampal place cells (such as changes in grid orientation being linked to hippocampal remapping; Fyhn et al., 2007), reduced temporal stability in the firing of spatially tuned neurons may be a common neuronal mechanism underpinning age-related navigation deficits.

There is evidence that the medial entorhinal cortex receives input from the head direction system (Alonso & Klink, 1993; Amaral & Witter, 1995; Burgess et al., 2007) and it has been reported that the firing of grid cells is modulated by head direction (Sargolini et al., 2006). In theory, it is therefore possible that compromised grid-cell-like representations might be driven by impairments in head direction signals. To date, however, no single human or animal study has investigated age-related changes in the head direction system; therefore, this remains an important goal for future studies.

Numerous studies have reported that age-related changes in the navigation system primarily affect allocentric navigation, while egocentric computations are relatively preserved (for a review, see Colombo et al., 2017). As grid cells are largely thought to contribute (together with other spatially selective cell types) to an allocentric environmental representation in the hippocampal formation, the present finding of compromised grid-cell-like representations could provide a mechanistic explanation for age-related deficits in allocentric navigation. In the present study, however, we did not observe allocentric navigation deficits of older adults in the object-location memory task during fMRI scanning, which is not surprising, given that the task was designed to be simple, and participants were trained extensively to achieve accurate performance. Therefore, it remains a goal for future studies to investigate whether age-related changes in the grid cell system might impact on performance in other allocentric navigation tasks.

Based on recent findings, grid-cell-like representations are thought to play a central role not only in spatial navigation computations but also other higher-order cognitive processes, such as organizing conceptual knowledge (Constantinescu et al., 2016) or memory-guided viewing behavior (Julian et al., 2018; Nau et al., 2018). Therefore, our finding of compromised grid-cell-like representations in old age implies that deficient grid cell firing might be a key mechanism that could mediate also other cognitive deficits in old age, beyond pure spatial navigation. Not only does this provide important insights into age-related neurophysiological changes, but it also reveals the grid cell system as a

promising target for interventions and therapeutic approaches to counteract age-related cognitive decline.

3.5 Contributions and acknowledgements

Matthias Stangl (MS) carried out this project in a collaborative effort with Johannes Achtzehn (JA), Caroline Dietrich (CD), Claus Tempelmann (CT) and Thomas Wolbers (TW). MS and TW conceptualized the work. MS was responsible for project administration. MS and CT prepared the MRI sequences and scanning parameters. MS and JA programmed the virtual reality navigation tasks. MS and CD acquired the data. MS analyzed the data, visualized the results, and drafted the manuscript (Stangl et al., 2018). All authors edited the manuscript. TW supervised the work.

We express our gratitude to Viktoria Friesen, Mareen Hanelt, Svende Kübler and Denise Scheermann for their help with data acquisition, and to Jonathan Shine for valuable discussions about the data as well as proofreading the manuscript.

This work was supported by the Collaborative Research in Computational Neuroscience Grant (01GQ1303) of the German Ministry of Education and Research (BMBF) and by the European Research Council Starting Investigator Grant AGESPACE (335090).

4. PROJECT C

Compromised grid-cell-like representations as a mechanistic explanation for age-related path integration deficits

The output of this project has been previously published as an Open Access article (together with output from Project B) in the journal "*Current Biology*" (Stangl et al., 2018). While all results presented here stay unchanged to the original publication, some paragraphs, figures, and corresponding figure captions have been edited, in order to meet the structure, scope, and formatting standards of this thesis. Moreover, this thesis contains some additional figures and paragraphs that were not included in the original publication due to the journal's limitations regarding text length and number of display items.

4.1 Project introduction

After we have shown in Project B that human grid-cell-like representations are compromised in old age, Project C aimed to investigate whether grid-cell-like representations are linked to path integration performance and whether compromised grid-cell-like representations could potentially explain age-related path integration deficits.

Path integration is a vital function in spatial navigation that enables the continuous tracking of one's position in space by integrating self-motion cues. Several previous studies reported path integration deficits in old age. For example, older adults showed difficulties in path integration tasks both when path integration was performed on self-motion cues only (Allen et al., 2004; Mahmood et al., 2009; Adamo et al., 2012; Harris & Wolbers, 2012), and also when additional landmark information was available (Harris & Wolbers, 2012; Bates &

Wolbers, 2014). Moreover, age-related deficits have been demonstrated for path integration tasks that required the integration of body-based or vestibular cues (Allen et al., 2004; Adamo et al., 2012), or when only visual cues (i.e., optic flow information) could be used (Mahmood et al., 2009; Adamo et al., 2012; Harris & Wolbers, 2012). Together, these findings suggest a general path integration deficit in old age, across various conditions and independent of which sensory modality was tested. To date, however, little is known about the underlying neuronal mechanism of these deficits.

Theoretical work and computational models have long suggested a link between the grid cell system's function and path integration abilities (Fuhs & Touretzky, 2006; McNaughton et al., 2006; Burgess et al., 2007; Guanella et al., 2007; Hasselmo, 2008; Burak & Fiete, 2009; Giocomo et al., 2011; Zilli, 2012; Widloski & Fiete, 2014). Due to the regular hexagonal firing pattern of grid cells, which was also found to be modulated by heading direction and running speed, grid cells could, theoretically, integrate self-motion information about distance, orientation and movement speed. The grid cell system would therefore be ideally suited to perform the underlying neuronal computations needed for path integration. Moreover, studies in rodents with brain lesions have shown that the entorhinal cortex (i.e., the main location of grid cells) is a key region for path integration (Parron & Save, 2004; Van Cauter et al., 2013; Jacob et al., 2017) and several neuronal pathways have been described to convey self-motion information from sensory systems to the entorhinal cortex (Rochefort et al., 2013; Hitier et al., 2014; Jacob et al., 2014). While these findings further strengthen the idea that path integration computations are performed by the grid cell system in the entorhinal cortex, there is little empirical evidence for this hypothesis. Most recently, however, Gil et al. (2018) demonstrated that a disrupted grid cell firing pattern leads to impaired path integration performance in mice.

In addition, it has been shown that the entorhinal cortex is particularly vulnerable to neurodegenerative processes during normal aging as well as to pathological processes in early stages of Alzheimer's disease (as discussed in more detail in Section 1.2.2 of this thesis). Although the evidence is mixed, studies reported for

example a reduced number of neurons, a reduced volume, and accelerated cortical thinning of the entorhinal cortex in older adults (Gómez-Isla et al., 1996; Du et al., 2001; Pennanen et al., 2004; Fjell et al., 2014).

Together, the vulnerability of the entorhinal cortex to age-related neurodegeneration, in combination with its presumed importance for path integration computations, may indicate that impairments in entorhinal grid cells are a key mechanism to explain path integration deficits in old age.

To test this hypothesis, we re-invited the participants from Project B (in which we had already measured their grid-cell-like representations in an fMRI experiment) and assessed each participant's individual navigation performance in a novel behavioral path integration task. During this path integration task, participants had to keep track of their own position during movement along pre-defined curved paths by integrating self-motion cues. The task was implemented in two different modalities: The "body-based" modality provided only body-based self-motion cues during movement, whereas in the "visual" modality only visual cues could be used.

Combining fMRI data from Project B with each participant's individual path integration performance from Project C allowed us to investigate potential associations between grid-cell-like representations and path integration abilities. Moreover, we tested whether the path integration performance of participants could be predicted by their individual magnitudes of grid-cell-like representations, and compared the predictive value of grid-cell-like representations to a range of neuropsychological test scores as well as demographic variables.

Together, these analyses should reveal whether potential impairments in grid-cell-like representations could provide a mechanistic explanation for age-related path integration deficits.

4.2 Method

4.2.1 Participants

For this experiment, we re-invited the same participants that we had tested in Project B ("Grid-cell-like representations in old age"). The advantage of testing the same participants again was that they had already undergone fMRI testing and analysis of their grid-cell-like representations, and so we could directly investigate potential associations between their magnitudes of grid-cell-like representations and path integration abilities, without the need for further fMRI measurements.

Consequently, as in Project B, 41 healthy adults took part in this study. The group of young adults consisted of 20 participants (10 woman, 10 men) aged between 19 and 30 years (M = 24.5, SD = 3.3 years), whereas the group of older adults consisted of 21 participants (11 woman, 10 men) aged between 63 and 81 years (M = 69.3, SD = 4.8 years). Only participants with no reported history of neurological or psychiatric disease and no reported motor deficits during normal walking or standing took part in this study. All participants reported right-handedness and had normal or corrected-to-normal eyesight.

Participants also underwent neuropsychological assessment with a neuropsychological test battery. One participant from the group of older adults, however, did not complete the neuropsychological testing (see Section 4.2.4 for more details).

Informed consent was obtained from all participants in writing before the measurements, and the experiment received approval from the Ethics Committee of the University of Magdeburg.

Prior to the study, all participants underwent the Montreal Cognitive Assessment (MoCA) screening tool for mild cognitive impairment (Nasreddine et al., 2005). Participants who did not exceed a MoCA cut-off score of 23 (following Luis et al., 2009) were excluded from the study and did not participate in any further

measurements. Participants also completed an image-recognition task, which is not discussed further in this thesis.

4.2.2 Path integration task

In commonly used path integration tasks for humans, such as the triangle completion task (Fujita et al., 1993; Harris & Wolbers, 2012), participants traverse a path and only estimate the distance and direction to the starting location at the end of the path. In the current study, however, we used a task in which participants were asked at three different points along the path to estimate the distance and direction to the path's starting point (**Figure 30**). Multiple distance and direction judgments per path were used for two reasons: First, it results in a larger number of data points (i.e., participant responses) in a similar amount of time, enabling a more reliable estimation of path integration errors. Second, responses from multiple points along the path can allow for a more precise estimation of path integration errors. Specifically, when complex paths are used, a participant may become disorientated as they move along the path, and the chances of this occurring increase with the distance traversed. When only one response is collected at the end of the path, as per the traditional triangle completion task, the participant's estimate would be random and not provide a valid quantification of path integration performance. In contrast, our task samples from multiple points along the path meaning that, even if the participant has become disorientated at the path's end point, there are still other data points earlier in the path that provide more accurate estimates of path integration performance.

A central assumption of our path integration task is that observers track and use self-motion cues to continuously update their internal estimates of position and orientation. However, path integration performance can also rely on a "configural strategy", in which participants store the configuration of a path (i.e. segment lengths and turn angles) and only compute a homing response when required (Wiener et al., 2011). This strategy is often observed when the outbound path can be easily segmented into turns and distances – such as in the triangle

completion task – and it can induce systematic biases such as a tendency to regularize turns and distances to canonical values (e.g. isosceles triangles or right-angle turns; Sadalla & Montello, 1989). In order to eliminate these confounds, we therefore employed irregularly shaped paths, in which translations and rotations were combined into curved trajectories. In addition, we asked subjects to repeatedly report their internal estimates of the homing vector at intermediate stopping points. These strategies strongly encourage participants to continuously update their displacement estimates based on self-motion cues over the task.

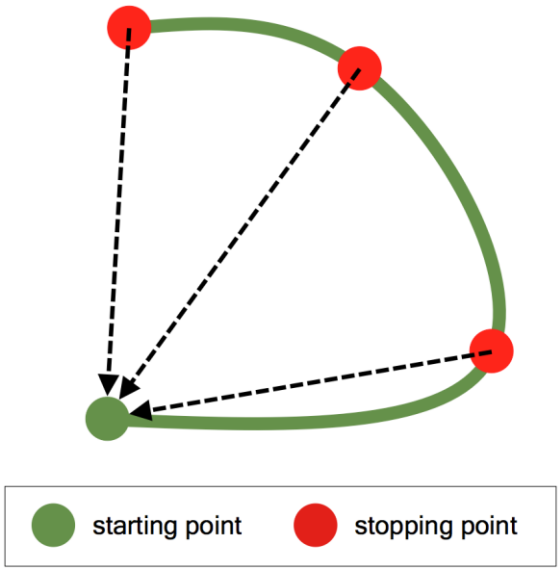

Figure 30: Behavioral path integration task

Example path from top-down perspective. Participants started at the path's starting point (green dot). There were three stopping points along each path (red dots). While walking along a path (curved green line), participants had to stop at each stopping point and estimate the direct distance and orientation to the path's starting point (black dashed arrows).

In this task, participants had to keep track of their own position during movement along pre-defined curved paths, while a head mounted display (HMD; Oculus Rift Development Kit 2, Oculus VR LLC, www.oculus.com) was positioned on the participant's head, so that they could not see anything outside the HMD. The task was implemented in two different modalities: In the "body-based" modality

(**Figure 31A**), no visual input was shown via the HMD (like in complete darkness), and participants could only use body-based self-motion cues, such as proprioceptive and vestibular representations, as well as motor efference copies that are produced during movement (Etienne & Jeffery, 2004). Participants held a wooden stick and were guided by the experimenter along a path. At each of three stopping points along the path, the distance to the starting point had to be estimated verbally in meters and centimeters, and participants turned their body on the spot to indicate the orientation to the starting point, which was measured by the built-in gyrometer of the HMD. In the "visual" modality (**Figure 31B**), participants sat stationary on a chair, while they saw a virtual environment via the HMD. This virtual environment did not contain any landmark cues but only showed a floor texture consisting of 500 white dots on a black ground plane. Each dot appeared at a random position within the field of view and disappeared after a random duration of 1 to 3 seconds, before it reappeared at a different location. Consequently, these so-called "limited lifetime dots" provided optic flow information, while their limited lifetime prevented the use of fixed reference points. Automated movement along a path was shown from first-person perspective, and on each of three stopping points along the path, participants estimated the distance to the path's starting point verbally in meters and centimeters, and indicated the presumed orientation by turning their view in the virtual environment to the left or right using a joystick.

Prior to the task, participants received written information about the task, and completed several practice paths in both modalities. During the task, participants wore earmuffs in order to prevent them from hearing any background sounds. Also, they were instructed to immediately inform the experimenter if they noticed any external cues that could help them to orient during the task (such as hearing, seeing, feeling or smelling something).

There were eight different pre-defined paths (**Figure 32**), and each path was performed two times per modality. The order of paths was pseudo-randomized, but the same order was used for all participants. Consequently, each participant completed 32 paths in total (16 paths per modality). Paths in different modalities

were intermixed, but there were always at least three different paths between two occurrences of the same path (irrespective of the modality).

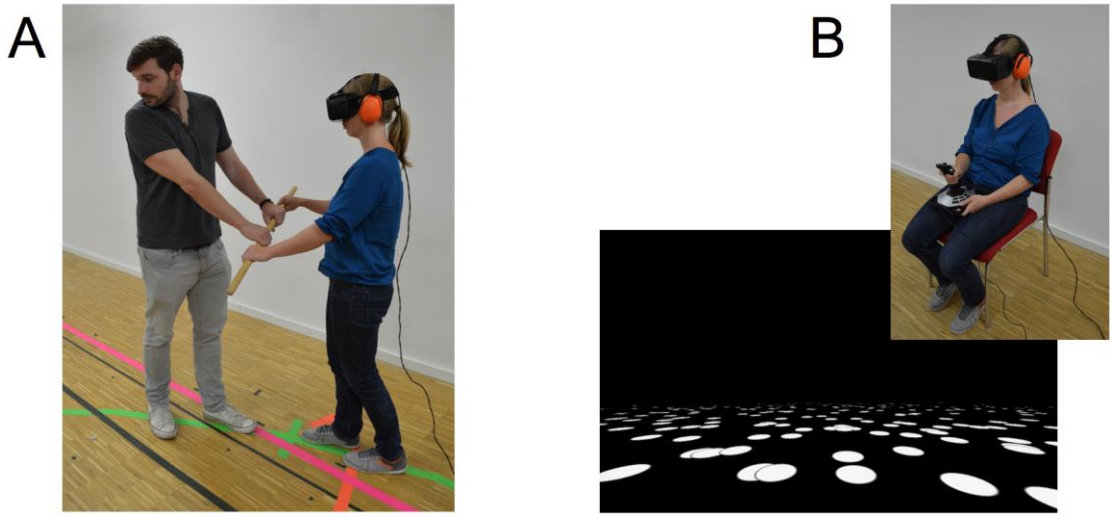

Figure 31: Body-based and visual modality of the path integration task

A: *In the "body-based" modality, the HMD showed no visual input, so that participants experienced only body-based cues during movement along the path. Participants held a wooden stick and were guided by the experimenter along the path. At each stopping point, the distance to the starting point had to be estimated verbally in meters and centimeters, and participants turned their body on the spot to indicate the orientation to the starting point.* ***B:*** *In the "visual" modality, participants sat stationary on a chair. The HMD showed a floor texture consisting of white "limited lifetime dots" on a black ground plane, which provided optic flow information while preventing use of fixed reference points. Automated movement along each path was shown from first-person perspective, and on each stopping point, participants estimated the distance to the path's starting point verbally in meters and centimeters, and indicated the presumed orientation by turning their view in the virtual environment to the left or right using a joystick.*

Coordinates for each of the eight pre-defined paths were defined as follows: First, a 3-legged path was created that comprised three distances and two turning angles between them (**Figure 33**). Each distance was either 2m, 3m, 4m, or 5m, and each angle was either 55°, 80°, or 105° to the left or to the right. Various combinations of distances and angles were used, that fit into a rectangular area of approximately 10 x 6 meters (given by the size of the room in which the experiment took place). On the basis of these 3-legged paths, we then created curved paths without corners by using the cscvn-function of MATLAB's curve fitting toolbox to calculate a natural interpolated cubic spline curve passing

through the turning points of the 3-legged path. Directions (left vs. right) of the two turning angles per path were counter-balanced between the different paths (**Figure 32**). The experimenters ensured that participants did not see the real physical dimensions of the room and the paths before and during the experiment.

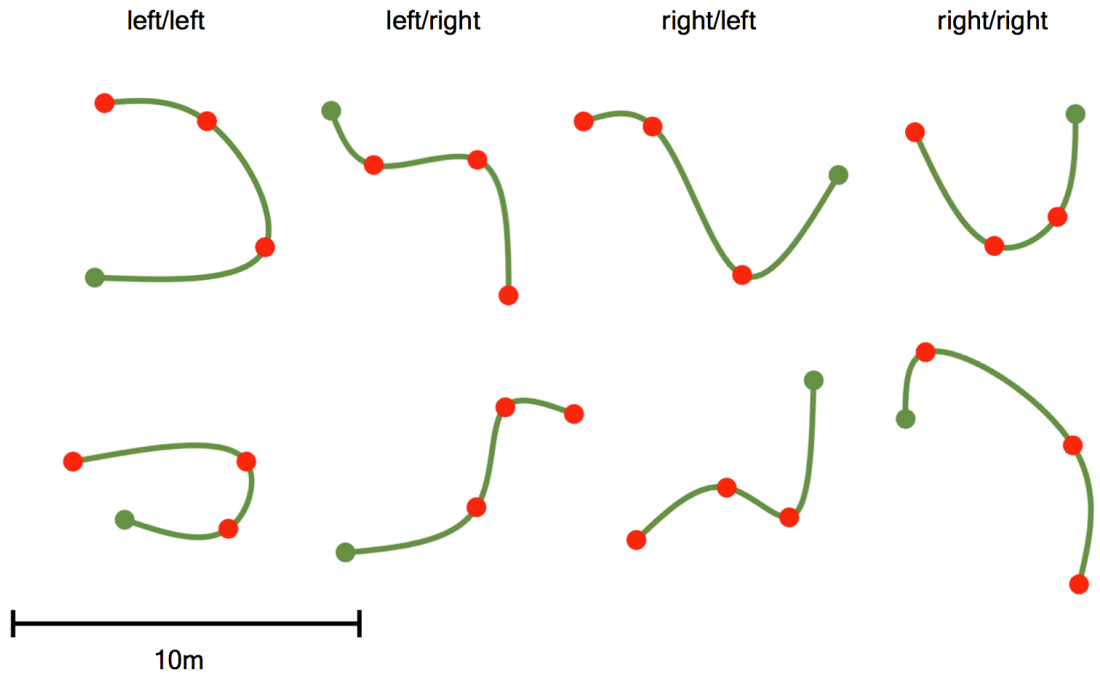

Figure 32: Layout of pre-defined paths from top-down perspective

Overview over the eight paths that were used in the experiment. Turning directions (left vs. right) of the two turning angles per path were counter-balanced between the different paths, leading to two paths with each of the following combinations: left/left (column 1), left/right (column 2), right/left (column 3), right/right (column 4). Green dots indicate starting points, red dots indicate stopping points along the path.

Participants completed the 32 paths in two blocks of 16 paths each. In the middle of each block, participants completed 4 so-called “standardization paths”, which were needed for data analysis in order to correct each participant’s distance estimate for their ability to use a correct estimate of a meter/centimeter when verbalizing their response (see Section 4.2.3). The procedure during a standardization path was similar as during a normal path, but a standardization path had only one starting point and one stopping point, which were connected

by a straight line, and participants had to estimate the distance between starting and stopping point. Two different distances (3m and 9m) had to be estimated both in body-based and visual modality, in the following order: 9m/visual, 3m/body-based, 9m/body-based, 3m/visual.

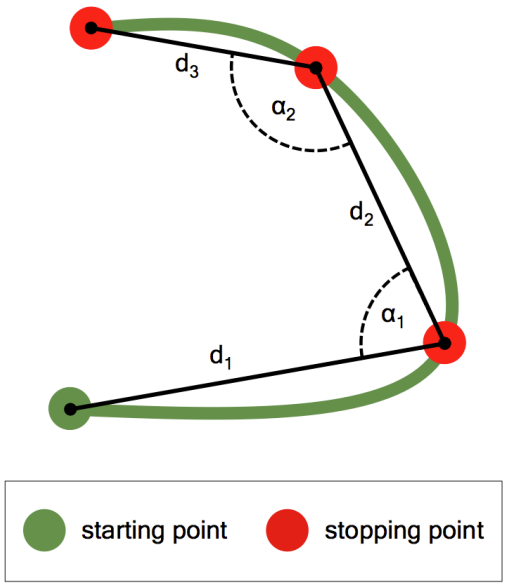

Figure 33: Definition of path coordinates

Each path was created by first defining a 3-legged path (black solid lines) consisting of three distances (d_1, d_2, d_3) and two turning angles between them (α_1, α_2). Participants walked along a curved version of this 3-legged path that had no corners and was created by a natural interpolated cubic spline curve passing through the path's turning points (green line).

After completing the task, participants filled out a form in which they were asked whether they noticed any external cues that could have helped them to orient during the task (such as hearing, seeing, feeling or smelling something), but no participant reported such confounding sources of information. Further, all participants were asked whether they had recognized that some paths were repetitions of each other, but no participant did.

The path integration task was developed using the Unity game engine 5.3.5 (Unity Technologies, www.unity3d.com).

4.2.3 Path integration data analysis

At every stopping point of a path, participants had to estimate the distance to the path's starting point verbally in meters and centimeters. However, due to these verbal estimates, the responded distance can be influenced not only by the participant's path integration performance, but might also be confounded by their ability to use a correct estimate of a meter/centimeter when verbalizing the response. For example, a participant with perfect path integration performance might still give suboptimal answers, just because they might have a relatively divergent perception of what they consider to be "a meter" (which might be unrelated to path integration performance per se). To get a "standardized" measure of path integration performance, we corrected each participant's responses for their individual ability to verbalize their distance estimate in meters/centimeters, and use their individual measure of what they perceive as a meter. Separately for each modality, we created an indicator of what each individual participant considered to be a meter by taking the responded distances from standardization paths (in which just a straight distance without any curves had to be estimated), and calculating:

$$f = d_{correct} / d_{response}$$

where $d_{correct}$ is the correct distance of the standardization path (either 3m or 9m), $d_{response}$ is the responded distance, and f is the resulting correction factor. Responded distances from standardization paths of the same distance (3m vs. 9m) and modality (body-based vs. visual) were averaged. For each participant, this led to two different correction factors per modality, one each for shorter distances (derived from the 3m standardization path) and longer distances (derived from the 9m standardization path). These factors were used to standardize the distance estimates this participant reported at normal paths: Whenever the participant's response distance of a normal path was between 0m and 6m, the response was multiplied with the correction factor for shorter distances, whereas response distances larger than 6m were multiplied with the correction factor for longer distances.

At each stopping point, the responded distance (multiplied with the individual participant's correction factor) and orientation was used to calculate the "presumed starting point". The x and y coordinates of the presumed starting point according to the participant's response were calculated by:

$$x_{presumedStart} = x_{stop} + d_{standardized} * \cos(ori_{response})$$

$$y_{presumedStart} = y_{stop} + d_{standardized} * \sin(ori_{response})$$

where $d_{standardized}$ is the standardized response distance, and $ori_{response}$ is the responded orientation. x_{stop} and y_{stop} are coordinates of the stopping point, $x_{presumedStart}$ and $y_{presumedStart}$ are the resulting coordinates of the presumed starting point.

One method to then determine the path integration error is, to calculate the Euclidean distance between the presumed starting point and the path's correct starting point. Throughout this thesis, we will refer to this measure of path integration error as "absolute path integration error" (**Figure 34A**). According to this method, each absolute path integration error reflects the error that occurred between the path's starting point and the respective stopping point (i.e., at stopping point 1 it reflects the error between the starting point and stopping point 1; at stopping point 2 it reflects the error between the starting point and stopping point 2; and so on). Accumulation of this error measure (i.e., absolute path integration errors) across all available stopping points, however, would lead to an overrepresentation of errors that occurred on early path segments (because these errors would be included for both earlier and later stopping points). In order to allow for accumulation of path integration errors across stopping points, we therefore also used an alternative method to calculate the path integration error, which we refer to as the "incremental path integration error" throughout this thesis: For a given stopping point, the Euclidean distance between the presumed starting point (according to the participant's response at this respective stopping point) and the previously presumed starting point (according to the response at the previous stopping point) was calculated (**Figure 34B**). Note that the previously presumed starting point at stopping point 1 is the correct starting point

of the path. Consequently, this measure of the path integration error reflects only the incremental error that occurred on the latest path segment before the stopping point, but does not include the error that occurred on earlier segments of the same path. More specifically, at stopping point 1 it reflects the error that occurred between the starting point and stopping point 1, at stopping point 2 it reflects the error that occurred between stopping point 1 and stopping point 2 (not including the error between the starting point and stopping point 1), and so on. This method of calculating the path integration error allows, for each individual participant, to aggregate all error measures from all available stopping points, because each incremental path integration error measure includes only the incremental (i.e., unique) error contribution of one path segment.

Throughout this project, the absolute path integration error was used whenever we report path integration errors separately for different stopping points (e.g., to show the increase of path integration error over the course of multiple stopping points, such as shown in **Figure 35**, left panel). The incremental path integration error, however, is used whenever errors are accumulated and averaged across all available stopping points (such as shown in **Figure 35**, right panel), in order to get a single-value estimate of each participant's path integration performance.

4.2.4 Neuropsychological tests

Neuropsychological test scores of older adults were taken from a database of the German Center for Neurodegenerative Diseases Magdeburg. These neuropsychological tests were carried out within 12 months before or after participants took part in the path integration and fMRI experiment. One older adult did not complete neuropsychological testing. For this participant, only the magnitude of grid-cell-like representations and demographic variables (age, sex), but not neuropsychological test scores were used in the multiple linear regression analysis. For the remaining 20 older adults, the following neuropsychological test scores were used: Self-reported spatial abilities, measured by the Santa Barbara Sense of Direction scale (SBSOD; Hegarty et al., 2002). Spatial working memory, measured by the Corsi block-tapping task

(Kessels et al., 2000). Spatial attention, measured by the subtest "visual scanning", and general working memory, measured by the subtest "working memory" of the Testbattery for Attentional Performance (TAP, Zimmermann P. & Fimm B., Psychologische Testsysteme, Herzogenrath, Germany). Processing speed, measured by the Digit Symbol Substitution Test (DSST) of the Wechsler Adult Intelligence Scale (WAIS-IV, Wechsler D., Pearson Assessment, San Antonio, TX, USA). Cognitive status, measured by the Montreal Cognitive Assessment (MoCA; Nasreddine et al., 2005).

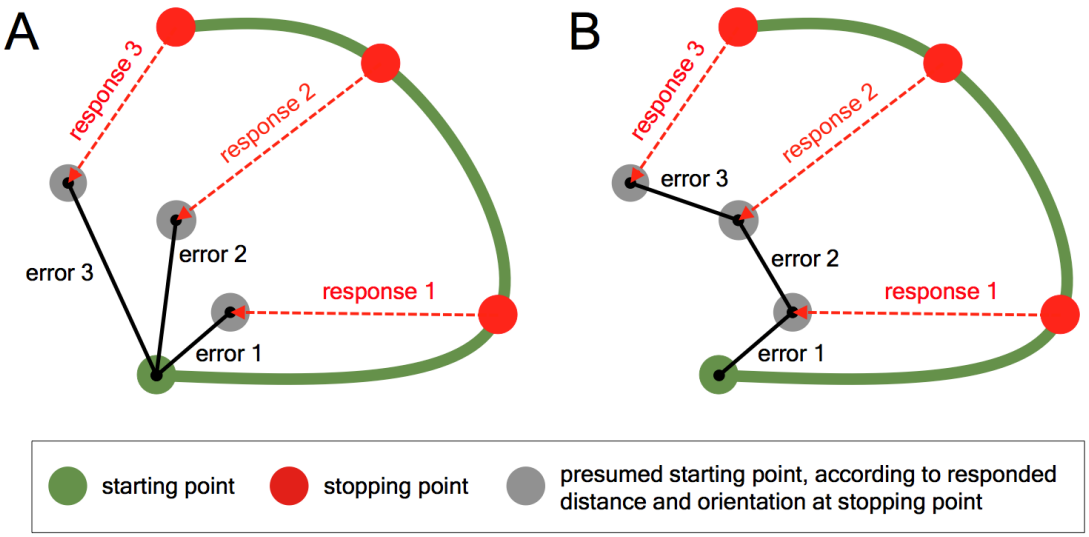

Figure 34: Calculation of path integration error

Path integration error was calculated for each stopping point separately (error 1, error 2, error 3). ***A:*** *For a given stopping point, the absolute path integration error was calculated by the Euclidean distance between the presumed starting point according to the participant's response at this respective stopping point (red dashed arrows), and the correct starting point of the path. This measure therefore reflects the path integration error that occurred between the path's starting point and the respective stopping point.* ***B:*** *For a given stopping point, the incremental path integration error was calculated by the Euclidean distance between the presumed starting point according to the participant's response at this respective stopping point (red dashed arrows), and the previously presumed starting point according to the response at the previous stopping point. Incremental path integration errors therefore reflect only the incremental error that occurred on the last path segment before the stopping point, but do not include errors that occurred on earlier segments of the same path. Consequently, this measure allows for accumulation of path integration errors from all stopping points across different paths, in order to get a single-value estimate of each participant's path integration performance.*

4.2.5 Quantification and statistical analysis

All statistical analyses were carried out using MATLAB 2016b and the Statistics and Machine Learning Toolbox for MATLAB 2016b. Correlation values, where given, are Pearson correlations. Error bars in figures indicate standard errors of the mean (SEM). Statistical analyses were performed using a significance threshold of $p < 0.05$.

Group comparisons between young and older adults were carried out using two-sample t-tests.

In order to divide the group of young adults into three subgroups with low, middle, and high magnitudes of grid-cell-like representations, a cluster analysis was applied on these magnitudes, using the k-means clustering function in MATLAB. Centroid starting locations (seeds) were defined by the mean magnitude of grid-cell-like representations for the 6 lowest, the 6 middle, and the 6 highest magnitudes of young adults, respectively.

4.3 Results

Relative to young adults, older adults showed a reduced path integration performance. In the body-based modality (**Figure 35**, top panel), the absolute path integration error was significantly higher for older adults already at the first stopping point ($t_{39} = 2.69$, $p = 0.010$), and performance was reduced also at stopping point 2 ($t_{39} = 3.40$, $p = 0.002$) and stopping point 3 ($t_{39} = 2.19$, $p = 0.035$) along the path. Consequently, the incremental path integration error (which allows for pooling path integration errors across stopping points) was also significantly higher for older relative to young adults ($t_{39} = -4.14$, $p < 0.001$). Similar results were obtained also for the visual modality of the path integration task (**Figure 35**, bottom panel). Again, older adults showed a significantly higher incremental path integration error than young adults ($t_{39} = -2.89$, $p = 0.006$). It is evident, however, that variability between participants was higher for the visual relative to the body-based modality, and absolute path integration errors of older

adults were significantly higher only at stopping point 1 (t_{39} = 2.24, p = 0.031) and stopping point 3 (t_{39} = 2.68, p = 0.011), but slightly failed the statistical significance level at stopping point 2 (t_{39} = 1.88, p = 0.068).

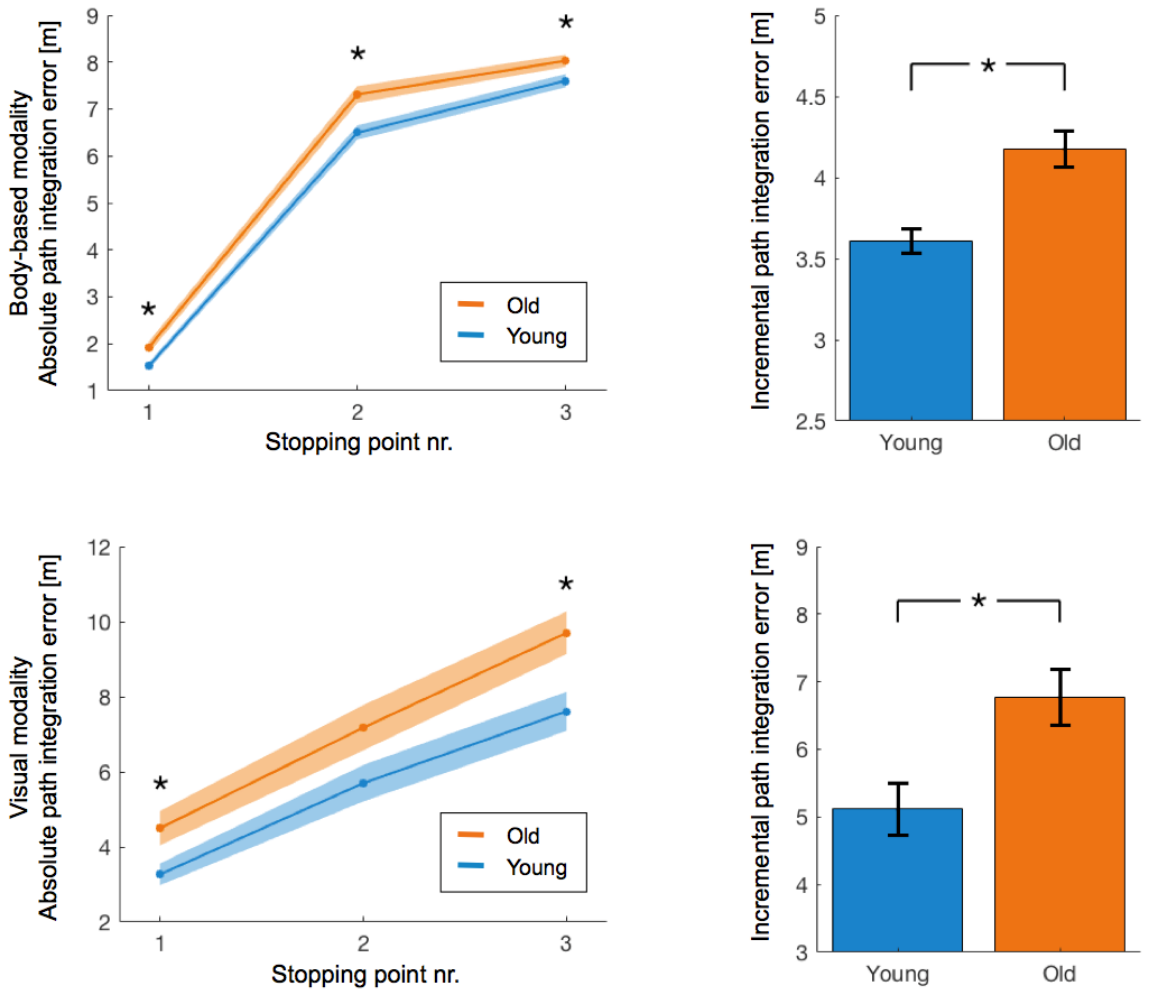

Figure 35: Path integration errors in young and older adults

Older adults showed significantly higher path integration errors than young adults, both in the body-based and the visual modality. ***Top panel:*** *In the body-based modality, older adults showed a higher absolute path integration error than young adults at all stopping points, and also incremental path integration errors (i.e., unique contributions to the path integration error for each stopping point) pooled across all stopping points were higher for older than young adults.* ***Bottom panel:*** *In the visual modality, older adults showed a higher incremental path integration error than young adults, and specifically, absolute path integration errors were higher for older as compared to young adults at stopping point 1 and stopping point 3.*

*Blue and orange lines indicate group mean ± SEM. Error bars indicate SEM. * denotes significant effects (p < 0.05).*

When combining data from both the fMRI measurements of Project B and the present path integration experiment, we found that, within the group of older adults, those participants with a higher magnitude of grid-cell-like representations showed lower path integration errors (**Figure 36**). This was indicated by a significant correlation between grid-cell-like representation magnitudes of older adults and their incremental path integration errors in the body-based modality ($r = -0.54$, $p = 0.011$). A similar pattern was found in older adults also for the visual modality, although this correlation did not reach statistical significance level ($r = -0.41$, $p = 0.065$). In young adults, there was no correlation between grid-cell-like representation magnitudes and incremental path integration errors, either in the body-based ($r = -0.10$, $p = 0.660$) or the visual modality ($r = -0.16$, $p = 0.511$).

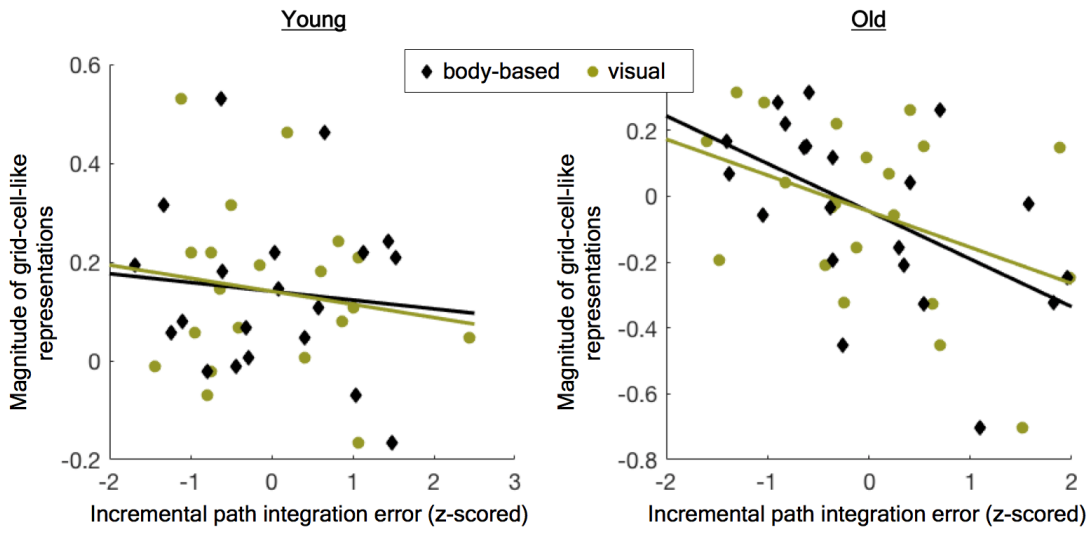

Figure 36: Association between magnitudes of grid-cell-like representations and path integration errors in young and older adults

In young adults (left), the magnitude of grid-cell-like representations was not associated with incremental path integration errors in either the body-based or the visual modality. In older adults (right), higher magnitudes of grid-cell-like representations were associated with lower incremental path integration errors. Path integration errors were z-scored for display purposes.

Moreover, we applied multiple linear regression on the data of older adults, in order to compare the predictive value of grid-cell-like representations to a range of other factors that might potentially explain variability in path integration

performance. In addition to grid-cell-like representations and individual demographic variables, this included a range of test scores from a neuropsychological test battery (see Section 4.2.4). Results of this regression analysis confirmed a significant link between grid-cell-like representations and both body-based as well as visual path integration performance, whereas no other demographic or neuropsychological factor could significantly predict path integration performance (Table 1).

Table 1: Multiple linear regression to predict path integration performance of older adults in body-based and visual modality

Predictor	β	t	p	sign.
Body-based modality:				
Grid-cell-like representations	0.069	2.717	0.022	p < 0.05
Age	-0.002	-1.137	0.282	ns.
Sex: male	0.023	1.784	0.105	ns.
Self-reported spatial abilities (SBSOD[a])	0.003	0.472	0.647	ns.
Spatial working memory (CORSI[b])	0.005	1.724	0.115	ns.
Spatial attention (TAP[c])	0.000	0.832	0.425	ns.
Working memory (TAP[d])	0.000	-0.550	0.595	ns.
Processing speed (DSST[e])	0.001	1.146	0.279	ns.
Cognitive status (MoCA[f])	0.004	1.431	0.183	ns.
Visual modality:				
Grid-cell-like representations	0.155	2.517	0.031	p < 0.05
Age	0.007	1.555	0.151	ns.
Sex: male	-0.023	-0.729	0.483	ns.
Self-reported spatial abilities (SBSOD[a])	0.006	0.425	0.680	ns.
Spatial working memory (CORSI[b])	0.012	1.559	0.150	ns.
Spatial attention (TAP[c])	0.000	0.521	0.613	ns.
Working memory (TAP[d])	0.000	-0.761	0.464	ns.
Processing speed (DSST[e])	0.000	0.116	0.910	ns.
Cognitive status (MoCA[f])	0.009	1.280	0.229	ns.

Path integration performance was calculated by 1 / incremental path integration error
"ns." denotes non-significant results
[a]*Santa Barbara Sense of Direction Scale*
[b]*Corsi block-tapping test*
[c]*Testbattery for Attentional Performance (TAP): subtest "visual scanning"*
[d]*Testbattery for Attentional Performance (TAP): subtest "working memory"*
[e]*Digit symbol substitution test (WAIS-IV)*
[f]*Montreal Cognitive Assessment (MoCA)*

Given the lack of an association between grid-cell-like representations and path integration performance in young adults, we wanted to carry out a more elaborate evaluation of this relationship and test whether an association can be found for a specific subgroup within the group of young adults. We therefore split up the group of young adults using cluster analysis to identify three subgroups of participants with low, middle, and high magnitudes of grid-cell-like representations (see Section 4.2.5). Within the group of young adults with low grid-cell-like representation magnitudes (n = 5), we found that their magnitudes of grid-cell-like representations were significantly correlated with incremental path integration errors in the body-based modality ($r = -0.89$, $p = 0.045$), whereas no correlation could be found for the group of young adults who had middle (n = 12; $r = 0.43$, $p = 0.159$) or high (n = 3; $r = 0.54$, $p = 0.634$) magnitudes of grid-cell-like representations. In the visual modality, the correlation values for the low group were also numerically stronger but failed to reach statistical significance (low: $r = -0.59$, $p = 0.298$; middle: $r = -0.22$, $p = 0.490$; high: $r = -0.28$, $p = 0.820$).

Next, we investigated whether those older adults who showed high path integration performance, also show “normal” grid-cell-like representations (i.e., whether their grid-cell-like representations appear to be similar to those of young adults). Given the significant association between magnitudes of grid-cell-like representations and body-based path integration performance, we split up the group of older adults based on their median incremental path integration error in the body-based modality, and further analyzed grid-cell-like representations in those older adults who showed low path integration errors (n = 10). In this subgroup, we found a significant magnitude of grid-cell-like representations ($t_9 = 3.55$, $p = 0.006$), whereas control models testing for other periodicities were not significantly different from zero (5-fold: $t_9 = -0.78$, $p = 0.454$; 7-fold: $t_9 = -0.48$, $p = 0.640$). Moreover, the average magnitude of grid-cell-like representations in this subgroup was not significantly different compared to young adults (**Figure 37**; $t_{28} = 0.06$, $p = 0.954$).

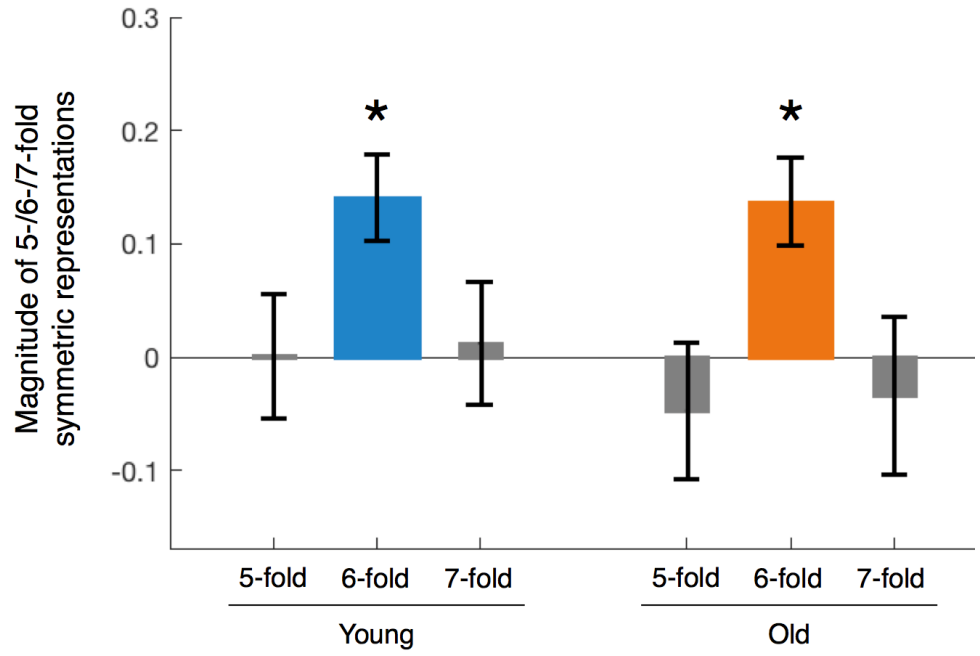

Figure 37: Magnitudes of 5-/6-/7-fold symmetric representations in young adults versus older adults with low path integration errors

Magnitudes of grid-cell-like (i.e., 6-fold symmetric) representations in a subgroup of older adults (n = 10; orange bar) who showed low incremental path integration errors appeared to be similar to grid-cell-like representation magnitudes of young adults (blue bar). Magnitudes of grid-cell-like representations were significantly different from zero for both young and older adults. Grey bars indicate control models testing for 5-fold and 7-fold symmetric representations.

*Units are parameter estimates. Error bars indicate SEM. * denotes significant effects ($p < 0.05$).*

4.4 Discussion

The results of this experiment demonstrate a modality-independent path integration deficit in old age. More specifically, older adults showed a deficit in computations of self-position, independent of whether path integration was based on body-based or visual self-motion cues. This is widely in line with results from previous studies that reported age-related path integration impairments for different sensory modalities (Mahmood et al., 2009; Adamo et al., 2012; Harris & Wolbers, 2012; Bates & Wolbers, 2014).

Combining the path integration data from the current project with data from Project B (i.e., fMRI measurements of grid-cell-like representations), we were able to reveal an association between grid-cell-like representation magnitudes and path integration abilities in older adults. This association was also confirmed by a multiple linear regression model, in which path integration performance in both body-based and visual modality could be predicted by individual magnitudes of grid-cell-like representations, whereas performance could not be significantly predicted by demographic variables and test scores of a neuropsychological test battery.

While animal studies and theoretical models have long suggested that path integration is a key function of the grid cell system, direct empirical evidence for this claim is scarce (Fuhs & Touretzky, 2006; McNaughton et al., 2006; Burgess et al., 2007; Guanella et al., 2007; Hasselmo, 2008; Burak & Fiete, 2009; Giocomo et al., 2011; Zilli, 2012; Widloski & Fiete, 2014; Gil et al., 2018). Our data show that the magnitude of grid-cell-like representations in the human entorhinal cortex is linked to path integration performance in old age and therefore further strengthens the hypothesis that grid cell function underlies path integration processes.

It is unclear, however, why we did not find an association between grid-cell-like representations and path integration performance in young adults. Potentially, this could be explained by additional processes, besides grid cell function, that may also contribute to path integration. For example, previous neuroimaging studies have demonstrated contributions of hippocampal and prefrontal computations (Wolbers et al., 2007; Sherrill et al., 2013; Chrastil et al., 2017). Variability in these processes could explain variations in path integration performance, when the grid cell system is intact and able to provide reliable positional computations (as assumed to be seen in young adults). In compromised grid cell systems (as more likely to be present in older adults), however, fundamental computations of positional information might be impaired, resulting in a direct relationship between the degree of impairment and path integration performance. To further test this assumption, we split up the group of

young adults into three subgroups of participants with low, middle, and high magnitudes of grid-cell-like representations, and found that correlations between magnitudes of grid-cell-like representations and path integration performance were higher for those participants with lower grid-cell-like representation magnitudes. While these results need to be treated with caution due to the small group sizes, they support the theoretical assumption that an association between grid-cell-like representations and path integration performance is only seen when grid-cell-like representations are compromised.

Lastly, we investigated grid-cell-like representations in a subgroup of older adults and found a significant magnitude of grid-cell-like representations for those older adults who showed high path integration performance. We therefore conclude that grid-cell-like representation magnitudes in older adults exhibiting high path integration performance, appear to be similar to those of the young adult group.

To sum up, we have demonstrated in this project that variation in magnitudes of grid-cell-like representations of older adults could explain individual differences in their path integration performance. On the one hand, this suggests that compromised grid-cell-like representations might serve as a mechanistic explanation for path integration deficits in old age, or potentially even for age-related spatial navigation deficits more generally. On the other hand, this finding further strengthens the hypothesis that computations of self-position during movement rely on entorhinal grid cell function, as has been suggested previously (Fuhs & Touretzky, 2006; McNaughton et al., 2006; Burgess et al., 2007; Guanella et al., 2007; Hasselmo, 2008; Burak & Fiete, 2009; Giocomo et al., 2011; Zilli, 2012; Widloski & Fiete, 2014). In addition, we have shown that the prognostic value of grid-cell-like representations for predicting path integration performance in older adults clearly exceeds the prognostic value of various standard neuropsychological tests and demographic variables. Together, these findings lay the foundation for future studies aiming to explore whether human grid-cell-like representations in the entorhinal cortex could potentially serve as a biomarker for integrity of the grid cell system and entorhinal cortex function. Since both neurophysiological changes in the entorhinal cortex (Braak & Braak,

1991; Gómez-Isla et al., 1996; Du et al., 2001; Pennanen et al., 2004; Masdeu et al., 2005; Stranahan & Mattson, 2010; Khan et al., 2014) and behavioral changes in navigational functions (Hort et al., 2007; Laczó et al., 2010; Mokrisova et al., 2016) are amongst the earliest symptoms of neurodegenerative processes like Alzheimer's disease, such a prognostic measure could also facilitate early detection of dementia and other neurodegenerative disorders. Furthermore, as grid cells have been discussed to not only provide the neuronal basis for navigational functions but also dimensional coding in non-spatial domains (Constantinescu et al., 2016; Aronov et al., 2017), future investigations will show whether changes in the grid cell system might explain not only path integration or spatial navigation deficits but also age-related decline in other cognitive domains.

4.5 Contributions and acknowledgements

Matthias Stangl (MS) carried out this project in a collaborative effort with Johannes Achtzehn (JA), Karin Huber (KH) and Thomas Wolbers (TW). MS and TW conceptualized the work. MS was responsible for project administration. MS and JA programmed the path integration task. MS and KH acquired the data. MS analyzed the data, visualized the results, and drafted the manuscript (Stangl et al., 2018). All authors edited the manuscript. TW supervised the work.

We express our gratitude to Viktoria Friesen, Mareen Hanelt, Svende Kübler, and Claudia Marx for their help with data acquisition, to Asema Hassan, Martin Riemer, and Sebastian Weiss for technical assistance, and to Jonathan Shine for valuable discussions about the data as well as proofreading the manuscript.

This work was supported by the Collaborative Research in Computational Neuroscience Grant (01GQ1303) of the German Ministry of Education and Research (BMBF) and by the European Research Council Starting Investigator Grant AGESPACE (335090).

5. PROJECT D

Sources of path integration error in young and older adults

This project was carried out in collaboration with Ila Fiete and Ingmar Kanitscheider from the Department of Neuroscience, Center of Learning and Memory, University of Texas at Austin. While I, Matthias Stangl, was responsible for the experimental and empirical parts of the project, Ila Fiete and Ingmar Kanitscheider developed the computational model that was used to decompose path integration errors into components.

5.1 Project introduction

The results of Project C in this thesis demonstrated that compromised grid-cell-like representations might be a key mechanism to explain path integration deficits in old age. Theoretically, however, path integration computations might be corrupted also by other potential sources of error – such as memory decay (leak), noise, biases, and reporting errors. Project D therefore aimed to reveal the specific contributors to path integration error, and to characterize their individual impact on path integration performance in young and older adults.

Spatial navigation is a complex behavior that combines many computations, including the storage and recall of information, the integration of information from multiple sensory and non-sensory brain areas, planning, prediction, and decision making. A vital component of navigation-related computations is path integration – the integration over time of a self-motion estimate, in the strict sense of vector calculus, to maintain an updated estimate of one's position and orientation while moving through space.

Self-motion estimates derive from a sophisticated pooling over multiple sensory modalities, and rely on proprioceptive and vestibular information, visual object and optic flow signals, as well as motor efference copies that are produced during movement (Etienne & Jeffery, 2004). After being processed in their respective low-level sensory systems, these cues are integrated in brainstem nuclei as well as cortical structures (i.e. area MST) to allow an overall estimation of angular and linear movement velocity (Bassett & Taube, 2001; Biazoli et al., 2006; Britten, 2008; Clark et al., 2012; Cullen, 2012; Butler & Taube, 2015). In this work, we seek to develop a method to decompose path integration errors into components (cf. Brunton et al., 2013) that can shed light on the mechanisms that could underlie the observed errors.

A circuit that functions as a path integrator for two-dimensional space must do the following: take as input the given two-dimensional velocity signal; remember the previous integrated state; increment the previous integrated state by adding to it a quantity proportional to the instantaneous velocity input. There are thus several natural sources of error: First, the velocity estimate might be wrong, with systematic bias or noise. Second, the integrator might remember its past states in a leaky way, so that there is a decay of information over time. Third, the velocity input-based increments might be summed with a scaling or gain prefactor that differs from the value required to match the instantaneous displacement. Fourth, the integrator might itself be noisy.

These errors accrue over the course of a spatial movement trajectory, and the net localization error at path's end will depend on the details of the trajectory. Thus, properly modeling and decomposing these errors requires iteration of a temporal dynamics, a statistical model that incorporates these dynamics, and sufficiently rich and varied spatial trajectories. One final error arises when a downstream neural circuit or the human experimenter attempt to obtain a readout of the output state of the integrator.

Our goal in the present work is not only to make progress in understanding the specific contributors to path integration error, but also to reveal sources of age-related degradation in navigation performance. Specifically, aging has

deleterious effects on path integration ability, with declines in the triangle completion task (Loomis et al., 1993) – a standard assay of path integration performance based on body-based, vestibular, or visual information cues (Allen et al., 2004; Mahmood et al., 2009; Adamo et al., 2012; Harris & Wolbers, 2012). Older adults are less accurate in reproducing travel distances or rotations (Mahmood et al., 2009; Adamo et al., 2012; Harris & Wolbers, 2012), and they exhibit worse path integration performance even if additional landmark information is available (Harris & Wolbers, 2012; Bates & Wolbers, 2014). Despite the sizeable body of research on losses in path integration performance with age, little is known about which specific aspects of the path integration computation or process are most affected in old age.

Here we combine an immersive virtual reality path integration experiment with a novel mathematical approach to reveal the sources of path integration error. We characterize the different contributors to error across subjects, and study group differences between young and older adults.

5.2 Method

5.2.1 Participants

56 healthy humans took part in this study. The group of young adults consisted of 30 participants (15 woman, 15 men) aged between 19 and 26 years (M = 22.0, SD = 2.0 years), whereas the group of older adults consisted of 26 participants (13 woman, 13 men) aged between 62 and 78 years (M = 69.0, SD = 4.6 years). Only participants with no reported history of neurological or psychiatric disease and no reported motor deficits during normal walking or standing took part in this study. All participants reported right-handedness and had normal or corrected-to-normal eyesight.

Informed consent was obtained from all participants in writing before the measurements, and the experiment received approval from the Ethics Committee of the University of Magdeburg.

Prior to the study, all participants underwent the Montreal Cognitive Assessment (MoCA) screening tool for mild cognitive impairment (Nasreddine et al., 2005). Participants who did not exceed a MoCA cut-off score of 23 (following Luis et al., 2009) were excluded from the study and did not participate in any further measurements.

5.2.2 Path integration task

Each participant's path integration performance was measured using a behavioral path integration task, in which they had to keep track of their own position during movement along pre-defined curved paths. In this task, participants were asked at four different points along the path to estimate the distance and direction to the path's starting point (**Figure 38**). The advantages of using multiple distance/direction judgments per path and employing irregularly shaped paths, in which translations and rotations were combined into curved trajectories, have been discussed earlier in this thesis (please see Section 4.2.2 for more details).

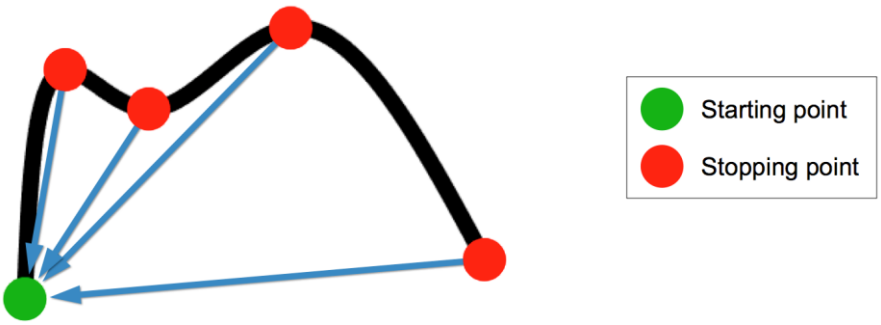

Figure 38: Behavioral path integration task

Example path from top-down perspective. Participants started at the path's starting point (green dot). There were four stopping points along each path (red dots). While walking along a path (curved black line), participants had to stop at each stopping point and estimate the direct distance and orientation to the path's starting point (blue arrows).

Prior to the task, participants received written information about the task, and completed several practice paths. An HMD (Oculus Rift Development Kit 2,

Oculus VR LLC, www.oculus.com) was positioned on the participant's head, so that they could not see anything outside the HMD. During the task, participants wore earmuffs in order to prevent them from hearing any background sounds. Also, they were instructed to immediately inform the experimenter if they noticed any external cues that could help them to orient during the task (such as hearing, seeing, feeling or smelling something).

During the task, participants held a wooden stick and were guided by the experimenter along a path (**Figure 39**). At each of four stopping points along the path, the distance to the starting point had to be estimated verbally in meters and centimeters, and participants turned their body on the spot to indicate the orientation to the starting point, which was measured by the built-in gyrometer of the HMD.

Figure 39: Path integration task procedure

Participants held a wooden stick and were guided by the experimenter along the path. At each stopping point, the distance to the starting point had to be estimated verbally in meters and centimeters, and participants turned their body on the spot to indicate the orientation to the starting point.

Via the HMD, participants saw a virtual environment, which consisted of a ground plane and distant landmark cues (**Figure 40**). The ground plane was designed to provide optic flow information during movement, but did not contain any fixed reference points or landmark cues. The distal landmarks were rendered at infinity, so that participants could use them only to determine their heading direction but not their position or any distance information. The exact position of a participant was tracked throughout the task using the Vicon Motion Tracking System with 12 cameras of type T10 (Vicon, Oxford, UK). The participant's viewpoint within the virtual environment was constantly updated depending on their actual position and movement, so that participants could actively walk around in the virtual environment. Consequently, in order to keep track of their own position relative to the path's starting point, participants could use both body-based and visual self-motion cues to perform the path integration task. Specifically, body-based self-motion cues included proprioceptive and vestibular representations, as well as motor efference copies that are produced during movement, whereas visual self-motion cues included optic flow information from the virtual environment (Etienne & Jeffery, 2004).

There were 10 different pre-defined paths (**Figure 41**). Coordinates for each path were defined as follows: First, a 4-legged path was created that comprised four distances and three turning angles between them. Each distance was either 2, 3.5, 5, or 6.5 meters, and each angle was either 55, 80, or 105 degrees to the left or to the right. Various combinations of distances and angles were used, that fit into a rectangular area of approximately 10 x 8 meters (given by the tracking area and size of the room in which the experiment took place). On the basis of these 4-legged paths, we then created curved paths without corners by using the cscvn-function of MATLAB's curve fitting toolbox to calculate a natural interpolated cubic spline curve passing through the turning points of the 4-legged path.

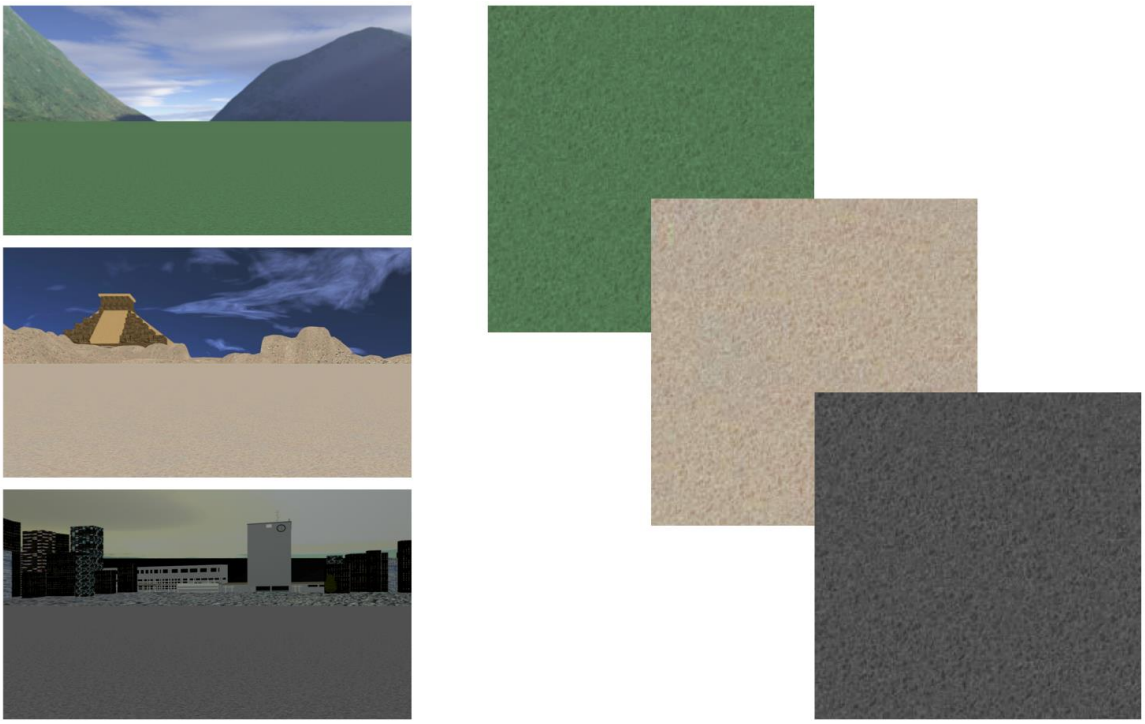

Figure 40: Virtual environments of the path integration task

Three different virtual environments were used in the path integration task. ***Left panel:*** *Each environment consisted of distant landmark cues that were rendered at infinity, so that participants could use them only to determine their heading direction but not their position or any distance information.* ***Right panel:*** *One tile of each environment's ground plane. These tiles had a so-called "seamless" texture, so that multiple tiles could be arranged next to one another, without any visible border or transition area between them. They were designed to not provide any landmark cues that could be used during the path integration task but only to provide optic-flow information during movement. The ground planes were identical between the three different environments, but differed only in terms of their color.*

Six paths comprised a mixture of left and right turns, respectively (see **Figure 41**, path numbers 1 to 6). Two additional paths (path numbers 7 and 9) only comprised right turns or left turns, respectively, and these two paths were present also in their mirrored version (i.e., the path that had only left turns was present also in its mirrored version comprising only right turns, and vice-versa). Directions (left vs. right) of the three turning angles per path were counter-balanced between the different paths.

The experimenters ensured that participants did not see the real physical dimensions of the room and the paths before and during the experiment.

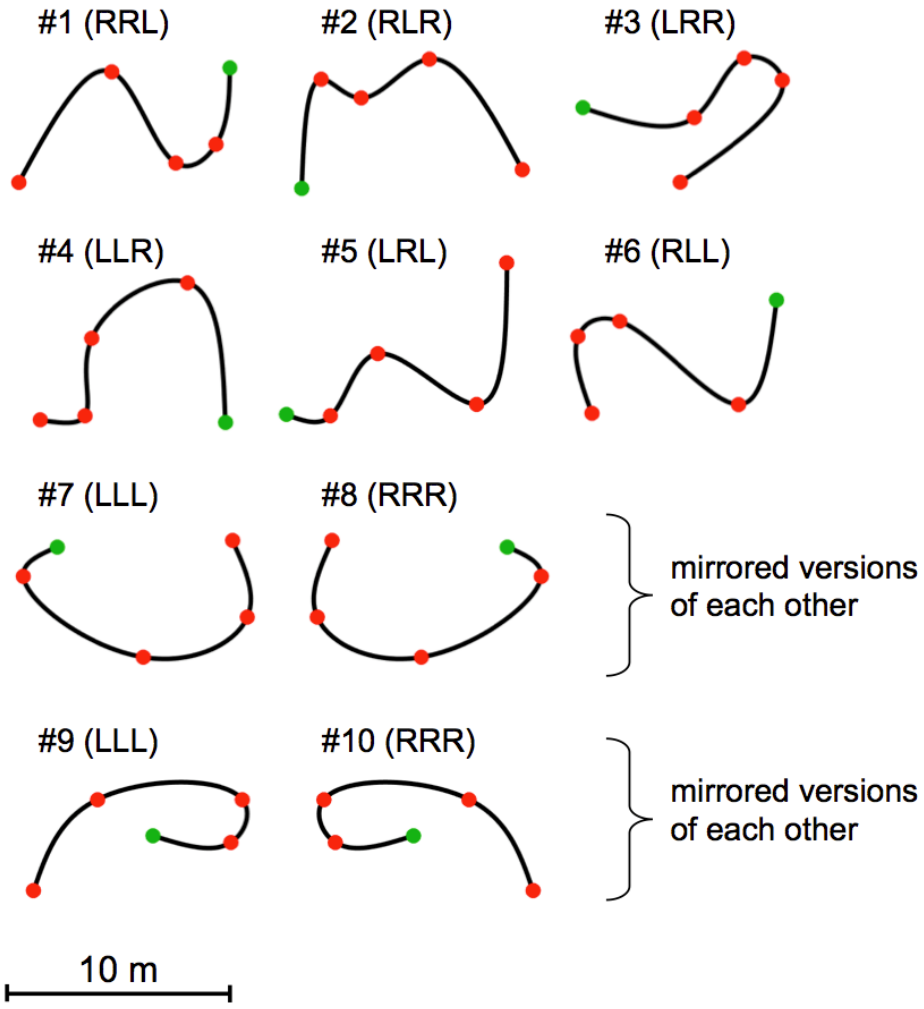

Figure 41: Layout of pre-defined paths from top-down perspective

Overview over the 10 different paths that were used in the experiment. Turning directions (i.e., left turns "L", vs. right turns "R") of the three turning angles per path were counter-balanced between the different paths. Six paths comprised a mixture of left and right turns (path numbers 1 to 6). Two additional paths (path numbers 7 and 9) comprised only right turns or left turns, respectively, and these two paths were present also in their mirrored version. Green dots indicate starting points, red dots indicate stopping points along the path.

Participants completed the path integration task in three blocks. Within each block, participants performed each of the 10 paths one time and, in addition, they performed the paths 1 to 6 (the ones which had both left and right turns) another time without stopping at the first three stopping points but only at the end of the path (i.e., only at stopping point 4). Consequently, each participant performed 16 paths per block. The order of paths was pseudo-randomized, but the same order

was used for all participants. There were always at least three different paths between two occurrences of the same path. The virtual environment was different in each block (see **Figure 40**) and the order of environments was randomized across participants.

After the 4th and after the 12th path of each block, participants completed three so-called “standardization paths”, which were needed for data analysis in order to correct each participant’s distance estimate for their ability to use a correct estimate of a meter/centimeter when verbalizing their response (see Section 5.2.3). The procedure during a standardization path was similar as during a normal path, but a standardization path had only one start point and one stopping point, which were connected by a straight line, and participants had to estimate the distance between starting and stopping point. Three different distances had to be estimated in the following order: 10 meters, 2 meters, 6 meters. Moreover, there were short breaks in the middle of each block and between blocks. **Figure 42** gives an overview over the procedure for each block.

After completing the task, participants filled out a form in which they were asked whether they noticed any external cues that could have helped them to orient during the task (such as hearing, seeing, feeling or smelling something), but no participant reported such confounding sources of information. Further, all participants were asked whether they had recognized that some paths were repetitions of each other, but no participant did.

The path integration task was developed using the WorldViz Vizard 5.1 Virtual Reality Software (WorldViz LLC, www.worldviz.com).

5.2.3 Path integration data analysis

The methods to calculate absolute and incremental path integration errors for behavioral data analysis were identical to the methods used in Project C (“Compromised grid-cell-like representations as a mechanistic explanation for age-related path integration deficits”). Therefore, please find a detailed description of these methods in Section 4.2.3 of this thesis.

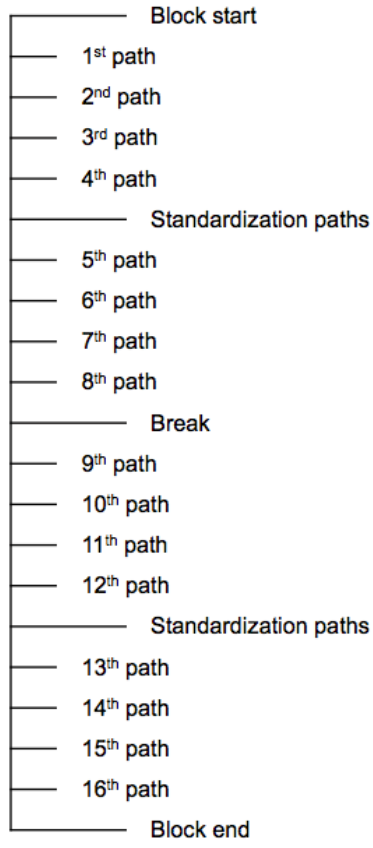

Figure 42: Experimental procedure per block

Each participant performed three blocks of the path integration task. Each block consisted of 16 paths. In addition, after the 4th and 12th path of each block, participants performed so-called "standardization-paths" (i.e., straight lines with a length of 2m, 6m, and 10m), which were needed for data analysis in order to correct each participant's distance estimate for their ability to use a correct estimate of a meter/centimeter when verbalizing their response. Moreover, there were short breaks in the middle of each block and between blocks.

In contrast to Project C, however, here our standardization paths had three different lengths (2m, 6m, and 10m). Consequently, three different correction factors, one each for shorter (derived from the 2m standardization path), middle (derived from the 6m standardization path) and longer distances (derived from the 10m standardization path), were used to standardize the distance estimates that a participant reported at normal paths: Whenever the participant's response distance of a normal path was between 0m and 4m, the response was multiplied with the correction factor for shorter distances, whereas response distances

between 4m and 8m were multiplied with the correction factor for middle distances, and response distances larger than 8m were multiplied with the correction factor for longer distances.

5.2.4 Computational modeling

Please note that the computational model described in this section was developed by Ila Fiete and Ingmar Kanitscheider from the Department of Neuroscience, Center of Learning and Memory, University of Texas at Austin.

At each stopping point, participants were asked to indicate the distance and orientation to the starting point of the path. The square error was calculated by first converting the distance estimate $\hat{\mathrm{d}}$ and the angular estimate $\hat{\varphi}$ to Cartesian coordinates and then comparing it to the true position of the stopping point relative to the starting point $\boldsymbol{r}_{true}$ (Note that throughout this section we use bold-faced letters to refer to two-dimensional vectors):

$$\mathrm{error}^2 = \left| \boldsymbol{r}_{true} - \begin{pmatrix} \hat{\mathrm{d}} cos\, \hat{\varphi} \\ \hat{\mathrm{d}} sin\, \hat{\varphi} \end{pmatrix} \right|^2$$

The path integration error is modeled to arise due to biases, leaks and noise in the path integration system. In the following, we distinguish between internal parameters, which affect the internal location estimate and are independent of the task, and external parameters, which affect the reporting of an internal location estimate and are task-dependent. Specifically, by predicting not only the size of the error, but also the actual estimates participants make at each stopping point, we aim to disentangle the following different sources of the path integration error:

Internal parameters:

- Memory decay (leak)
- Multiplicative velocity gain
- Additive bias
- Internal path integration noise

External parameters:

- Noise due to imperfect reporting of an internal location estimate

We assume that participants continuously update an internal, two-dimensional estimate of their location $\hat{\mathbf{x}}(t)$ using proprioceptive and visual percepts of their walking velocity $\mathbf{v}(t)$. The update process is corrupted by memory decay β, velocity gain α, additive bias **b,** and Gaussian noise with standard deviation σ_0 (where $\boldsymbol{\xi}(t)$ is normally-distributed Gaussian noise) according to

Eq. (1)

$$\frac{d\hat{\mathbf{x}}(t)}{dt} = -\beta\hat{\mathbf{x}}(t) + \alpha\mathbf{v}(t) + \mathbf{b} + \sigma_0\boldsymbol{\xi}(t)$$

The internal parameters can be interpreted as follows:

- Memory decay β: If $\beta > 0$, the current estimate $\hat{\mathbf{x}}(t)$ will not depend on values $\mathbf{v}(\mathbf{t} - \boldsymbol{\tau})$ with $\tau \gg 1/\beta$. This forgetting of velocity history is also called "leaky integration". Perfect integration corresponds to $\beta = 0$.
- Multiplicative velocity gain α: A value $\alpha > 1$ corresponds to overshooting of location updating given velocity $\mathbf{v}(t)$, a value $\alpha < 1$ corresponds to undershooting. Perfect integration corresponds to $\alpha = 1$.
- Additive bias **b:** Specifies the bias direction in which the location estimate gets drawn over time. Perfect integration corresponds to $\mathbf{b} = 0$.
- Internal path integration noise σ_0: Standard deviation of zero-mean Gaussian noise that corrupts path integration. Perfect integration corresponds to $\sigma_0 = 0$.

In addition to these internal noise and bias parameters, we assume that the estimates of distance and angle from the current location to the starting point that participants report are corrupted by additional reporting noise: The distance estimate requires a noisy conversion of an internal estimate to a verbal number (Izard & Dehaene, 2008) and the angular estimate that participants report by turning their body to face the path's starting point is corrupted by motor noise

(Schmidt et al., 1979; Jones et al., 2002; Faisal et al., 2008). Given distance d and angle φ between participants' internal location estimate and the true starting position, we assume that the reported distances $\hat{d}$ and angles $\hat{\varphi}$ are given by

Eq. (2)

$$\hat{d} = \exp(\log(d) + \sigma_d \eta_d)$$

$$\hat{\varphi} = \varphi + \sigma_\varphi \eta_\varphi$$

where σ_d and σ_φ are standard deviations of distance and angular noise, η_d is normally-distributed distance noise, and η_φ is normally-distributed angular noise. The parameterization of the distance noise is chosen such that for fixed σ_d, the magnitude of the reporting error $|\hat{d} - d|$ increases approximately linearly with d, in line with Weber's law (Oberlin, 1936; Gaydos, 1958; Cornsweet & Teller, 1965; Fechner, 1966; Indow & Stevens, 1966; Izard & Dehaene, 2008). We also find empirically that this Weber's law-type parameterization of the distance reporting error captures the data better than a linear parameterization (see Section 5.3).

Please see Appendix 2 for more details about the computational model used in this project, including model fitting, Extended Kalman Filter (EKF), and model comparison using the Bayesian Information Criterion (BIC).

5.2.5 Quantification and statistical analysis

While analyses related to the computational model were carried out by Ingmar Kanitscheider, analyses of the behavioral path integration data were carried out by Matthias Stangl, using MATLAB 2016b and the Statistics and Machine Learning Toolbox for MATLAB 2016b. Correlation values, where given, are Pearson correlations. Error bars in figures indicate SEM. Statistical analyses were performed using a significance threshold of $p < 0.05$. Group comparisons between young and older adults were carried out using two-sample t-tests or, in the case of model parameters, one-sided permutation tests.

5.3 Results

Older adults showed a lower performance in the path integration task, as compared to young adults (**Figure 43**). Absolute path integration errors were significantly higher in older relative to young adults already at the first stopping point, and also at all subsequent stopping points along the path (stopping point #1: $t_{55} = 2.15$, $p = 0.036$; #2: $t_{55} = 2.80$, $p = 0.007$; #3: $t_{55} = 2.64$, $p = 0.011$; #4: $t_{55} = 2.24$, $p = 0.029$). Moreover, incremental path integration errors (pooled over all stopping points; see Section 5.2.3) were significantly higher for older relative to young adults ($t_{55} = 3.23$, $p = 0.002$).

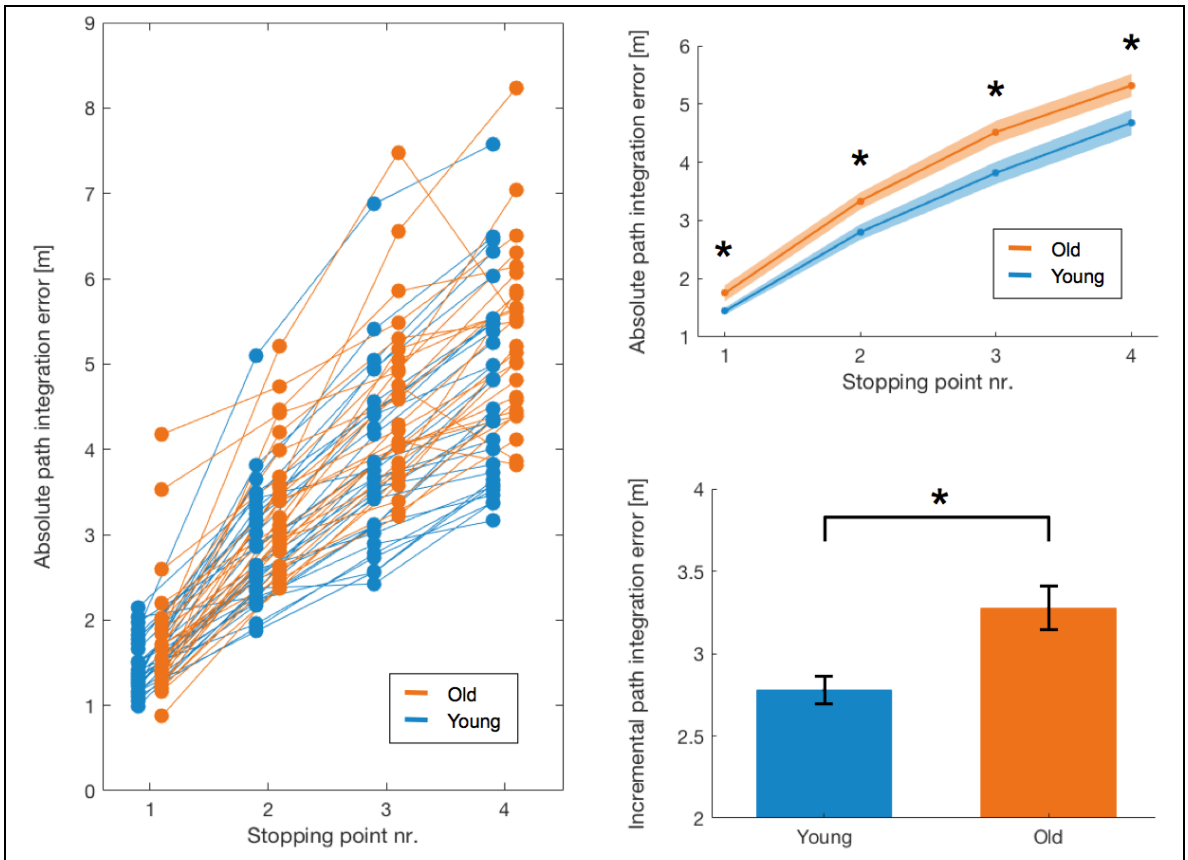

Figure 43: Path integration performance in young and older adults

Left panel: *Absolute path integration errors over four stopping points for young and older adults. Average errors per stopping point are shown for each participant separately by blue (young adults) and orange (older adults) dots, connected with lines between stopping points. It is evident that most participants showed an increase in their absolute path integration error with stopping points.* ***Right top panel:*** *On average, older adults showed higher absolute path integration errors than young adults at all stopping points. Blue and orange lines indicate group mean ± SEM.* ***Right bottom panel:*** *Incremental path integration errors were higher in older as compared to young adults.*

*Error bars indicate SEM. * denotes significant effects ($p < 0.05$).*

Next, we evaluated whether participants' performance in the path integration task was better than random guessing. Indeed, participants' estimates of their location were highly correlated with their true location (**Figure 44**) and shuffling their responses at each stopping point across trials led to a much higher square error (**Figure 45**).

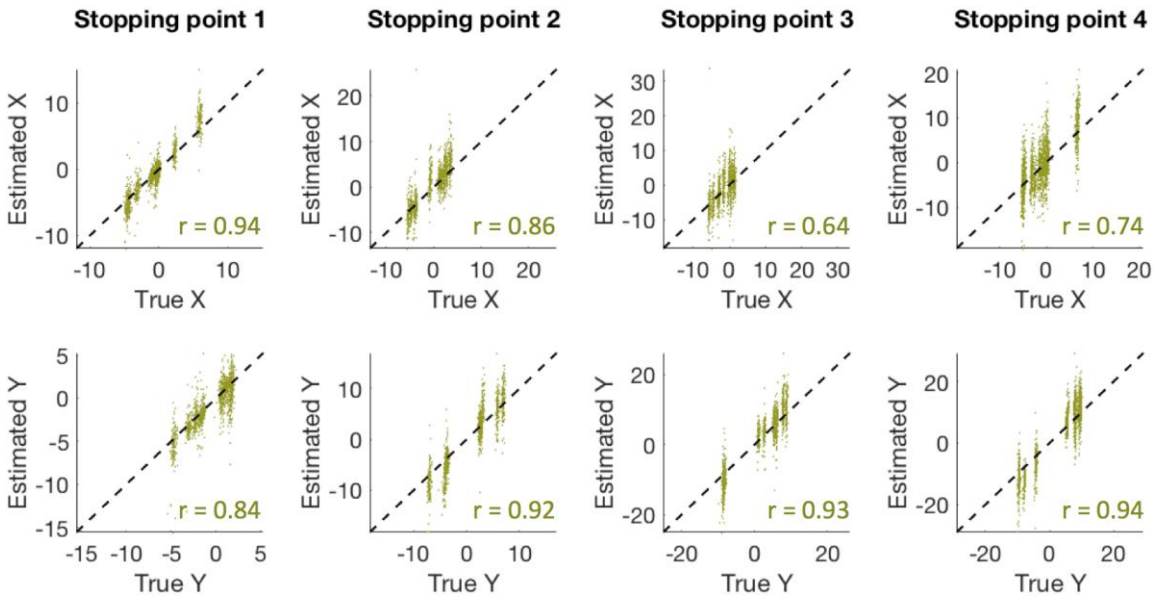

Figure 44: Participant's location estimates versus their true location

Each participant's location estimate (y-axis) versus their true location (x-axis) at each of the four stopping points (columns), separately for x-coordinates (top row) and y-coordinates (bottom row). The diagonal (dashed line) indicates perfect response (estimated location = true location). All correlation coefficients are significant (all $p < 0.00001$). All units are meters.

We then fitted a detailed computational model of participants' responses to disentangle different sources of path integration error. We modeled path integration as a continuous update of an internal location estimate using an instantaneous velocity estimate that is corrupted by the following internal error sources: leaky integration of location, under- or overestimation of velocity, an additive location bias, and zero-mean Gaussian noise. In addition, we assumed that the participant's reports of distance and angle from their internal location estimate to the origin are imperfect and corrupted by reporting noise. These

different error and bias parameters can be distinguished because they make different predictions depending on the shape of each individual trajectory.

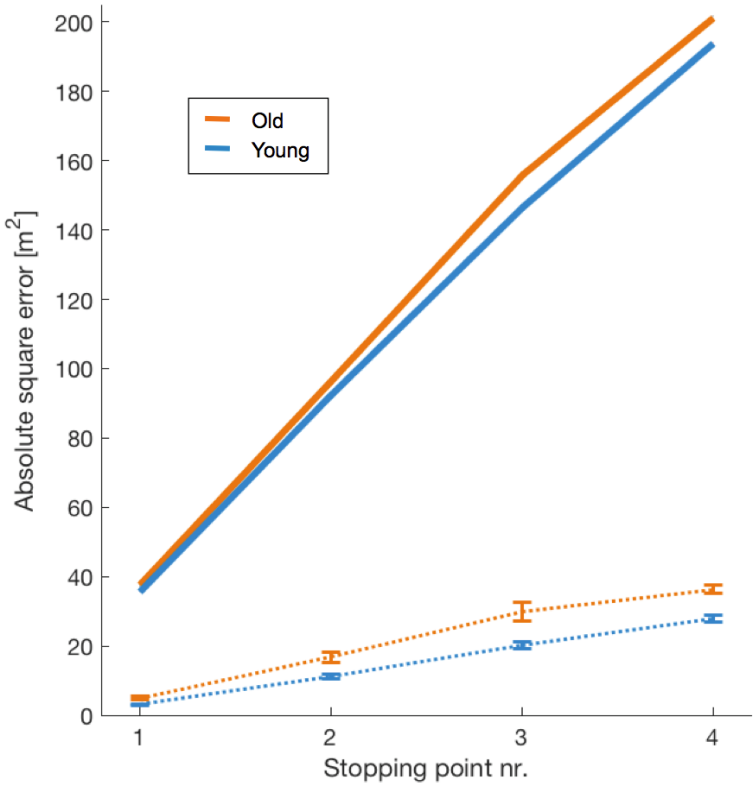

Figure 45: Path integration errors of young and older adults versus errors with shuffled responses

It is evident that the square error of participants' responses (dotted lines and error bars) is considerably lower than the square error obtained from shuffling their responses across trials, separately for each stopping point (solid lines). Error bars indicate group mean ± SEM.

After fitting the parameters individually per participant, we compared the prediction of the model with the data. The model correctly reproduced the characteristic increase in square error with stopping points (**Figure 46**) and was predictive of the direction of errors in individual trials, averaged over participants of the same age group (**Figure 47**).

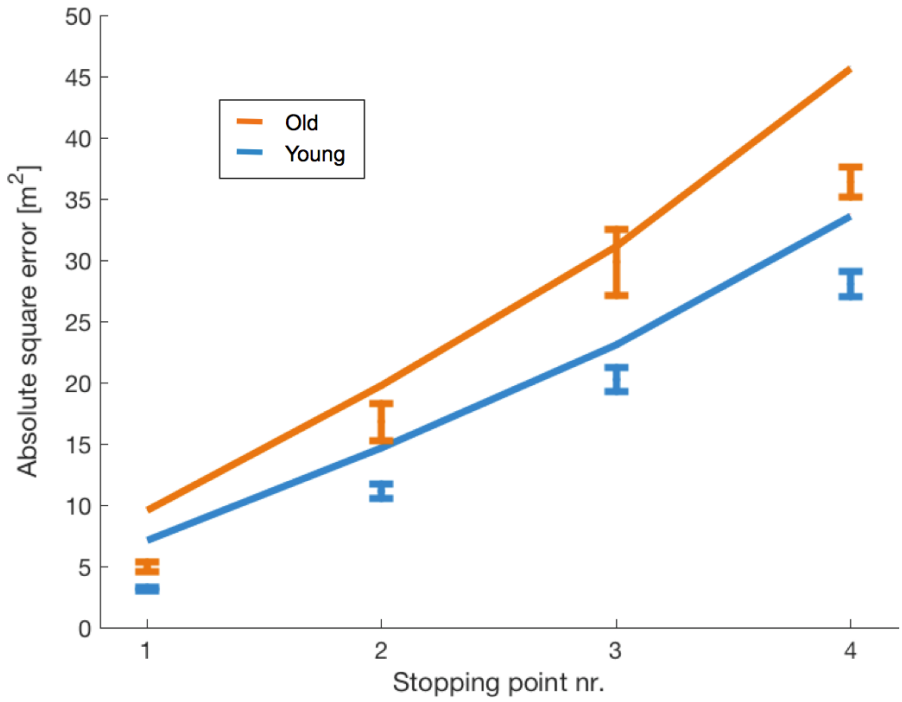

Figure 46: Path integration errors of young and older adults versus errors predicted by the model

Square error of participants' responses (single error bars) and square error of responses predicted by model (solid lines) over four stopping points. Error bars indicate group mean ± SEM.

We then provided support for the detailed structure of the computational model by comparing it to other model variants using BIC (see Appendix 2 for more details). We found that both the existence and structure of the reporting noise is important. The default model was much better supported by the data than a model variant without reporting noise or a model variant with reporting noise that does not scale with distance to the starting point (**Figure 48**; $\Delta BIC \gg 10$). Similarly, the default model with parameters fitted individually for each participant was much better supported by the data than fitting model parameters by age group (**Figure 49**; $\Delta BIC \gg 10$).

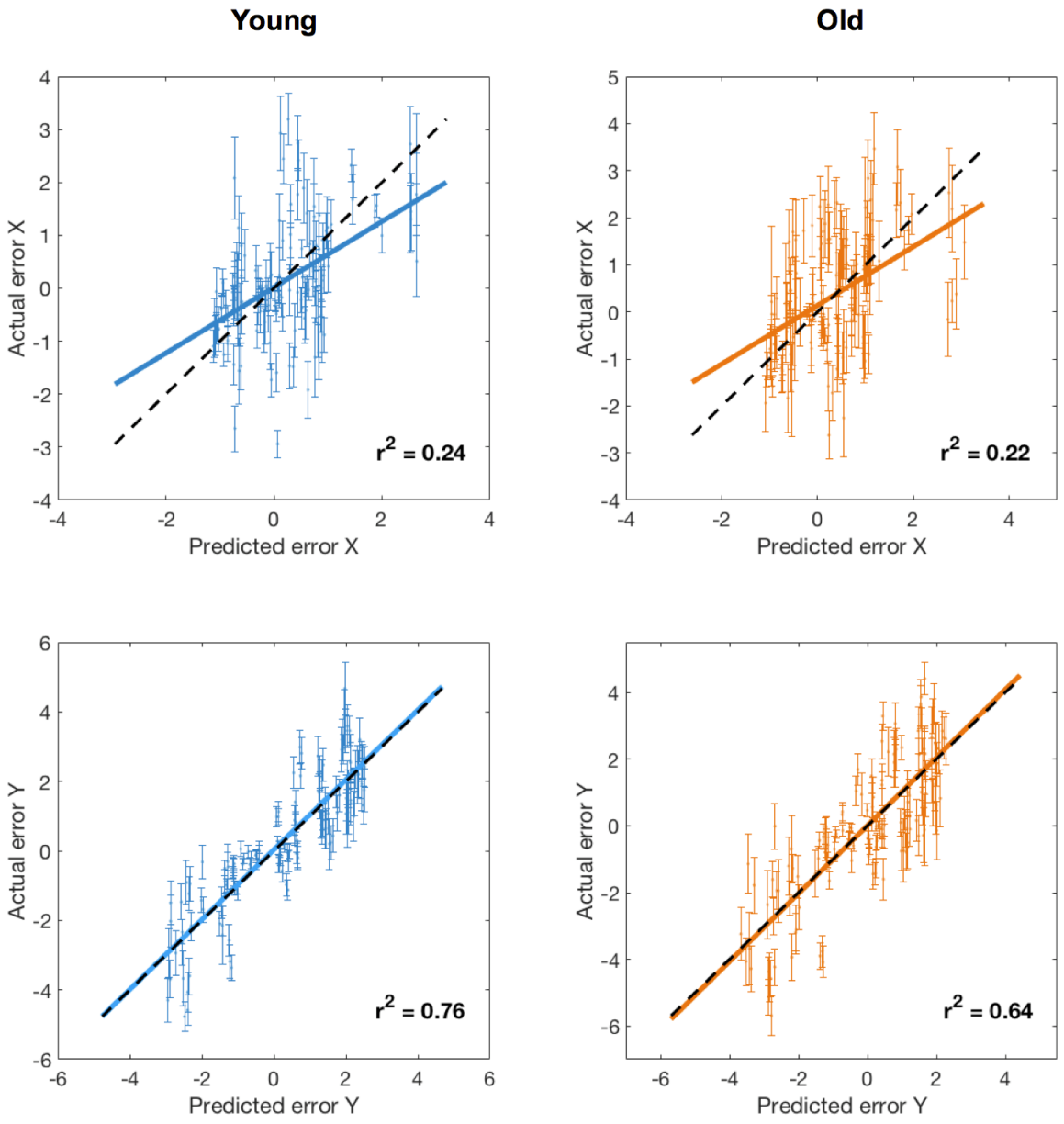

Figure 47: Single-trial path integration errors versus errors predicted by the model

Path integration error predicted by the computational model versus participants' actual error, separately for x-coordinates (top row) and y-coordinates (bottom row). The diagonal (dashed line) indicates perfect error prediction (predicted error = actual error). Error bars represent path integration errors for single trials (mean ± SEM), averaged over participants of the same age group (blue = young, orange = old). Solid lines represent the best-fitting linear regression fit. All units are meters.

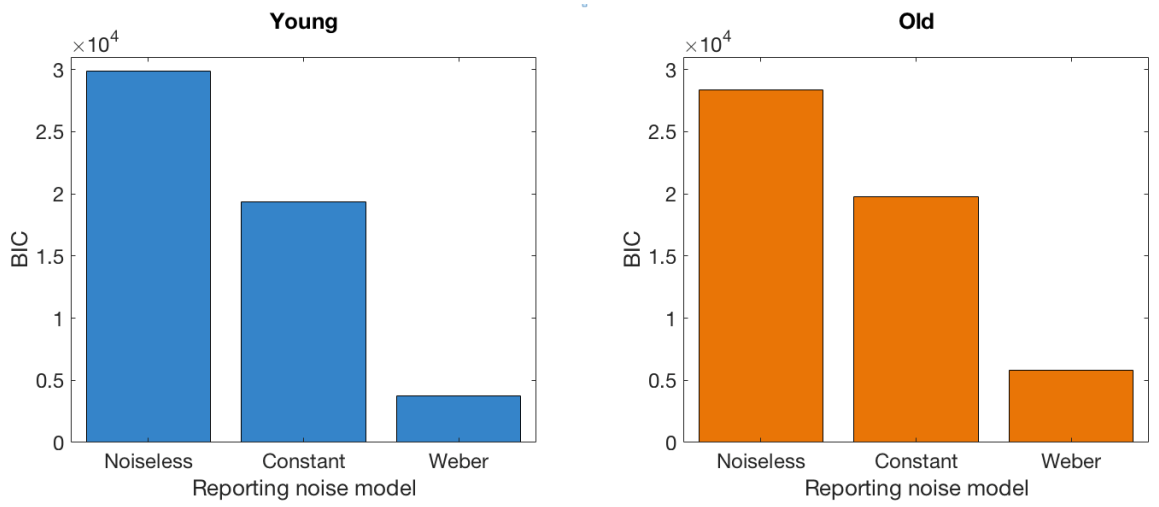

Figure 48: Comparison between models with different types of reporting noise

Model comparison using BIC between models with no reporting noise, constant reporting noise and Weber-like reporting noise. For both age groups, the model with Weber-like reporting noise was best supported by the data.

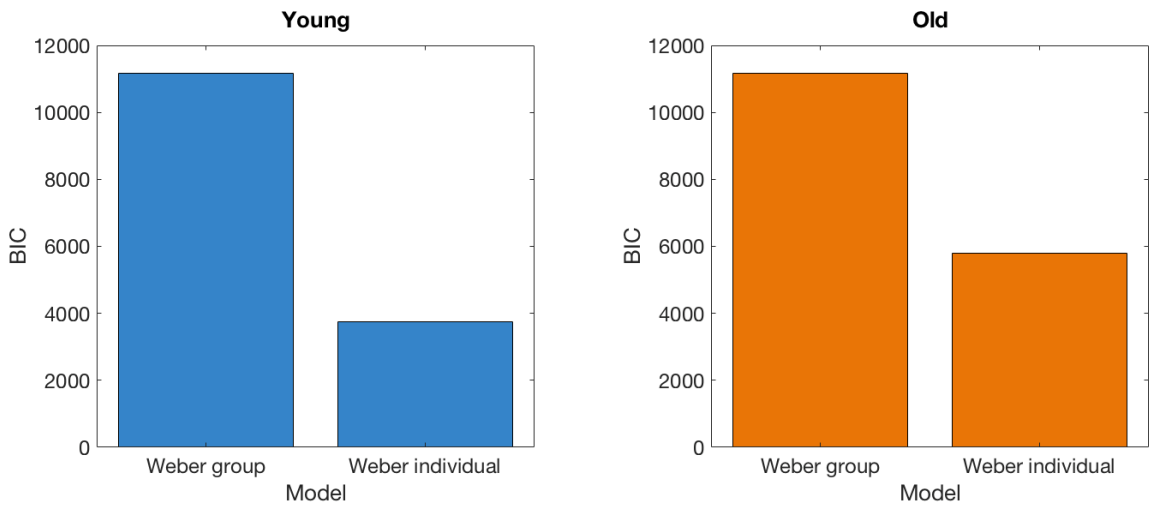

Figure 49: Comparison between group level and individual models

Model comparison using BIC between models that were fitted at the group level and models that were fitted individually for each participant. For both age groups, the model with individual parameters per participant was best supported by the data.

The computational model allowed us to assess which type of bias and noise parameter had the largest influence on the square error as predicted by the model. For this purpose, we calculated the relative influence of each parameter type on the predicted square error (see Appendix 2 for more details). We found that internal noise (50-55%) and velocity gain bias (25-26%) had the largest influence on the square error, followed by radial (14-15%) and angular (12-13%) reporting noise (**Figure 50**). The influences of both additive bias and memory leak were very small (< 3%).

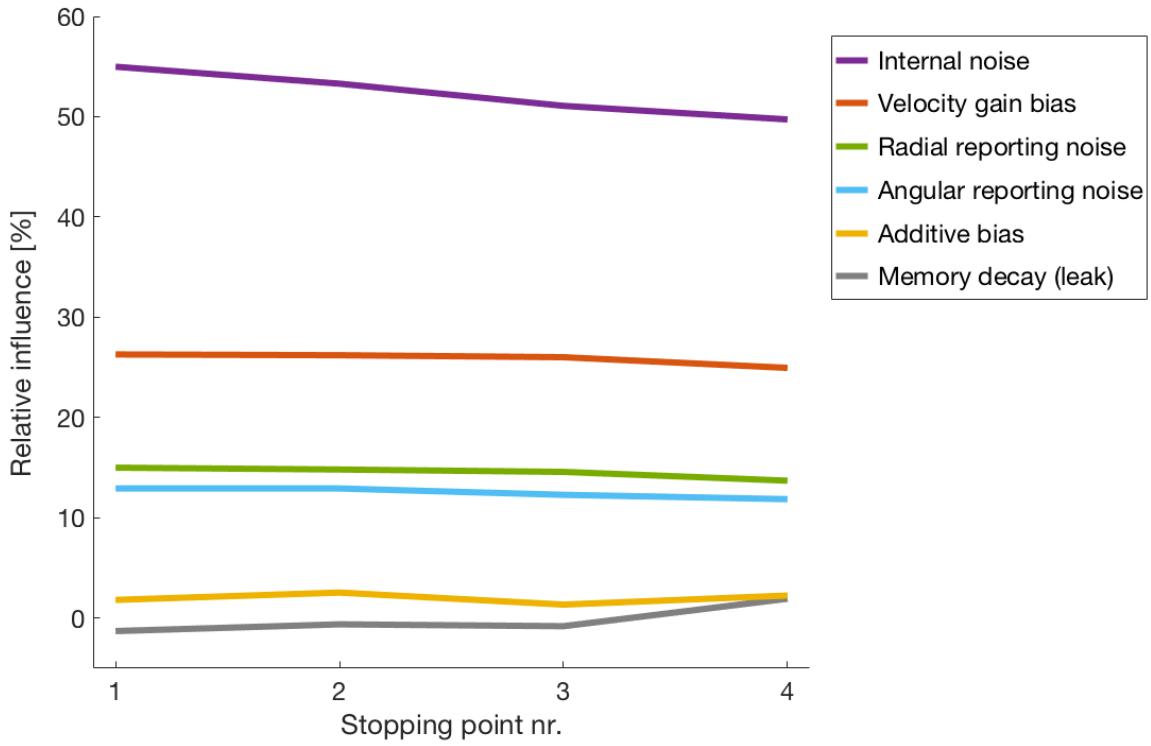

Figure 50: Impact of different error sources on path integration error

Relative influence of each model parameter on the predicted square error. Relative influence measures the predicted reduction in square error by setting a parameter to its ideal value corresponding to noiseless and unbiased integration. Note that due to the nonlinearity of the model the relative influences do not have to sum to 100%, and that a parameter's relative influence can be negative if the reduced square error is larger than the square error of the full model (see Appendix 2 for more details).

Finally, we compared the model parameter values between age groups. We found that older adults had a significantly larger additive bias (p = 0.001; one-sided permutation test), a significantly larger internal noise parameter (p = 0.018; one-sided permutation test), and a larger memory decay (p = 0.035; one-sided permutation test) than young adults (**Figure 51**). However, due to the small overall influence of the additive bias and memory decay, comparing each parameter's contribution to overall path integration error between age groups showed that only the internal noise (p = 0.012; one-sided permutation test) had a significantly higher contribution to error in older relative to young adults (**Figure 52**).

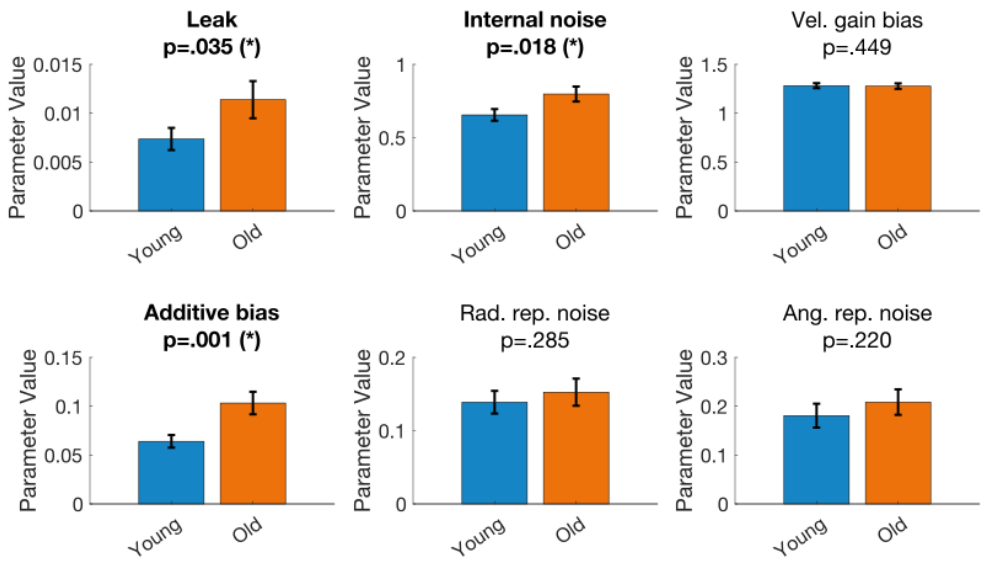

Figure 51: Comparison of model parameters between age groups

*Model parameter values, averaged over participants of the same age group, compared between young and older adults. * denotes significant effects in a one-sided permutation test (p < 0.05).*

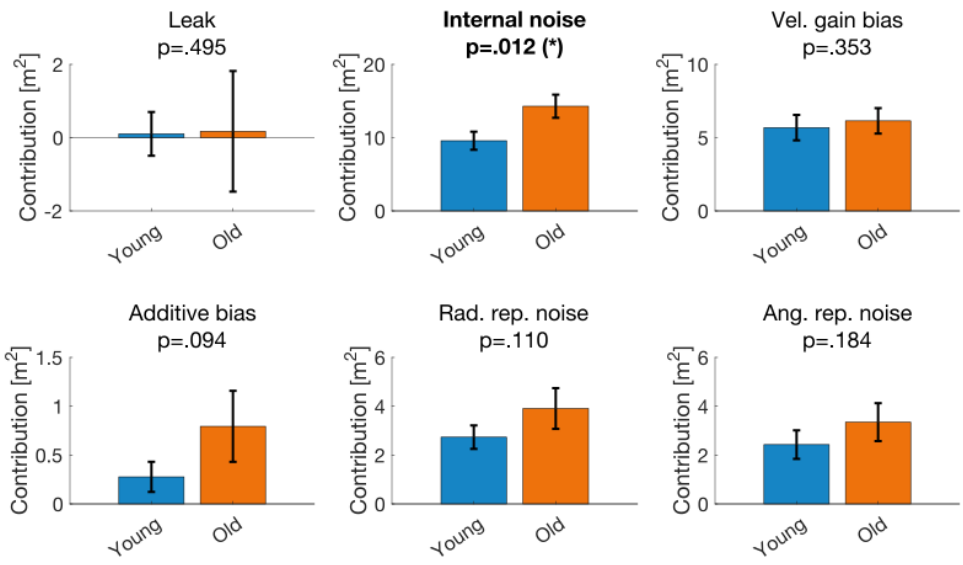

Figure 52: Contribution of error sources to overall error in young versus older adults

*Each model parameter's contribution to the square error, averaged over participants of the same age group, compared between young and older adults. Only internal noise resulted in a significant difference in error contribution between age groups. A parameter's contribution is calculated by measuring the reduction in square error when setting the parameter to its ideal value corresponding to unbiased, noiseless integration (see Appendix 2 for more details). * denotes significant effects in a one-sided permutation test ($p < 0.05$).*

5.4 Discussion

In the present study, we used a virtual reality path integration task, in which young and older adults had to keep track of their own position and orientation using visual and body-based self-motion cues while travelling along curved path segments. Moreover, we developed a computational model to decompose path integration errors and simultaneously estimate, on a trial-to-trial basis, the contribution of different sources of imperfection in the sensing and integration processes (leaky integration, multiplicative velocity gains different from unity, additive velocity biases, and unbiased or zero-mean noise in either velocity estimation or path integration or both) to the total error. In addition to these

sources of accruing error in path integration, our model also included inaccuracies in producing an explicit report of an internal displacement estimate, as subjects were asked to do at each stopping point. We performed mathematical inference on the model using an approach based on the Extended Kalman Filter (see Appendix 2 for more details), which permitted us to disentangle the different sources of error and compare their influence on path integration errors across participants and between age groups.

Previous work from Lappe and colleagues (2007, 2011) postulated that a leaky integration process might be responsible for path integration errors. Using a computational model that involved both a leaky integrator and a velocity gain bias, they could successfully explain underestimation effects when subjects had to indicate the distance to start following visual movement along straight or veering outbound paths. In our present model, the impact of both leak and velocity gain bias was relatively similar to the extent to which these two factors impacted on overall path integration performance in their studies. On the one hand, this suggests that the findings of Lappe et al. (2007, 2011) do not only apply to visual distance estimation based on optic flow, but also to more realistic path integration scenarios in with both visual and body-based cues can be used for path integration along more complex and diverse paths. On the other hand, however, using a more finely resolved computational model that includes also additional sources of error, we found that a leaky integrator is at most a modest contributor to path integration error. Instead, our model revealed that a velocity gain bias (i.e., under- or overestimation of movement velocity and, consequently, traveled distance) and noise in a person's reporting of their internal location estimate, have considerably higher impact on path integration error, as compared to relatively little contributions of leak and an additive velocity bias. Most importantly, however, our model showed that path integration computations were mainly corrupted by internal noise (i.e., a random diffusion of estimated locations away from their true value) that could, theoretically, be a consequence of neural and synaptic noise within the brain's path integration circuit (Compte et al., 2000; Brody et al., 2003; Boucheny et al., 2005; Wu et al., 2008; Burak & Fiete, 2012).

Given the large body of research suggesting that grid cells are the underlying neuronal source of path integration computations (Hafting et al., 2005; Fuhs & Touretzky, 2006; McNaughton et al., 2006; Burgess et al., 2007; Guanella et al., 2007; Hasselmo, 2008; Burak & Fiete, 2009; Giocomo et al., 2011; Zilli, 2012; Widloski & Fiete, 2014; Gil et al., 2018; Stangl et al., 2018), one could hypothesize that the internal noise stems from noisy computations in the grid cell system. Similarly, noisy coding of heading direction by head direction cells, or noise in the vestibular system, which also conveys information about position and orientation of the body, might be other potential origins of internal path integration noise. We note, however, that our model does not allow to conclude whether internal noise actually originates in one of these systems, and it cannot distinguish whether these systems itself may be malfunctioning or whether they receive a noisy input signal from earlier levels along the processing stream of positional and velocity information.

In line with previous studies (Mahmood et al., 2009; Adamo et al., 2012; Harris & Wolbers, 2012; Bates & Wolbers, 2014), the present work also shows that path integration performance is reduced in older as compared to young adults. Comparing the impact of the different contributors to path integration errors between young and older adults revealed a significantly higher magnitude of internal noise in path integration computations of older adults, whereas other sources of error were not significantly different between age groups. As discussed earlier, this might reflect a higher noise level in older adults' velocity estimation, or noisier coding of self-position in spatially-tuned neurons such as grid cells. Most recently, we have demonstrated that grid-cell-like representations in the human entorhinal cortex are compromised in old age, and that this impairment is associated with higher path integration errors (Stangl et al., 2018). Furthermore, there is evidence that certain aspects of the vestibular system deteriorate with age (for a review, see Allen et al., 2016), and vestibular loss has also been shown to affect path integration performance (Glasauer et al., 2002; Xie et al., 2017). While these findings strengthen the idea that noise on a neuronal level (e.g., in the grid cell network or in the vestibular system) may be responsible for deficient computations of self-position in old age, it remains an

important goal for future studies to determine the exact factors that underlie increased internal noise in older adults' path integration computations.

5.5 Contributions and acknowledgements

Matthias Stangl (MS) carried out this project in a collaborative effort with Ingmar Kanitscheider (IK), Martin Riemer (MR), Swantje Petersen (SP), Ila Fiete (IF), and Thomas Wolbers (TW). MS, IK, IF and TW conceptualized the work. MS was responsible for project administration. MS and MR programmed the path integration task. MS and SP acquired the data. IK and IF developed the computational path integration model. MS and IK analyzed the data, visualized the results, and drafted the manuscript (Stangl et al., in preparation). All authors edited the manuscript. IF and TW supervised the work.

We express our gratitude to Falko Eckardt, Mareen Hanelt, Patrick Hauff, Anita Hökelmann, Marko Kirbach, Claudia Marx, Mona Reißberg and Uwe Sobieray for their help with data acquisition, project administration, and technical assistance.

This work was supported by the Collaborative Research in Computational Neuroscience Grant (01GQ1303) of the German Ministry of Education and Research (BMBF) and by the European Research Council Starting Investigator Grant AGESPACE (335090).

6. GENERAL DISCUSSION

6.1 Summary

The analysis of human grid-cell-like representations is distinctly non-trivial and requires knowledge not only of fMRI analysis methods in general, but also of advanced computer programming and specific mathematical techniques. The complexity of this analysis method, and the fact that it is not included in standard fMRI analysis packages, might explain why there remain relatively few published studies in the area of human grid-cell-like representation research so far, despite the great interest in this cutting-edge research field. In Project A, entitled “The Grid Code Analysis Toolbox (GridCAT)”, a detailed review of the analysis method for the detection and investigation of grid-cell-like representations in human fMRI data is provided, and different analysis strategies that were applied in previous publications are synthesized and discussed in detail. Moreover, within Project A, we have developed the MATLAB-based open-source Grid Code Analysis Toolbox (GridCAT) for the automated analysis of grid-cell-like representations in fMRI signals. The GridCAT can be used to detect grid-cell-like representations in the human brain, and to calculate several properties of grid-cell-like representations, such as their spatial and temporal stability. In addition, the GridCAT includes several plotting and data export functions to visualize and further analyze these properties depending on the user’s specific research question. The GridCAT comes with a graphical user interface, allowing researchers to analyze grid-cell-like representations without the need to develop their own analysis code. On the one hand, this enables researchers to carry out analyses of grid-cell-like representations, regardless of their computer programming abilities. On the other hand, it saves time also for experienced programmers, as they do not have to develop the analysis pipeline themselves but can use the GridCAT’s analysis functions and tailor them to their specific needs by adapting the openly available source code. In order to make

adaptations of the source code and extensions of the GridCAT's functionality as easy as possible, the toolbox also comes along with example scripts in which the source code is explained step-by-step. Finally, users can learn and explore the GridCAT's functionality with the help of the detailed manual, and reproduce the results presented in Project A of this thesis by applying all analysis functions to an openly available example dataset. Together, reviewing the analysis method and developing the GridCAT in Project A not only laid the foundation for further projects in this thesis, but will also support other researchers to conduct investigations of grid-cell-like representations, helping to elucidate the role of grid-cell-like representations in human cognition.

The grid cell's main location within the brain, the entorhinal cortex, is known to be particularly vulnerable to age-related neurodegeneration and, theoretically, such neurodegenerative processes could lead to an impaired function of the grid cell system (as discussed in more detail in Section 1.2.2 of this thesis). To date, however, it is unknown whether grid cell function changes in the course of normal healthy aging. In Project B of this thesis, entitled "Grid-cell-like representations in old age", we therefore applied the GridCAT to investigate grid-cell-like representations in healthy and cognitively normal young and older adults. In line with previous studies (Doeller et al., 2010; Kunz et al., 2015), we found a significant magnitude of grid-cell-like representations in young adults while they were navigating a virtual environment in an object-location memory task during fMRI scanning. In older adults, however, grid-cell-like representation magnitudes were significantly lower than in young adults. Further analyses showed that this difference in grid-cell-like representation magnitudes between young and older adults was predominantly driven by a reduced temporal stability (i.e., grid orientations of grid-cell-like representations in older adults were less stable over time), whereas spatial stability of grid-cell-like representations (i.e., coherence of grid orientations across voxels) seemed to be preserved in old age. Control analyses confirmed that the detected grid-cell-like representations in young adults show the typical 6-fold symmetry that is expected from the putative firing of grid cells, rather than control models testing for other periodicities (i.e., 5-fold or 7-fold symmetric representations). In further control analyses, we

confirmed that our finding of reduced grid-cell-like representations in older adults was not driven by other age-related behavioral and neurophysiological differences between young and older adults, such as differences in entorhinal cortex volume or signal quality, head movement during scanning, performance during the navigation task, or different data amounts between young and older adults that resulted from differences in task behavior. In sum, we have demonstrated in Project B that human grid-cell-like representations, and specifically their stability over time, are compromised in healthy older adults. Given the importance of grid cells for spatial navigation functions, such an impairment could, theoretically, serve as a mechanistic explanation for navigational deficits frequently observed in old age.

Building on the finding of compromised grid-cell-like representations in older adults, we then aimed to investigate whether reduced magnitudes of grid-cell-like representations are associated with spatial navigation deficits. In Project C of this thesis, entitled “Compromised grid-cell-like representations as a mechanistic explanation for age-related path integration deficits”, we therefore re-invited the same young and older participants from Project B (in whom we had already analyzed their grid-cell-like representations). We asked them to perform a novel behavioral path integration task, in which they had to integrate self-motion cues during movement along pre-defined curved paths. This task was performed in two different modalities, allowing path integration to be based on body-based or visual self-motion cues only. These data enabled us to estimate each participant’s path integration performance, independently for the body-based and the visual modality. In accordance with results from previous studies (e.g., Mahmood et al., 2009; Adamo et al., 2012; Harris & Wolbers, 2012; Bates & Wolbers, 2014) we found that path integration performance was lower in older than in young adults, independently for both modalities, suggesting that older adults show a modality-independent deficit in computations of self-position. Most interestingly, we found an association between individual magnitudes of grid-cell-like representations and path integration performance in older adults. Specifically, older adults with low grid-cell-like representation magnitudes showed larger errors in the path integration task. This association between grid-

cell-like representations and path integration performance was also confirmed by a multiple linear regression analysis, in which path integration performance of older adults could be predicted by grid-cell-like representation magnitudes, but not by demographic factors or a range of neuropsychological test scores. These results provide further support for the hypothesis that grid cell function underlies path integration computations, as suggested previously (Fuhs & Touretzky, 2006; McNaughton et al., 2006; Burgess et al., 2007; Guanella et al., 2007; Hasselmo, 2008; Burak & Fiete, 2009; Giocomo et al., 2011; Zilli, 2012; Widloski & Fiete, 2014). Together, the results of this project support the hypothesis that compromised grid-cell-like representations in the human entorhinal cortex might serve as a mechanistic explanation for age-related deficits in path integration.

While compromised grid-cell-like representations could be a key mechanism in explaining known path integration deficits in old age, we do not know whether and to what extent other factors may also contribute to path integration errors in both young and older adults. In Project D, entitled “Sources of path integration error in young and older adults”, we therefore aimed to take into account also other potential error sources and characterized their individual impact on overall path integration errors. We used a path integration task in which participants of different ages had to keep track of their own position and orientation by integrating both body-based and visual self-motion cues during movement in virtual environments. Developing a novel computational model allowed us to decompose path integration errors into distinct causes, including memory decay (“leak”), internal noise in path integration computations, different bias-types, and reporting errors. Applying our computational model on the empirical data revealed that path integration errors (in both young and older adults) are explained mainly by unbiased noise that could, theoretically, be a consequence of noise within the brain’s path integration circuit or of noise in the velocity inputs delivered to the neural path integrator. Comparing the components of error in young and older adults revealed a significantly higher magnitude of unbiased noise in path integration computations of older adults, while other sources of error were not significantly different between age groups. In other words, the biggest source of error in young adults is further magnified in aging adults, while

the smaller sources of error are not significantly compromised with age and therefore seem to only play a minor role for age-related path integration deficits. Cumulatively, these results provide further support for the notion that noise on a neuronal level, which may arise from noisier coding of self-position in spatially-tuned neurons such as grid cells, could be responsible for deficient navigational computations in old age.

6.2 Limitations

6.2.1 Limitations related to the Grid Code Analysis Toolbox

By developing the GridCAT and making the whole output of this project (including a detailed description of the method, open source MATLAB code, a graphical user interface, and a detailed manual) freely and openly available online, we aimed to enable researchers worldwide to carry out analyses of human grid-cell-like representations with as few limitations as possible. However, there are still some limitations of the toolbox, which might limit its use for some users.

First and foremost, the toolbox requires a MATLAB installation. Although research institutions and Universities often provide MATLAB for their students and researchers, not everyone who might be interested in carrying out analyses of grid-cell-like representations will also own or have access to a MATLAB license or will be able to buy this software. Therefore, it would be desirable in future to translate the toolbox to different programming languages, for which no license or costly software framework needs to be bought.

Second, the GridCAT is able to only analyze the putative firing of grid cells during movement (be it in a virtual environment, in visual space, or in abstract space) on a two-dimensional (2D) plane. To date, there is no animal or human study that reports how the firing pattern of grid cells looks during movement in three-dimensional (3D) space, presumably because of the technical difficulties of recording from freely moving animals during 3D movements. But researchers

have already started to develop theoretical assumptions and models about the hypothesized 3D grid cell firing pattern (Jeffery et al., 2015; Stella & Treves, 2015; Kim & Maguire, 2018). Due to the lack of knowledge about grid cell firing properties in 3D space, and how these might modulate the BOLD signal in fMRI measurements, the GridCAT is not designed to analyze data from 3D movement, at least not in its current version.

Third, it is not clear how the different combinations of analysis options within the GridCAT impact on analysis results. Although the basic methodology for investigating human grid-cell-like representations in fMRI data was similar across previously published studies, the exact details of their analysis strategies still differed in several aspects. The GridCAT was designed to be flexible and to offer a variety of options that have been used previously or that might be potentially useful for future studies, but it does neither provide a systematic comparison of using different combinations of model parameters and analysis settings, nor a critique as to best practice for investigating grid-cell-like representations. Therefore, determining the exact factors that aid detection of human grid-cell-like representations in fMRI data remains to be addressed in future studies.

Fourth, the GridCAT does not offer a representational similarity analysis (RSA) or multi-voxel pattern analysis (MVPA) approach to analyze grid-cell-like representations. Rather than the mass univariate method commonly used to examine grid-cell-like representations in human fMRI data, one study by Bellmund et al. (2016) applied MVPA to provide evidence for grid-cell-like representations in the entorhinal cortex during mental simulation. To date, however, the GridCAT does not support this analysis method, but rather offers some data export options in order to allow users to analyze their data with additional software, such as the MVPA/RSA toolboxes from Nili et al. (2014) or Oosterhof et al. (2016).

6.2.2 Limitations related to our scientific findings

There are also some limitations of our scientific findings in Projects B, C, and D, in which we have investigated age-related changes in grid-cell-like

representations as well as the sources and neuronal mechanisms underlying path integration errors and age-related path integration deficits.

First, all of the results presented in this thesis stem from cross-sectional studies. Consequently, this work can only provide a snapshot of the differences between young and older adults, but it does not allow conclusions about how effects have developed in the past or might develop in the future. For example, we tested only healthy young and older adults that did not show signs of cognitive decline at the time of testing, based on a screening tool for mild cognitive impairment (Nasreddine et al., 2005). However, previous studies have reported that older adults might already show early symptoms of neurodegeneration (such as a pathological deposition of the tau protein in the entorhinal cortex) at a time before cognitive deficits can be detected (Braak & Del Tredici, 2015; Mufson et al., 2016). We therefore cannot exclude that our findings (e.g., reduced grid-cell-like representations in the entorhinal cortex and increased in noise in path integration computations of older adults, as well as age-related path integration deficits) might – at least to some extent – be driven by a proportion of older adults who were affected by neurodegenerative processes already. Longitudinal studies or follow-up measurements with our participants would be necessary in order to specify whether those participants who showed reduced grid-cell-like representation magnitudes, increased internal path integration noise, or path integration deficits, will also develop pathological signs of cognitive decline or dementia in the future.

Second, our investigations of grid-cell-like representations were focused on the entorhinal cortex but not other brain regions. Studies in rodents, bats, and nonhuman primates have identified the entorhinal cortex as the grid cell's primary location. Nevertheless, fMRI investigations in humans provided evidence for grid-cell-like representations also in several other brain regions, such as parietal, lateral temporal, and prefrontal areas (Doeller et al., 2010; Constantinescu et al., 2016). Since grid-cell-like representations in the human entorhinal cortex have been found to be compromised in a group of young adults at increased genetic risk for Alzheimer's disease (Kunz et al., 2015), we

prioritized this region and aimed to acquire fMRI data from the entorhinal cortex with relatively high spatial and temporal resolution. Due to these high-resolution images, however, we were able only to acquire partial volume fMRI images centered on the entorhinal cortex, limiting our coverage of more distant brain areas. But recent developments in fMRI scanning techniques, such as multiband sequences, might allow for high-resolution functional images of the whole brain and will therefore provide a more comprehensive picture of the human grid cell system in future studies.

Third, when combining data from Project B and Project C of this thesis, we found an association between grid-cell-like representations in older but not in young adults. In young adults, however, we found a significant correlation between grid-cell-like representation magnitudes and path integration performance only for a subgroup with low grid-cell-like representation magnitudes and only for the body-based path integration modality. Following these findings, we hypothesized that an association between grid-cell-like representation magnitudes and path integration performance can only be seen when grid-cell-like representations are compromised and the grid cell system is therefore not able to provide reliable computations of positional information. We note, however, that this hypothesis remains speculative, given that these results were calculated only on a relatively small sample size (i.e., only five young adults showed low grid-cell-like representation magnitudes). Furthermore, the results were rather inconclusive, given that low grid-cell-like representation magnitudes in young adults were only correlated with path integration performance in the body-based but not in the visual modality.

Fourth, we want to point out that associations between grid-cell-like representations and path integration performance in our study do not necessarily reflect a causal relationship. In our data, we found a link between grid-cell-like representations and path integration performance separately for two independent path integration modalities, through both a correlational analysis and a multiple linear regression analysis. Such a link seems theoretically plausible, as a large body of previous research suggests that grid cells would provide the neuronal

basis for path integration computations (Fuhs & Touretzky, 2006; McNaughton et al., 2006; Burgess et al., 2007; Guanella et al., 2007; Hasselmo, 2008; Burak & Fiete, 2009; Giocomo et al., 2011; Zilli, 2012; Widloski & Fiete, 2014; Gil et al., 2018). Nevertheless, the correlational methods used in the present studies do not test causal relationships between grid-cell-like representations and path integration performance. Therefore, further research is needed to determine the precise nature of the link between grid-cell-like representations and path integration computations.

Finally, while our computational path integration model supports the notion that noise on a neuronal level may be responsible for age-related degradation of path integration performance, it cannot provide evidence as to the actual origin of this noise. Theoretically, such internal noise can be a consequence of noise within the brain's path integration circuit or of noise in the velocity inputs delivered to the neural path integrator (Compte et al., 2000; Brody et al., 2003; Boucheny et al., 2005; Wu et al., 2008; Burak & Fiete, 2012). Noise within the path integration circuit, in turn, might correspond to stochastic neural or synaptic processes within the grid cell system. Similarly, noise in sensory systems (e.g. in the visual, vestibular, and proprioceptive peripheries) as well as in the downstream coding and processing systems for the estimation of self-motion could contribute to noise-like errors in our model. Without an independent measurement of the velocity estimates of the subject, however, our model cannot distinguish between noise in the velocity input to the integrator versus the intrinsic operation of the integrator. The precise origin of internal noise in path integration computations therefore remains to be determined in future studies.

6.3 Implications and future perspectives

Implementing analyses of grid-cell-like representations in human fMRI data is a time-consuming and non-trivial task that requires advanced computer programming and mathematical skills. We have therefore developed the GridCAT in order to save time for researchers, and also to enable those who

might not possess these skills to carry out such analyses. As the GridCAT's source code is open to everyone and its license allows any modification and extension of its functionality, new and additional features can be easily added to the toolbox by researchers around the world. For example, additional functions could be included in the toolbox to allow analyses not only by mass univariate approaches but also MVPA or RSA methods. Moreover, translating the open source code to other programming languages that are not depending on a costly software framework, would allow an even more widespread use of the toolbox and further speed-up progress in this research field. By making the GridCAT freely and openly available to all users, and by providing a comprehensive overview and synthesizing the different analysis strategies for the analysis of grid-cell-like representations, we hope that we can open up this exciting research area to the wider neuroscience community and help to address novel research questions regarding the role of grid cells and grid-cell-like representations in human cognition.

For example, one such key question has been addressed within this thesis: Does aging affect grid cells and could age-related changes in grid cell function be associated with impairments in spatial navigation computations? The results of Projects B and C support the hypothesis that compromised grid-cell-like representations could be a key mechanism to explain path integration deficits in older adults. Moreover, our computational model further strengthens this notion based on two findings in Project D: First, the model identified internal noise in path integration computations as the main source of path integration error, which may arise from dysfunctional coding in spatially-tunes neurons such as grid cells. Second, the model revealed that other factors, such as memory decay, biases, or errors in reporting an internal location estimate, play only a minor role for path integration errors across individuals and in explaining age-related path integration deficits.

While our computational model included a range of potential error sources that can corrupt path integration performance in young and old age, we do not know how and to what extent individual sources of error are influenced by specific

cognitive processes that might also be involved in path integration computations. For example, Petzschner and colleagues suggested that knowledge about prior experience could be dynamically incorporated into current estimates of displacement and therefore also impact on path integration performance (Petzschner & Glasauer, 2011; Petzschner et al., 2015). As we have isolated here the different sources of error and characterized their individual impact on overall path integration performance, our work has also laid the foundation for future studies to investigate the impact of additional error sources on navigational abilities and age-related navigational deficits, such as a-priori assumptions that subjects have about the world.

Building on the findings in this thesis, another important research question for future studies will be: What causes compromised human grid-cell-like representations in the entorhinal cortex and increased internal noise in path integration computations of older adults? Hypothetically, reduced grid-cell-like representations and internal noise could be a consequence of neurodegenerative processes such as a pathological deposition of harmful amyloid-β plaques and tau in neurofibrillary tangles. Previous studies have shown an increased accumulation particularly of the tau protein in the entorhinal cortex of older adults who do not show signs of cognitive decline (Braak & Del Tredici, 2015; Mufson et al., 2016). Such an accumulation of tau, in turn, can cause synaptic dysfunction and neuronal loss (Gómez-Isla et al., 1997; Di et al., 2016; Bejanin et al., 2017). And indeed, Fu et al. (2017) most recently found that tau pathology in old mice induced impaired grid cell function. Consequently, one could assume that pathological tau accumulation might be the driving factor behind our finding of compromised human grid-cell-like representations in old age, which might in turn explain noisier path integration computations and higher path integration errors. In order to test this important hypothesis, future studies could combine fMRI measurements of human grid-cell-like representations with positron emission tomography (PET) scanning to quantify tau pathology in humans, and investigate the relationship between these two measures.

Alternatively, compromised grid-cell-like representations as well as increased noise in older adults' path integration computations could also be a consequence of dysfunctional input to grid cells, potentially from earlier levels along the processing stream of positional information. It has been shown that the entorhinal cortex receives input from the head direction system (Alonso & Klink, 1993; Amaral & Witter, 1995; Burgess et al., 2007) and that the firing of grid cells is often modulated by head direction (Sargolini et al., 2006). Impaired head direction signal input to the grid cell system would therefore be another potential explanation for grid cell dysfunction and internal path integration noise. Theoretically, if grid cells receive deficient input from the head direction system, like a higher variability in directional coding, this might cause less stable and more variable grid cell firing, leading to noisier and less accurate path integration computations. As no study has yet investigated age-related changes in the head direction system, future studies could apply combined measurements of the head direction cell and the grid cell system, in order to shed light on this open question.

In addition, age-related impairments in vestibular processing might also be related to our findings of noisier path integration computations and compromised grid-cell-like representations in older adults. It is known that certain aspects of the vestibular system deteriorate with age (for a review, see Allen et al., 2016). Also, previous studies suggest that the vestibular system provides critical input for the generation of spatial representations (Horii et al., 1994; Stackman et al., 2002; Yoder & Taube, 2014). As vestibular signals convey information about position and orientation of the body, age-related impairments in the vestibular system could lead to noisier and imprecise coding in spatially selective cells, including grid cells. This might, in turn, explain results from previous studies showing that vestibular loss is associated with path integration deficits (Glasauer et al., 2002; Xie et al., 2017). Testing this hypothesis as well as a more precise characterization of the vestibular system’s impact on grid cell function and grid-cell-like representations, however, awaits further investigation.

We note that, even though magnitudes of grid-cell-like representations were on average lower in older than in young adults, a proportion of older adults in our sample, namely those who performed well in the path integration task, showed normal magnitudes of grid-cell-like representations. In fact, grid-cell-like representation magnitudes of these older adults could not be distinguished from magnitudes of young adults in our sample. It is unclear, however, which factors distinguish those older adults with low grid-cell-like representation magnitudes from those in which grid-cell-like representations seem to be preserved. Future studies might aim to identify the factors that protect individuals from decline in grid-cell-like representations during aging. For example, investigating such protective factors in longitudinal studies with larger sample sizes might provide important insight into the factors that distinguish healthy older adults from those with navigational deficits. In turn, this would be an important step towards the development of efficient interventions and therapeutic approaches to counteract age-related decline in navigational functions.

As of this writing, all studies on human grid-cell-like representations, including the studies in this thesis, have exclusively investigated healthy individuals. However, it might be a promising future research approach to examine grid-cell-like representations not only in healthy individuals but also in longitudinal studies with groups of patients during the development of neurodegenerative disorders such as Alzheimer's disease. It has been shown that the entorhinal cortex is one of the regions that is affected earliest by the neuropathology of Alzheimer's disease (Braak & Braak, 1991; Gómez-Isla et al., 1996; Du et al., 2001; Pennanen et al., 2004; Masdeu et al., 2005; Stranahan & Mattson, 2010; Khan et al., 2014), and the study of Kunz et al. (2015) demonstrated that already healthy young adults at increased genetic risk of Alzheimer's disease show changes in entorhinal grid-cell-like representations. It should therefore be explored whether grid-cell-like representations might serve as a potential biomarker for integrity of the grid cell system and entorhinal cortex function, as such a biomarker could aid early detection of Alzheimer's disease by identifying earliest neuropathological changes before detectable cognitive symptoms are shown.

Moreover, not only the detection of neurophysiological changes, such as compromised grid-cell-like representations, but also tasks measuring navigational abilities could help to detect pathological development in early stages of Alzheimer's disease. The brain's key regions for spatial navigation, such as the entorhinal and perirhinal cortex, hippocampus, precuneus, and retrosplenial cortex, are amongst the first cortical structures that are affected by Alzheimer's pathology (Braak & Braak, 1995; Pengas et al., 2010; Jagust, 2018). It is therefore not surprising that behavioral deficits in navigation tasks belong to the earliest symptoms of Alzheimer's disease (Hort et al., 2007; Laczó et al., 2010; Mokrisova et al., 2016). Consequently, assessing navigational abilities in older adults, for example with tasks measuring path integration performance, might facilitate early detection of neuropathological changes and predict the development of Alzheimer's disease or cognitive impairments on an individual basis. Given the necessity to stop the progression of Alzheimer's pathology as early as possible, it would be an important research goal to adopt a longitudinal approach and explore the clinical potential of assessing both grid-cell-like representations and spatial navigation abilities for an early prediction of Alzheimer's disease.

Ever since their discovery, grid cells were thought to provide a metric for space and support spatial navigation computations. In recent years, however, several studies have demonstrated that grid cells and grid-cell-like representations are involved not only in spatial navigation computations, but also in other cognitive functions, including auditory processing in rats (Aronov et al., 2017), visual processing in humans (Julian et al., 2018; Nau et al., 2018) and non-human primates (Killian et al., 2012), as well as mechanisms for organizing conceptual knowledge in the human memory network (Constantinescu et al., 2016). Therefore, future investigations will show whether age-related changes in the grid cell system might explain not only navigational deficits in old age, but also a more general decline in higher-order cognitive functions beyond spatial navigation.

REFERENCES

Adamo, D. E., Briceño, E. M., Sindone, J. A., Alexander, N. B., & Moffat, S. D. (2012). Age differences in virtual environment and real world path integration. *Frontiers in Aging Neuroscience*, *4*, 26.

Allen, D., Ribeiro, L., Arshad, Q., & Seemungal, B. M. (2016). Age-Related Vestibular Loss: Current Understanding and Future Research Directions. *Frontiers in Neurology*, *7*, 231.

Allen, G. L., Kirasic, K. C., Rashotte, M. A., & Haun, D. B. M. (2004). Aging and path integration skill: Kinesthetic and vestibular contributions to wayfinding. *Perception & Psychophysics*, *66*, 170–179.

Alonso, A., & Klink, R. (1993). Differential electroresponsiveness of stellate and pyramidal-like cells of medial entorhinal cortex layer II. *Journal of Neurophysiology*, *70*, 128–143.

Amaral, D., & Witter, M. (1995). The Hippocampus. In Paxinos G (Ed.), *The Rat Nervous System. 2nd ed.* (pp. 443–493). Ney York.

Aronov, D., Nevers, R., & Tank, D. W. (2017). Mapping of a non-spatial dimension by the hippocampal-entorhinal circuit. *Nature*, *543*, 719–722.

Barnes, C. A., Suster, M. S., Shen, J., & McNaughton, B. L. (1997). Multistability of cognitive maps in the hippocampus of old rats. *Nature*, *388*, 272–275.

Barry, C., Hayman, R., Burgess, N., & Jeffery, K. J. (2007). Experience-dependent rescaling of entorhinal grids. *Nature Neuroscience*, *10*, 682–684.

Bassett, J. P., & Taube, J. S. (2001). Neural correlates for angular head velocity in the rat dorsal tegmental nucleus. *The Journal of Neuroscience*, *21*, 5740–5751.

Bates, S. L., & Wolbers, T. (2014). How cognitive aging affects multisensory integration of navigational cues. *Neurobiology of Aging*, *35*, 2761–2769.

Bejanin, A., Schonhaut, D. R., La Joie, R., Kramer, J. H., Baker, S. L., Sosa, N., Ayakta, N., Cantwell, A., … Rabinovici, G. D. (2017). Tau pathology and neurodegeneration contribute to cognitive impairment in Alzheimer's disease. *Brain*, *140*, 3286–3300.

Bellmund, J. L., Deuker, L., Navarro Schröder, T., & Doeller, C. F. (2016). Grid-cell representations in mental simulation. *eLife*, *5*, 12897–12901.

Berens, P. (2009). CircStat: A MATLAB Toolbox for Circular Statistics. *Journal of Statistical Software*, *31*, 1–21.

Berron, D., Vieweg, P., Hochkeppler, A., Pluta, J. B., Ding, S.-L., Maass, A., Luther, A., Xie, L., … Wisse, L. E. M. (2017). A protocol for manual segmentation of medial temporal lobe subregions in 7Tesla MRI. *NeuroImage: Clinical*, *15*, 466–482.

Biazoli, C. E., Goto, M., Campos, A. M. P., & Canteras, N. S. (2006). The supragenual nucleus: A putative relay station for ascending vestibular signs to head direction cells. *Brain Research*, *1094*, 138–148.

Boucheny, C., Brunel, N., & Arleo, A. (2005). A continuous attractor network model without recurrent excitation: Maintenance and integration in the head direction cell system. *Journal of Computational Neuroscience*, *18*, 205–227.

Braak, H., & Braak, E. (1991). Neuropathological stageing of Alzheimer-related changes. *Acta Neuropathologica*, *82*, 239–259.

Braak, H., & Braak, E. (1995). Staging of Alzheimer's disease-related neurofibrillary changes. *Neurobiology of Aging*, *16*, 271–278.

Braak, H., & Del Tredici, K. (2015). The preclinical phase of the pathological process underlying sporadic Alzheimer's disease. *Brain*, *138*, 2814–2833.

Britten, K. H. (2008). Mechanisms of Self-Motion Perception. *Annual Review of Neuroscience*, *31*, 389–410.

Brody, C. D., Romo, R., & Kepecs, A. (2003). Basic mechanisms for graded persistent activity: Discrete attractors, continuous attractors, and dynamic representations. *Current Opinion in Neurobiology*, *13*, 204–211.

Brun, V. H., Leutgeb, S., Wu, H.-Q., Schwarcz, R., Witter, M. P., Moser, E. I., & Moser, M.-B. (2008). Impaired spatial representation in CA1 after lesion of direct input from entorhinal cortex. *Neuron*, *57*, 290–302.

Brunton, B. W., Botvinick, M. M., & Brody, C. D. (2013). Rats and Humans Can Optimally Accumulate Evidence for Decision-Making. *Science*, *340*, 95–98.

Burak, Y., & Fiete, I. R. (2009). Accurate Path Integration in Continuous Attractor Network Models of Grid Cells. *PLoS Computational Biology*, *5*, e1000291.

Burak, Y., & Fiete, I. R. (2012). Fundamental limits on persistent activity in networks of noisy neurons. *Proceedings of the National Academy of Sciences*, *109*, 17645–17650.

Burgess, N., Barry, C., & O'Keefe, J. (2007). An oscillatory interference model of grid cell firing. *Hippocampus*, *17*, 801–812.

Butler, W. N., & Taube, J. S. (2015). The nucleus prepositus hypoglossi contributes to head direction cell stability in rats. *The Journal of Neuroscience*, *35*, 2547–2558.

Chrastil, E. R., Sherrill, K. R., Aselcioglu, I., Hasselmo, M. E., & Stern, C. E. (2017). Individual Differences in Human Path Integration Abilities Correlate with Gray Matter Volume in Retrosplenial Cortex, Hippocampus, and Medial Prefrontal Cortex. *eNeuro*, *4*, 0346-16.

Clark, B. J., Brown, J. E., & Taube, J. S. (2012). Head direction cell activity in the anterodorsal thalamus requires intact supragenual nuclei. *Journal of Neurophysiology*, *108*, 2767–2784.

Colombo, D., Serino, S., Tuena, C., Pedroli, E., Dakanalis, A., Cipresso, P., & Riva, G. (2017). Egocentric and allocentric spatial reference frames in aging: A systematic review. *Neuroscience & Biobehavioral Reviews*, *80*, 605–621.

Compte, A., Brunel, N., Goldman-Rakic, P. S., & Wang, X. J. (2000). Synaptic mechanisms and network dynamics underlying spatial working memory in a cortical network model. *Cerebral Cortex*, *10*, 910–923.

Constantinescu, A. O., O'Reilly, J. X., & Behrens, T. E. J. (2016). Organizing conceptual knowledge in humans with a gridlike code. *Science*, *352*, 1464–1468.

Cornsweet, T. N., & Teller, D. Y. (1965). Relation of increment thresholds to brightness and luminance. *Journal of the Optical Society of America*, *55*, 1303–1308.

Cullen, K. E. (2012). The vestibular system: Multimodal integration and encoding of self-motion for motor control. *Trends in Neurosciences*, *35*, 185–196.

Daugherty, A. M., Yuan, P., Dahle, C. L., Bender, A. R., Yang, Y., & Raz, N. (2015). Path Complexity in Virtual Water Maze Navigation: Differential Associations with Age, Sex, and Regional Brain Volume. *Cerebral Cortex*, *25*, 3122–3131.

de Almeida, L., Idiart, M., & Lisman, J. E. (2009). The input-output transformation of the hippocampal granule cells: From grid cells to place fields. *The Journal of Neuroscience*, *29*, 7504–7512.

Di, J., Cohen, L. S., Corbo, C. P., Phillips, G. R., El Idrissi, A., & Alonso, A. D. (2016). Abnormal tau induces cognitive impairment through two different mechanisms: Synaptic dysfunction and neuronal loss. *Scientific Reports*, *6*, 20833.

Ding, S.-L., Royall, J. J., Sunkin, S. M., Ng, L., Facer, B. A. C., Lesnar, P., Guillozet-Bongaarts, A., McMurray, B., … Lein, E. S. (2016). Comprehensive cellular-resolution atlas of the adult human brain. *Journal of Comparative Neurology*, *524*, 3127–3481.

Doeller, C. F., Barry, C., & Burgess, N. (2010). Evidence for grid cells in a human memory network. *Nature*, *463*, 657–661.

Du, A. T., Schuff, N., Amend, D., Laakso, M. P., Hsu, Y. Y., Jagust, W. J., Yaffe, K., Kramer, J. H., … Weiner, M. W. (2001). Magnetic resonance imaging of the entorhinal cortex and hippocampus in mild cognitive impairment and Alzheimer's disease. *Journal of Neurology, Neurosurgery & Psychiatry*, *71*, 441–447.

Ekstrom, A. D., Kahana, M. J., Caplan, J. B., Fields, T. A., Isham, E. A., Newman, E. L., & Fried, I. (2003). Cellular networks underlying human spatial navigation. *Nature*, *425*, 184–188.

Etienne, A. S., & Jeffery, K. J. (2004). Path integration in mammals. *Hippocampus*, *14*, 180–192.

Faisal, A. A., Selen, L. P. J., & Wolpert, D. M. (2008). Noise in the nervous system. *Nature Reviews Neuroscience*, *9*, 292–303.

Fechner, G. (1966). *Elements of Psychophysics*. (D. H. Howes, Ed.). New York City: Holt, Rinehart and Winston.

Feigenbaum, J. D., & Rolls, E. T. (1991). Allocentric and egocentric spatial information processing in the hippocampal formation of the behaving primate. *Psychobiology*, *19*, 21–40.

Fjell, A. M., Westlye, L. T., Grydeland, H., Amlien, I., Espeseth, T., Reinvang, I., Raz, N., Dale, A. M., … Alzheimer Disease Neuroimaging Initiative. (2014). Accelerating Cortical Thinning: Unique to Dementia or Universal in Aging? *Cerebral Cortex*, *24*, 919–934.

Fu, H., Rodriguez, G. A., Herman, M., Emrani, S., Nahmani, E., Barrett, G., Figueroa, H. Y., Goldberg, E., … Al., E. (2017). Tau Pathology Induces Excitatory Neuron Loss, Grid Cell Dysfunction, and Spatial Memory Deficits Reminiscent of Early Alzheimer's Disease. *Neuron*, *93*, 533–541.

Fuhs, M. C., & Touretzky, D. S. (2006). A Spin Glass Model of Path Integration in Rat Medial Entorhinal Cortex. *The Journal of Neuroscience*, *26*, 4266–4276.

Fujita, N., Klatzky, R. L., Loomis, J. M., & Golledge, R. G. (1993). The Encoding-Error Model of Pathway Completion without Vision. *Geographical Analysis*, *25*, 295–314.

Fyhn, M., Hafting, T., Treves, A., Moser, M.-B., & Moser, E. I. (2007). Hippocampal remapping and grid realignment in entorhinal cortex. *Nature*, *446*, 190–194.

Fyhn, M., Molden, S., Witter, M. P., Moser, E. I., & Moser, M.-B. (2004). Spatial Representation in the Entorhinal Cortex. *Science*, *305*, 1258–1264.

Gallistel, C. R. (1990). *The organization of learning*. Cambridge, MA: MIT Press.

Gaydos, H. F. (1958). Sensitivity in the Judgment of Size by Finger-Span. *The American Journal of Psychology*, *71*, 557.

Gil, M., Ancau, M., Schlesiger, M. I., Neitz, A., Allen, K., De Marco, R. J., & Monyer, H. (2018). Impaired path integration in mice with disrupted grid cell firing. *Nature Neuroscience*, *21*, 81–91.

Giocomo, L. M., Moser, M.-B., & Moser, E. I. (2011). Computational Models of Grid Cells. *Neuron*, *71*, 589–603.

Glasauer, S., Amorim, M.-A., Viaud-Delmon, I., & Berthoz, A. (2002). Differential effects of labyrinthine dysfunction on distance and direction during blindfolded walking of a triangular path. *Experimental Brain Research*, *145*, 489–497.

Gómez-Isla, T., Hollister, R., West, H., Mui, S., Growdon, J. H., Petersen, R. C., Parisi, J. E., & Hyman, B. T. (1997). Neuronal loss correlates with but exceeds neurofibrillary tangles in Alzheimer's disease. *Annals of Neurology*, *41*, 17–24.

Gómez-Isla, T., Price, J. L., McKeel, D. W., Morris, J. C., Growdon, J. H., & Hyman, B. T. (1996). Profound loss of layer II entorhinal cortex neurons occurs in very mild Alzheimer's disease. *The Journal of Neuroscience*, *16*, 4491–4500.

Guanella, A., Kiper, D., & Verschure, P. (2007). A model of grid cells based on a twisted torus topology. *International Journal of Neural Systems*, *17*, 231–240.

Hafting, T., Fyhn, M., Molden, S., Moser, M.-B., & Moser, E. I. (2005). Microstructure of a spatial map in the entorhinal cortex. *Nature*, *436*, 801–806.

Harris, M. A., & Wolbers, T. (2012). Ageing effects on path integration and landmark navigation. *Hippocampus*, *22*, 1770–1780.

Hasselmo, M. E. (2008). Grid cell mechanisms and function: Contributions of entorhinal persistent spiking and phase resetting. *Hippocampus*, *18*, 1213–1229.

Hasselmo, M. E. (2009). A model of episodic memory: Mental time travel along encoded trajectories using grid cells. *Neurobiology of Learning and Memory*, *92*, 559–573.

Hayman, R. M., & Jeffery, K. J. (2008). How heterogeneous place cell responding arises from homogeneous grids--a contextual gating hypothesis. *Hippocampus*, *18*, 1301–1313.

Head, D., & Isom, M. (2010). Age effects on wayfinding and route learning skills. *Behavioural Brain Research*, *209*, 49–58.

Hegarty, M., Richardson, A. E., Montello, D. R., Lovelace, K., & Subbiah, I. (2002). Development of a self-report measure of environmental spatial ability. *Intelligence*, *30*, 425–447.

Hitier, M., Besnard, S., & Smith, P. F. (2014). Vestibular pathways involved in cognition. *Frontiers in Integrative Neuroscience*, *8*, 59.

Horii, A., Takeda, N., Mochizuki, T., Okakura-Mochizuki, K., Yamamoto, Y., & Yamatodani, A. (1994). Effects of vestibular stimulation on acetylcholine release from rat hippocampus: An in vivo microdialysis study. *Journal of Neurophysiology*, *72*, 605–611.

Horner, A. J., Bisby, J. A., Zotow, E., Bush, D., & Burgess, N. (2016). Grid-like Processing of Imagined Navigation. *Current Biology*, *26*, 842–847.

Hort, J., Laczó, J., Vyhnálek, M., Bojar, M., Bures, J., & Vlcek, K. (2007). Spatial navigation deficit in amnestic mild cognitive impairment. *Proceedings of the National Academy of Sciences*, *104*, 4042–4047.

Indow, T., & Stevens, S. S. (1966). Scaling of saturation and hue. *Perception & Psychophysics*, *1*, 253–271.

Izard, V., & Dehaene, S. (2008). Calibrating the mental number line. *Cognition*, *106*, 1221–1247.

Jacob, P.-Y., Gordillo-Salas, M., Facchini, J., Poucet, B., Save, E., & Sargolini, F. (2017). Medial entorhinal cortex and medial septum contribute to self-motion-based linear distance estimation. *Brain Structure and Function*, *222*, 2727–2742.

Jacob, P.-Y., Poucet, B., Liberge, M., Save, E., & Sargolini, F. (2014). Vestibular control of entorhinal cortex activity in spatial navigation. *Frontiers in Integrative Neuroscience*, *8*, 38.

Jacobs, J., Weidemann, C. T., Miller, J. F., Solway, A., Burke, J. F., Wei, X.-X., Suthana, N., Sperling, M. R., … Kahana, M. J. (2013). Direct recordings of grid-like neuronal activity in human spatial navigation. *Nature Neuroscience*, *16*, 1188–1190.

Jagust, W. (2018). Following the pathway to Alzheimer's disease. *Nature Neuroscience*, *21*, 306–308.

Jeffery, K. J., Wilson, J. J., Casali, G., & Hayman, R. M. (2015). Neural encoding of large-scale three-dimensional space-properties and constraints. *Frontiers in Psychology*, *6*, 927.

Jones, K. E., Hamilton, A. F., & Wolpert, D. M. (2002). Sources of signal-dependent noise during isometric force production. *Journal of Neurophysiology*, *88*, 1533–1544.

Julian, J. B., Keinath, A. T., Frazzetta, G., & Epstein, R. A. (2018). Human entorhinal cortex represents visual space using a boundary-anchored grid. *Nature Neuroscience*, *21*, 191–194.

Kelley, C. L., & Charness, N. (1995). Issues in training older adults to use computers. *Behaviour & Information Technology*, *14*, 107–120.

Kessels, R. P. C., van Zandvoort, M. J. E., Postma, A., Kappelle, L. J., & de Haan, E. H. F. (2000). The Corsi Block-Tapping Task: Standardization and Normative Data. *Applied Neuropsychology*, *7*, 252–258.

Khan, U. A., Liu, L., Provenzano, F. A., Berman, D. E., Profaci, C. P., Sloan, R., Mayeux, R., Duff, K. E., & Small, S. A. (2014). Molecular drivers and cortical spread of lateral entorhinal cortex dysfunction in preclinical Alzheimer's disease. *Nature Neuroscience*, *17*, 304–311.

Killian, N. J., Jutras, M. J., & Buffalo, E. A. (2012). A map of visual space in the primate entorhinal cortex. *Nature*, *491*, 761–764.

Kim, M., & Maguire, E. A. (2018). 3D grid cells in human entorhinal cortex: Theoretical and methodological considerations and fMRI findings. *bioRxiv*, 282327.

Konishi, S., & Kitagawa, G. (2008). *Information Criteria and Statistical Modeling*. New York: Springer.

Kropff, E., Carmichael, J. E., Moser, M.-B., & Moser, E. I. (2015). Speed cells in the medial entorhinal cortex. *Nature*, *523*, 419–424.

Kunz, L., Schröder, T. N., Lee, H., Montag, C., Lachmann, B., Sariyska, R., Reuter, M., Stirnberg, R., … Axmacher, N. (2015). Reduced grid-cell-like representations in adults at genetic risk for Alzheimer's disease. *Science*, *350*, 430–433.

Laczó, J., Andel, R., Vyhnalek, M., Vlcek, K., Magerova, H., Varjassyova, A., Tolar, M., & Hort, J. (2010). Human analogue of the morris water maze for testing subjects at risk of Alzheimer's disease. *Neurodegenerative Diseases*, *7*, 148–152.

Lappe, M., Jenkin, M., & Harris, L. R. (2007). Travel distance estimation from visual motion by leaky path integration. *Experimental Brain Research*, *180*, 35–48.

Lappe, M., Stiels, M., Frenz, H., & Loomis, J. M. (2011). Keeping track of the distance from home by leaky integration along veering paths. *Experimental Brain Research*, *212*, 81–89.

Lester, A. W., Moffat, S. D., Wiener, J. M., Barnes, C. A., & Wolbers, T. (2017). The Aging Navigational System. *Neuron*, *95*, 1019–1035.

Lever, C., Burton, S., Jeewajee, A., O'Keefe, J., & Burgess, N. (2009). Boundary Vector Cells in the Subiculum of the Hippocampal Formation. *The Journal of Neuroscience*, *29*, 9771–9777.

Liu, I., Levy, R. M., Barton, J. J. S., & Iaria, G. (2011). Age and gender differences in various topographical orientation strategies. *Brain Research*, *1410*, 112–119.

Loomis, J. M., Klatzky, R. L., Golledge, R. G., Cicinelli, J. G., Pellegrino, J. W., & Fry, P. A. (1993). Nonvisual navigation by blind and sighted: Assessment of path integration ability. *Journal of Experimental Psychology: General*, *122*, 73–91.

Luis, C. A., Keegan, A. P., & Mullan, M. (2009). Cross validation of the Montreal Cognitive Assessment in community dwelling older adults residing in the Southeastern US. *International Journal of Geriatric Psychiatry*, *24*, 197–201.

Lyttle, D., Gereke, B., Lin, K. K., & Fellous, J.-M. (2013). Spatial scale and place field stability in a grid-to-place cell model of the dorsoventral axis of the hippocampus. *Hippocampus*, *23*, 729–744.

Mahmood, O., Adamo, D., Briceno, E., & Moffat, S. D. (2009). Age differences in visual path integration. *Behavioural Brain Research*, *205*, 88–95.

Masdeu, J. C., Zubieta, J. L., & Arbizu, J. (2005). Neuroimaging as a marker of the onset and progression of Alzheimer's disease. *Journal of the Neurological Sciences*, *236*, 55–64.

McHugh, T. J., Blum, K. I., Tsien, J. Z., Tonegawa, S., & Wilson, M. A. (1996). Impaired Hippocampal Representation of Space in CA1-Specific NMDAR1 Knockout Mice. *Cell*, *87*, 1339–1349.

McNaughton, B. L., Battaglia, F. P., Jensen, O., Moser, E. I., & Moser, M.-B. (2006). Path integration and the neural basis of the "cognitive map." *Nature Reviews Neuroscience*, *7*, 663–678.

Mehta, M. R., Barnes, C. A., & McNaughton, B. L. (1997). Experience-dependent, asymmetric expansion of hippocampal place fields. *Proceedings of the National Academy of Sciences*, *94*, 8918–8921.

Mehta, M. R., Quirk, M. C., & Wilson, M. A. (2000). Experience-dependent asymmetric shape of hippocampal receptive fields. *Neuron*, *25*, 707–715.

Mittelstaedt, M.-L., & Mittelstaedt, H. (1980). Homing by path integration in a mammal. *Naturwissenschaften*, *67*, 566–567.

Moffat, S. D., & Resnick, S. M. (2002). Effects of age on virtual environment place navigation and allocentric cognitive mapping. *Behavioral Neuroscience*, *116*, 851–859.

Moffat, S. D., Zonderman, A. B., & Resnick, S. M. (2001). Age differences in spatial memory in a virtual environment navigation task. *Neurobiology of Aging*, *22*, 787–796.

Mokrisova, I., Laczo, J., Andel, R., Gazova, I., Vyhnalek, M., Nedelska, Z., Levcik, D., Cerman, J., … Hort, J. (2016). Real-space path integration is impaired in Alzheimer's disease and mild cognitive impairment. *Behavioural Brain Research*, *307*, 150–158.

Molter, C., & Yamaguchi, Y. (2008). Impact of temporal coding of presynaptic entorhinal cortex grid cells on the formation of hippocampal place fields. *Neural Networks*, *21*, 303–310.

Monaco, J. D., & Abbott, L. F. (2011). Modular realignment of entorhinal grid cell activity as a basis for hippocampal remapping. *The Journal of Neuroscience*, *31*, 9414–9425.

Morris, R. (1984). Developments of a water-maze procedure for studying spatial learning in the rat. *Journal of Neuroscience Methods*, *11*, 47–60.

Moser, E. I., Kropff, E., & Moser, M.-B. (2008). Place Cells, Grid Cells, and the Brain's Spatial Representation System. *Annual Review of Neuroscience*, *31*, 69–89.

Moser, M.-B., Rowland, D. C., & Moser, E. I. (2015). Place Cells, Grid Cells, and Memory. *Cold Spring Harbor Perspectives in Biology*, *7*, a021808.

Mufson, E. J., Malek-Ahmadi, M., Perez, S. E., & Chen, K. (2016). Braak staging, plaque pathology, and APOE status in elderly persons without cognitive impairment. *Neurobiology of Aging*, *37*, 147–153.

Nagel, I. E., Preuschhof, C., Li, S.-C., Nyberg, L., Backman, L., Lindenberger, U., & Heekeren, H. R. (2009). Performance level modulates adult age differences in brain activation during spatial working memory. *Proceedings of the National Academy of Sciences*, *106*, 22552–22557.

Nasreddine, Z. S., Phillips, N. A., Bédirian, V., Charbonneau, S., Whitehead, V., Collin, I., Cummings, J. L., & Chertkow, H. (2005). The Montreal Cognitive Assessment, MoCA: A Brief Screening Tool For Mild Cognitive Impairment. *Journal of the American Geriatrics Society*, *53*, 695–699.

Nau, M., Navarro Schröder, T., Bellmund, J. L. S., & Doeller, C. F. (2018). Hexadirectional coding of visual space in human entorhinal cortex. *Nature Neuroscience*, *21*, 188–190.

Nili, H., Wingfield, C., Walther, A., Su, L., Marslen-Wilson, W., Kriegeskorte, N., Alivisatos, A., Chun, M., … Müller, K. (2014). A Toolbox for Representational Similarity Analysis. *PLoS Computational Biology*, *10*, e1003553.

O'Keefe, J., & Burgess, N. (2005). Dual phase and rate coding in hippocampal place cells: Theoretical significance and relationship to entorhinal grid cells. *Hippocampus*, *15*, 853–866.

O'Keefe, J., & Conway, D. H. (1978). Hippocampal place units in the freely moving rat: Why they fire where they fire. *Experimental Brain Research*, *31*, 573–590.

O'Keefe, J., & Dostrovsky, J. (1971). The hippocampus as a spatial map. Preliminary evidence from unit activity in the freely-moving rat. *Brain Research*, *34*, 171–175.

Oberlin, K. W. (1936). Variation in intensive sensitivity to lifted weights. *Journal of Experimental Psychology*, *19*, 438–455.

Oosterhof, N. N., Connolly, A. C., & Haxby, J. V. (2016). CoSMoMVPA: Multi-Modal Multivariate Pattern Analysis of Neuroimaging Data in Matlab/GNU Octave. *Frontiers in Neuroinformatics*, *10*, 27.

Parron, C., & Save, E. (2004). Evidence for entorhinal and parietal cortices involvement in path integration in the rat. *Experimental Brain Research*, *159*, 349–359.

Pavliotis, G. A. (2014). *Stochastic Processes and Applications: Diffusion Processes, the Fokker-Planck and Langevin Equations.* New York: Springer.

Pengas, G., Hodges, J. R., Watson, P., & Nestor, P. J. (2010). Focal posterior cingulate atrophy in incipient Alzheimer's disease. *Neurobiology of Aging*, *31*, 25–33.

Pennanen, C., Kivipelto, M., Tuomainen, S., Hartikainen, P., Hänninen, T., Laakso, M. P., Hallikainen, M., Vanhanen, M., … Soininen, H. (2004). Hippocampus and entorhinal cortex in mild cognitive impairment and early AD. *Neurobiology of Aging*, *25*, 303–310.

Petzschner, F. H., & Glasauer, S. (2011). Iterative Bayesian Estimation as an Explanation for Range and Regression Effects: A Study on Human Path Integration. *The Journal of Neuroscience*, *31*, 17220–17229.

Petzschner, F. H., Glasauer, S., & Stephan, K. E. (2015). A Bayesian perspective on magnitude estimation. *Trends in Cognitive Sciences*, *19*, 285–293.

Rochefort, C., Lefort, J., & Rondi-Reig, L. (2013). The cerebellum: A new key structure in the navigation system. *Frontiers in Neural Circuits*, *7*, 35.

Rolls, E. T., Stringer, S. M., & Elliot, T. (2006). Entorhinal cortex grid cells can map to hippocampal place cells by competitive learning. *Network*, *17*, 447–465.

Rowland, D. C., Roudi, Y., Moser, M.-B., & Moser, E. I. (2016). Ten Years of Grid Cells. *Annual Review of Neuroscience*, *39*, 19–40.

Sadalla, E. K., & Montello, D. R. (1989). Remembering Changes in Direction. *Environment and Behavior*, *21*, 346–363.

Sargolini, F., Fyhn, M., Hafting, T., McNaughton, B. L., Witter, M. P., Moser, M.-B., & Moser, E. I. (2006). Conjunctive representation of position, direction, and velocity in entorhinal cortex. *Science*, *312*, 758–762.

Savelli, F., & Knierim, J. J. (2010). Hebbian analysis of the transformation of medial entorhinal grid-cell inputs to hippocampal place fields. *Journal of Neurophysiology*, *103*, 3167–3183.

Schimanski, L. A., Lipa, P., & Barnes, C. A. (2013). Tracking the Course of Hippocampal Representations during Learning: When Is the Map Required? *The Journal of Neuroscience*, *33*, 3094–3106.

Schmidt, R. A., Zelaznik, H., Hawkins, B., Frank, J. S., & Quinn, J. T. (1979). Motor-output variability: A theory for the accuracy of rapid motor acts. *Psychological Review*, *47*, 415–451.

Sharp, P. E., Blair, H. T., & Cho, J. (2001). The anatomical and computational basis of the rat head-direction cell signal. *Trends in Neurosciences*, *24*, 289–294.

Shen, J., Barnes, C. A., McNaughton, B. L., Skaggs, W. E., & Weaver, K. L. (1997). The effect of aging on experience-dependent plasticity of hippocampal place cells. *The Journal of Neuroscience*, *17*, 6769–6782.

Sherrill, K. R., Erdem, U. M., Ross, R. S., Brown, T. I., Hasselmo, M. E., & Stern, C. E. (2013). Hippocampus and Retrosplenial Cortex Combine Path Integration Signals for Successful Navigation. *The Journal of Neuroscience*, *33*, 19304–19313.

Shine, J. P., Valdés-Herrera, J. P., Hegarty, M., & Wolbers, T. (2016). The Human Retrosplenial Cortex and Thalamus Code Head Direction in a Global Reference Frame. *The Journal of Neuroscience*, *36*, 6371–6381.

Si, B., & Treves, A. (2009). The role of competitive learning in the generation of DG fields from EC inputs. *Cognitive Neurodynamics*, *3*, 177–187.

Solstad, T., Boccara, C. N., Kropff, E., Moser, M.-B., & Moser, E. I. (2008). Representation of Geometric Borders in the Entorhinal Cortex. *Science*, *322*, 1865–1868.

Solstad, T., Moser, E. I., & Einevoll, G. T. (2006). From grid cells to place cells: A mathematical model. *Hippocampus*, *16*, 1026–1031.

Stackman, R. W., Clark, A. S., & Taube, J. S. (2002). Hippocampal spatial representations require vestibular input. *Hippocampus*, *12*, 291–303.

Stangl, M., Achtzehn, J., Huber, K., Dietrich, C., Tempelmann, C., & Wolbers, T. (2018). Compromised Grid-Cell-like Representations in Old Age as a Key Mechanism to Explain Age-Related Navigational Deficits. *Current Biology*, *28*, 1108–1115.

Stangl, M., Shine, J., & Wolbers, T. (2017). The GridCAT: A Toolbox for Automated Analysis of Human Grid Cell Codes in fMRI. *Frontiers in Neuroinformatics*, *11*, 47.

Stella, F., & Treves, A. (2015). The self-organization of grid cells in 3D. *eLife*, *4*, e05913.

Stensola, H., Stensola, T., Solstad, T., Frøland, K., Moser, M.-B., & Moser, E. I. (2012). The entorhinal grid map is discretized. *Nature*, *492*, 72–78.

Stranahan, A. M., & Mattson, M. P. (2010). Selective vulnerability of neurons in layer II of the entorhinal cortex during aging and Alzheimer's disease. *Neural Plasticity*, *2010*, 108190.

Taube, J. S. (2007). The head direction signal: Origins and sensory-motor integration. *Annual Review of Neuroscience*, *30*, 181–207.

Thompson, L. T., & Best, P. J. (1990). Long-term stability of the place-field activity of single units recorded from the dorsal hippocampus of freely behaving rats. *Brain Research*, *509*, 299–308.

Thrun, S., Burgard, W., & Fox, D. (2005). *Probabilistic Robotics*. Cambridge, MA: MIT Press.

Uhlenbeck, G. E., & Ornstein, L. S. (1930). On the Theory of the Brownian Motion. *Physical Review*, *36*, 823–841.

Ulanovsky, N., & Moss, C. F. (2007). Hippocampal cellular and network activity in freely moving echolocating bats. *Nature Neuroscience*, *10*, 224–233.

United Nations, Department of Economic and Social Affairs, Population Division (2015). *World Population Ageing 2015*. *ST/ESA/SER.A/390*.

Van Cauter, T., Camon, J., Alvernhe, A., Elduayen, C., Sargolini, F., & Save, E. (2013). Distinct Roles of Medial and Lateral Entorhinal Cortex in Spatial Cognition. *Cerebral Cortex*, *23*, 451–459.

Vann, S. D., Aggleton, J. P., & Maguire, E. A. (2009). What does the retrosplenial cortex do? *Nature Reviews Neuroscience*, *10*, 792–802.

Widloski, J., & Fiete, I. (2014). How Does the Brain Solve the Computational Problems of Spatial Navigation? In *Space,Time and Memory in the Hippocampal Formation* (pp. 373–407). Vienna: Springer.

Wiener, J. M., Berthoz, A., & Wolbers, T. (2011). Dissociable cognitive mechanisms underlying human path integration. *Experimental Brain Research*, *208*, 61–71.

Wiener, J. M., Kmecova, H., & de Condappa, O. (2012). Route repetition and route retracing: Effects of cognitive aging. *Frontiers in Aging Neuroscience*, *4*, 7.

Wilkniss, S. M., Jones, M. G., Korol, D. L., Gold, P. E., & Manning, C. A. (1997). Age-related differences in an ecologically based study of route learning. *Psychology and Aging*, *12*, 372–375.

Wilson, I. A., Gallagher, M., Eichenbaum, H., & Tanila, H. (2006). Neurocognitive aging: Prior memories hinder new hippocampal encoding. *Trends in Neurosciences*, *29*, 662–670.

Witter, M. P., Naber, P. A., van Haeften, T., Machielsen, W. C. M., Rombouts, S. A. R. B., Barkhof, F., Scheltens, P., & Lopes da Silva, F. H. (2000). Cortico-hippocampal communication by way of parallel parahippocampal-subicular pathways. *Hippocampus*, *10*, 398–410.

Wolbers, T., Wiener, J. M., Mallot, H. A., & Büchel, C. (2007). Differential Recruitment of the Hippocampus, Medial Prefrontal Cortex, and the Human Motion Complex during Path Integration in Humans. *The Journal of Neuroscience*, *27*, 9408–9416.

Wu, S., Hamaguchi, K., & Amari, S. (2008). Dynamics and Computation of Continuous Attractors. *Neural Computation*, *20*, 994–1025.

Xie, Y., Bigelow, R. T., Frankenthaler, S. F., Studenski, S. A., Moffat, S. D., & Agrawal, Y. (2017). Vestibular Loss in Older Adults Is Associated with Impaired Spatial Navigation: Data from the Triangle Completion Task. *Frontiers in Neurology*, *8*, 173.

Yartsev, M. M., Witter, M. P., & Ulanovsky, N. (2011). Grid cells without theta oscillations in the entorhinal cortex of bats. *Nature*, *479*, 103–107.

Yoder, R. M., & Taube, J. S. (2014). The vestibular contribution to the head direction signal and navigation. *Frontiers in Integrative Neuroscience*, *8*, 32.

Zhang, S.-J., Ye, J., Couey, J. J., Witter, M., Moser, E. I., & Moser, M.-B. (2014). Functional connectivity of the entorhinal-hippocampal space circuit. *Philosophical Transactions of the Royal Society of London B: Biological Sciences*, *369*, 20120516.

Zhong, J. Y., & Moffat, S. D. (2016). Age-Related Differences in Associative Learning of Landmarks and Heading Directions in a Virtual Navigation Task. *Frontiers in Aging Neuroscience*, *8*, 122.

Zilli, E. A. (2012). Models of Grid Cell Spatial Firing Published 2005–2011. *Frontiers in Neural Circuits*, *6*, 16.

APPENDIX

Appendix 1:

The GridCAT Manual

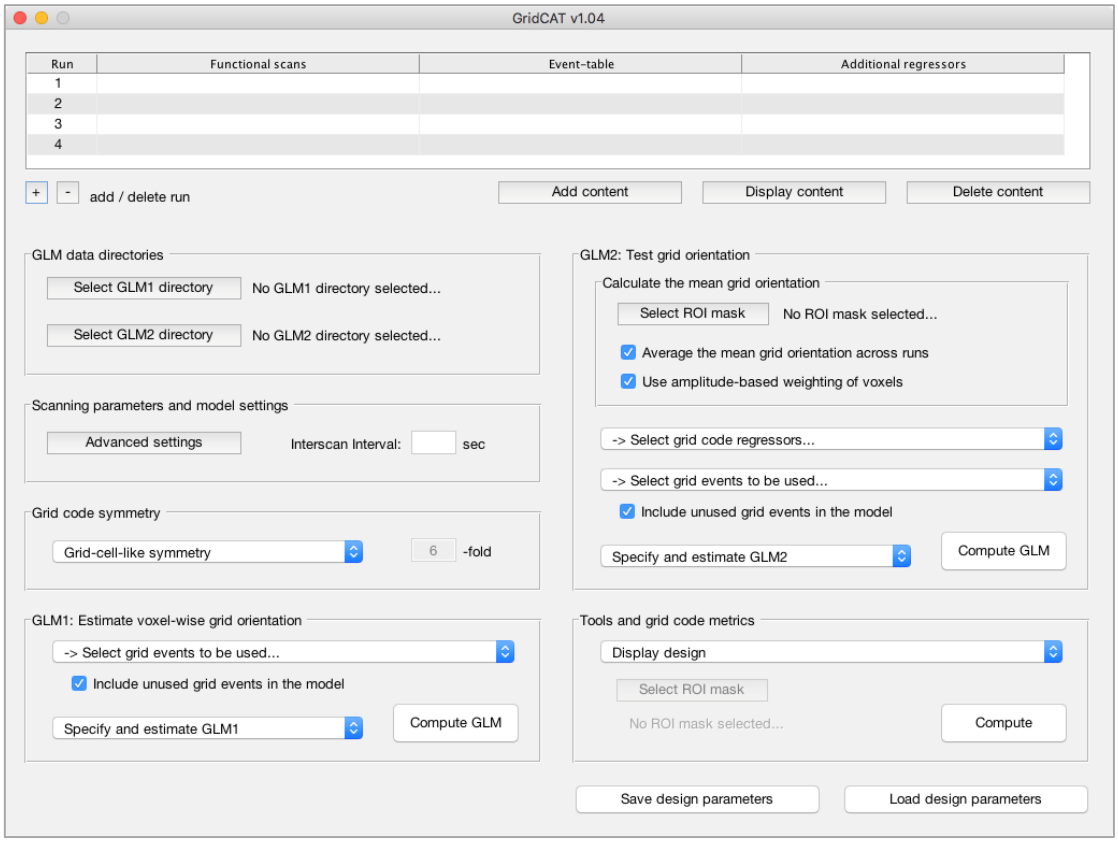

We kindly ask you to cite the GridCAT in your publication, if you have used its graphical user interface or any part of the open-source code for your analysis.

Reference:

Stangl, M.*, Shine, J.*, & Wolbers, T. (2017). The GridCAT: A toolbox for automated analysis of human grid cell codes in fMRI. Frontiers in Neuroinformatics, 11:47. https://doi.org/10.3389/fninf.2017.00047
[* equal contribution]

The GridCAT Manual: Table of Contents

System Requirements 161

Install and start the GridCAT 161

Analyze an example dataset 161

Terminology 162

The raw data table 163

Specify GLM data directories 164

Specify scanning parameters and model settings 165

Specify grid code symmetry 165

Specify and compute GLM1 165

Specify and compute GLM2 167

Tools and grid code metrics 170

Save and load design parameters 175

Using the example script of the GridCAT 175

Appendix 1.1: The GridCAT Selection Dialog 176

Appendix 1.2: The GridCAT event-table 177

Appendix 1.3: Advanced scanning parameters and model settings 179

System Requirements

- The GridCAT runs on Windows, Mac and Linux Systems.
- The GridCAT was extensively tested with MATLAB versions between 2014b and 2016b. We therefore recommend using the GridCAT with these versions, but it might also work fine with newer versions of MATLAB.
- To be correctly displayed, the GridCAT requires a minimum screen resolution of 1050 pixels width and 760 pixels height.
- To run the GridCAT analyses, SPM12 must be installed (i.e., added to your MATLAB path). You can check this by typing “spm fmri” into the MATLAB command window. If SPM does not start, please install SPM12 following the instructions in the SPM manual.

Install and start the GridCAT

1. Download the GridCAT and unzip the downloaded file.
2. Move the GridCAT directory to a permanent location on your local hard drive.
3. Start MATLAB and change to the GridCAT directory within MATLAB.
4. Type “install_GridCAT” into the MATLAB command window (this will permanently add the GridCAT to your MATLAB path).
5. To start the GridCAT from now on, open MATLAB and type “gridcat” into the command window.

Analyze an example dataset

In order to test the functionality of the GridCAT, you can run a complete grid code analysis and try out different analysis methods on an example dataset that we have provided.
In this manual, we highlight in blue italic text all steps that are necessary to analyze the example dataset and reproduce the results presented in the paper.
Before you can start analyzing the example dataset, you must download it, unzip the downloaded file and save the unzipped data to your hard drive. The saving location on your hard drive will be henceforth referred to as

`[exampleDatasetDirectory]`

Terminology

- **GLM1, GLM2:**
  The GridCAT analyses are carried out using a two-step approach. In the first step, grid orientations are estimated, and in the second step the estimated grid orientations are tested. We use the term “GLM1” for the first general linear model that is carried out to estimate voxel-wise grid orientations, and the term “GLM2” is used for the second general linear model that tests the estimated grid orientations.

- **Event:**
  The term “event” is used for anything happening during the fMRI scanning runs that you want to include in your GLM to explain changes in the blood oxygenation level dependent (BOLD) response. Every single event is specified by a name, an onset, and duration. For example, a typical event during an fMRI run could be the presentation of a fixation cross, beginning at a certain time after the start of the scanning run (onset) and staying on the screen for a specific period of time (duration).

- **Grid event:**
  We use the term “grid event” for events that have also an event-angle (i.e. directional information that is used to determine the grid orientation, quantify the magnitude of grid code response, etc.). For example, in a paradigm requiring subjects to navigate a virtual environment (e.g., like a 3D computer game) while they are in the scanner, a grid event might comprise a movement within the virtual environment that begins at a particular onset, lasts for a certain duration, and the movement is made in a specific direction (event-angle) in the virtual world.

- **Grid event type:**
  During an experiment, there will usually be multiple repetitions of the same event type (e.g., multiple “translation” events that have different onsets, durations, and event-angles). However, a researcher may also want to compare different types of grid events, for example “active translation” and “passive translation”, denoting trials in which the participant moved through the virtual environment using a joystick versus those where they viewed a video of the movement. To investigate grid code metrics for each “grid event type” separately, the user can specify multiple grid event types (e.g., active and passive), and label each grid event accordingly.

The raw data table

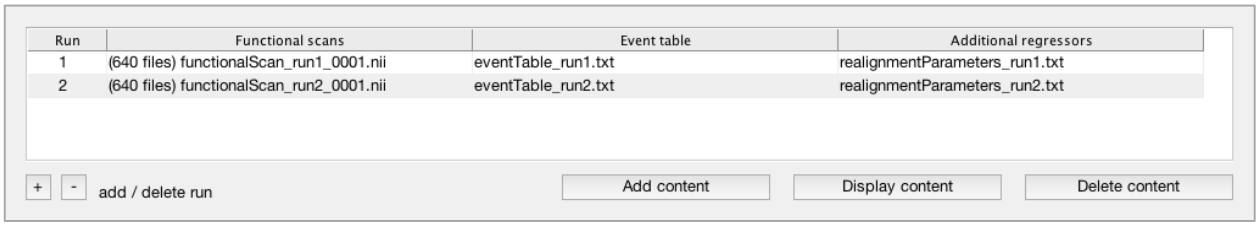

1. Specify the number of separate fMRI scanning runs by pressing the +/- buttons in the bottom left corner of the table.
   In the example dataset, we have 2 separate runs.

2. For each run, specify functional scans, an event-table, and (optionally) an additional regressor file, by assigning data to the table's cells (these steps are described in detail below). In order to assign data to one or multiple specific cell(s), select the cell(s) you want and then press the "Add content" button. To select data for all empty cells of the table, just click on the "Add content" button when no cell is selected. Data selection works with the "GridCAT Selection Dialog" (this is mostly self-explanatory, but its functionality is explained in more detail in Appendix 1.1 of this manual).
   If you want to double-check the data you have assigned to one or multiple cell(s), select the cell(s) you want and click on the "Display content" button. Also, you can delete cell content by selecting cells and clicking on the "Delete content" button.

   a. Functional scans are a set of 3D images for each scanning run. We recommend using files in the .nii format. Select all files of a particular run. After selection, the number of selected files and the name of the first image is shown in the table.
      For the example dataset, in order to specify functional scans for run 1, select all functional scans
      `functionalScan_run1_0001.nii,`
      `functionalScan_run1_0002.nii,`
      `…`
      from the folder
      `[exampleDatasetDirectory]/FunctionalScans/run1/`
      and do the same for run 2. After you have selected the files, the table should now show the number of selected functional scans and the name of the first scan. The example dataset consists of 640 files for each run.

   b. The event-table is the textfile (.txt) that contains all the information about the individual events within an fMRI scanning run. Detailed information about the specific format of an event-table as well as additional options and examples can be found in Appendix 1.2 of this manual. Briefly, the event-table must be a textfile (*.txt) in which each line defines one event. Each event comprises multiple columns, which can be delimited either by a semicolon, a comma, or a tabstopp. For each event, column 1 defines the event-name, column 2 defines the event-onset in seconds (relative to the start of the scanning run), and column 3 defines the event duration in seconds. In addition, grid events have a 4th column in which the event-angle is defined (0 – 359 degrees).

To specify the event-table for run 1 or 2 of the example dataset, select the appropriate textfile

`eventTable_run1.txt`, or
`eventTable_run2.txt`

from the folder

`[exampleDatasetDirectory]/EventTables/`

c. Optionally, you can load a file for each run containing additional regressors that you want to add to the GLM. This file can be a textfile (.txt), in which the number of lines corresponds to the number of functional scans, and each column containing a different regressor. For example, SPM automatically creates a textfile containing the realignment parameters resulting from the realignment of your functional images. These textfiles can be used directly as additional regressor files. Alternatively, you can specify a MATLAB file (*.mat) containing a matrix named R, which contains the corresponding values per line and column.
For the example dataset, we provide realignment parameters that were generated automatically by SPM during data preprocessing. To specify additional regressors for run 1 or 2 of the example dataset, select the appropriate textfile

`realignmentParameters_run1.txt`, or
`realignmentParameters_run2.txt`

from the folder

`[exampleDatasetDirectory]/AdditionalRegressors/`

They each contain 6 columns corresponding to the 6 movement dimensions (X/Y/Z direction and yaw/pitch/roll).

Specify GLM data directories

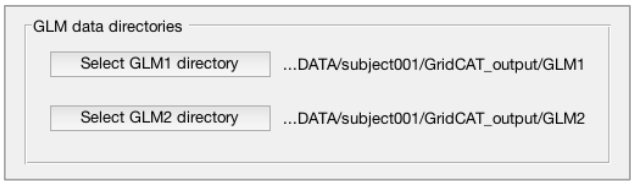

Two different directories for GLM1 and GLM2 need to be selected, which will store all the data produced by the GridCAT. We recommend that you create new directories for GLM1 and GLM2, which do not contain any other data.
After specifying a data directory, you can double-check its full path by clicking on the textbox next to the button.
For the example dataset, you can create a directory

`[exampleDatasetDirectory]/GridCAT_data/GLM1/`

and select it as GLM1 data directory, and repeat this for GLM2.

Specify scanning parameters and model settings

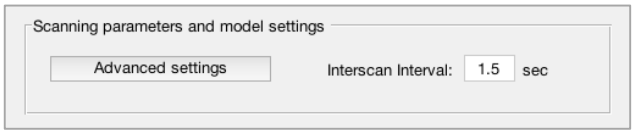

1. Specify the Interscan-Interval (TR) in seconds, which is the time between acquiring a plane of one volume and the same plane in the next volume.
   For the example dataset, the data was acquired with an interscan-interval of 1.5 seconds.

2. You can also change advanced scanning parameters and model settings (microtime-resolution, microtime-onset, high-pass-filter, and the addition of time and dispersion HRF derivatives), used by SPM during the fitting of the GLM. In many cases, it won't be necessary to change the default settings. However, if you want to change these parameters, you can find more information about them in Appendix 1.3 of this manual.
   In order to reproduce the presented results for the example dataset, do not change the advanced scanning parameters and model settings.

Specify grid code symmetry

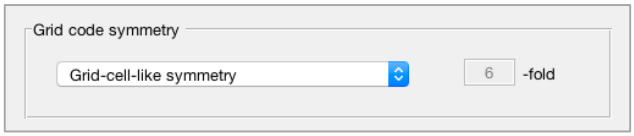

For standard analyses, specify that you want to check for "Grid-cell-like symmetry" (6-fold), since grid-cell-like representations are expected to show a 6-fold symmetrical pattern. However, other symmetry values can be used to carry out control analyses in order to show that effects are strongest for the 6-fold but not other (e.g. 4,5,7,8)-fold symmetries.
The results presented for the example dataset are generated by running separate analyses with the GridCAT checking for 4/5/6/7/8-fold symmetry, respectively.

Specify and compute GLM1

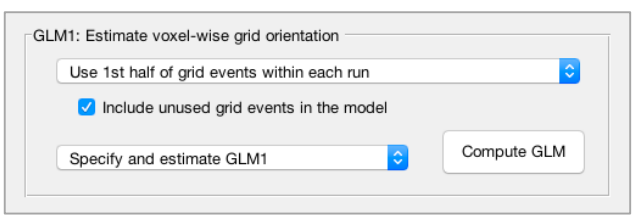

1. Here, you specify which events should be used to calculate GLM1. It is necessary to partition your dataset into two: one to estimate the voxel-wise grid orientation (GLM1) and a separate one to test the estimated orientations (GLM2). Thus, if you select the first half of grid events per run to estimate grid orientations in GLM1, you would usually select the second half of grid events per run for use in GLM2. When choosing the events for GLM1, the GridCAT will automatically set the unused grid events in GLM1 as the events to be used for testing the estimated grid orientation in GLM2. However, you can change this later when you specify settings for GLM2.
   In order to reproduce the presented results for the example dataset, select to use the first half of grid events per run for GLM1.

2. Specify whether you want to keep unused grid events in the model or not. For example, if you have selected only the first half of grid events per run for GLM1, the second half of grid events per run can either be completely excluded from GLM1, or they can be included without their corresponding event-angles (meaning that these events will not contribute to the estimation of grid orientations).
   In order to reproduce the presented results for the example dataset, select to keep unused events in the model.

3. Specify and estimate GLM1. During GLM1 specification, the GridCAT generates and displays a design matrix and saves all model specifications in the GLM1 data directory. During the estimation process, the parameter estimates (beta images) are generated for every regressor, including the two grid event regressors (β_{sin} and β_{cos}) that parametrically model grid events using sin(α_t*6) and cos(α_t*6) with respect to their grid event angle α_t. Furthermore, images containing the estimated voxel-wise grid orientations are generated. You can select to carry out both specification and estimation together, or separately.

4. Press “Compute GLM” to start the calculation process for GLM1. The GridCAT starts with all the GLM1 calculations, which will take a while. Parameter estimates for each regressor are calculated and voxel-wise grid orientations are estimated. Moreover, an indicator for the strength of the grid-like activation (which might be interpreted as the “firing-amplitude”) is also calculated by $\sqrt{\beta_{sin}{}^2 + \beta_{cos}{}^2}$ using the parameter estimates of the two grid event regressors (β_{sin} and β_{cos}).
   After all the GLM1 calculations have finished, the newly generated data (e.g. beta-images for all regressors, voxel-wise grid orientation images, etc.) are stored in the GLM1 data directory.
   To estimate voxel-wise grid orientations in the example dataset, compute GLM1 (specification & estimation) now.

Specify and compute GLM2

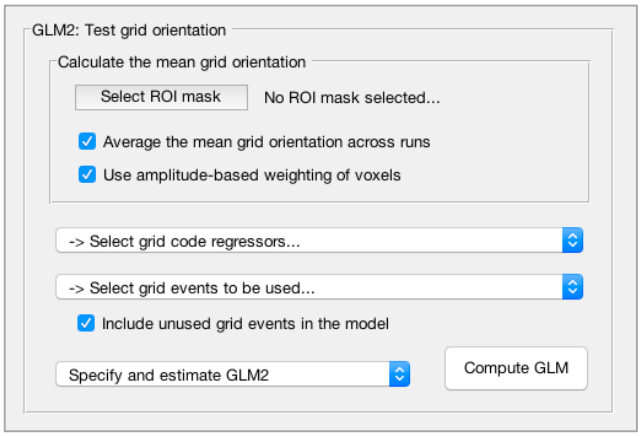

1. After estimating voxel-wise grid orientations using GLM1, you may want to test the estimated orientations in GLM2. For this purpose, you have to define a region of interest (ROI) within the brain that you want to use to calculate a mean grid orientation across multiple voxels. For example, if you want to calculate the mean grid orientation within an anatomical region like the entorhinal cortex, you need to specify an ROI mask, which contains the information about where the entorhinal cortex is located in this particular subject. It is necessary, therefore, to specify a ROI mask image, which is aligned/coregistered with your functional scans, and contains binary information about your ROI (i.e., all voxels containing "1" belong to your ROI, all voxels containing "0" do not belong to your ROI).
   After specifying a ROI mask image, you can double-check its full path by clicking on the textbox next to the button.
   With the example dataset, we provide ROI mask images for the entorhinal cortex (both right and left hemisphere) of our example participant. These ROI masks have been created by manually delineating the entorhinal cortex on an anatomical image using ITK-SNAP (http://www.itksnap.org). Select one of these ROI masks
   `ROImask_entorhinalCortex_LH.nii`, or
   `ROImask_entorhinalCortex_RH.nii`
   from the directory
   `[exampleDatasetDirectory]/ROI_masks/`
   to reproduce the presented results.

2. In GLM1, the voxel-wise grid orientation is estimated for each run individually. However, when testing the estimated grid orientation in GLM2, you can use either individual mean grid orientations per run, or a mean grid orientation averaged across all runs. In experiments where you would expect different grid orientations for individual runs, we recommend not averaging the grid orientation across runs.
   In the example dataset, we have no reason to assume that the mean grid orientation would change between runs, so we can choose to average the mean grid orientation across runs.

3. When calculating the mean grid orientation across all voxels within the ROI, it is possible to use the indicator of "firing-amplitude" (i.e., a measure of grid-like activation that has been calculated during GLM1 computations) per voxel. Selecting this option, the GridCAT assigns different weights to individual voxels, depending on the voxel's "firing-amplitude". If you do not select this option, all voxels are weighted equally.

In order to reproduce the presented results for the example dataset, select amplitude-based weighting of voxels.

4. There are several ways to include regressors for grid events in GLM2.
   In order to reproduce the presented results for the example dataset, select either a parametric modulation regressor or aligned / misaligned regressors (1 each). Including multiple aligned / misaligned regressors does not seem to be reasonable here, as the number of grid events in our example dataset is quite small for this kind of analysis. This analysis would be more appropriate with a larger number of grid events or if results are averaged across multiple participants.

   a. Parametric modulation regressor: Grid events can be modelled using parametric modulation that serves as a measure of alignment between the mean grid orientation and the event-angle of an individual event. One grid event regressor and the corresponding parametric modulation value (ranging from -1 to 1) will be included in the GLM2.

   b. Aligned/misaligned regressors (1 each): Grid events can be assigned either to a regressor for “aligned” or for “misaligned” events. An event is assigned to the “aligned” regressor if its event-angle lies within +/- 15 degrees of the mean grid orientation (or a 60 degree multiple of this value), or otherwise to the “misaligned” regressor.

   c. Aligned/misaligned regressors (multiple): Based on our model’s assumptions of grid-cell-like symmetry, we expect higher peaks in signal amplitude for an event if the offset between its event-angle and the mean grid orientation is 0 or a multiple of 60 degrees (i.e., 0/60/120/180/240/300 degrees), or lower peaks for an offset of 30 degrees plus a multiple of 60 degrees (i.e., 30/90/150/210/270/330 degrees). Analogous peaks would be expected when testing for other symmetry values (e.g. for 4-fold symmetry, higher peaks are expected with 0/90/180/270 offset, and lower peaks are expected with 45/135/225/315 degrees).
      When using this option, multiple regressors, one for each orientation for which a signal peak (high or low) is expected, will be added to the model, and each grid event will be assigned to the appropriate regressor.

5. Specify, which events should be used to calculate GLM2. Usually, you would use the other half of the data that has not been used in GLM1 to estimate voxel-wise grid orientations. For example, if you have used the first half of grid events per run to estimate grid orientations in GLM1, you would now select to use the second half of grid events per run for GLM2.
   In order to reproduce the presented results for the example dataset, select the second half of grid events per run.

6. Specify whether you want to keep unused grid events in the model or not.
   In order to reproduce the presented results for the example dataset, select to keep unused events in the model.

7. Specify and/or estimate GLM2 (this will generate and visualize the design matrix, save all model specifications, generate parameter estimates for each regressor, etc.).
   To test the estimated grid orientations in the example dataset, compute GLM2 (specification & estimation) now.

   The GridCAT automatically creates a default set of contrasts between regressors, which can be used to derive grid code metrics such as the magnitude of grid code response. How these contrasts are created mathematically depends on how you have selected to model grid events in GLM2 (using a parametric modulation, or one aligned/misaligned regressor each, or multiple aligned/misaligned regressors):

   a. If grid events are modelled using parametric modulation:
      t-contrasts for single runs are created by multiplying the parameter estimates for a grid event type's parametric modulation regressor by 1, whereas all other regressors' parameter estimates are multiplied by 0. Furthermore, if the same grid event type is present in multiple runs, a combined t-contrast across all of these runs is created by multiplying the grid event type's parameter estimates of each run by 1, whereas all other regressors' parameter estimates are multiplied by 0.

   b. If grid events are modelled using one regressor each for "aligned" and "misaligned" events:
      t-contrasts for single runs are created by multiplying the parameter estimates for the "aligned" grid event regressor by 1, whereas the parameter estimates for the "misaligned" grid event regressor is multiplied by -1 and all other regressors' parameter estimates are multiplied by 0. Furthermore, if the same grid event type is present in multiple runs, combined t-contrasts across all of these runs are created by multiplying the grid event type's parameter estimates for the "aligned" regressors of each run by 1, whereas the "misaligned" regressors' parameter estimates are multiplied with -1; all other regressors' parameter estimates are multiplied by 0.

   c. If grid events are modelled using multiple "aligned" and "misaligned" regressors:
      A separate t-contrast is created for each individual orientation at which a signal peak is expected. For example, based on our assumption of grid-cell-like (6-fold) symmetry, higher signal peaks are expected for 0/60/120/180/240/300 degrees and lower peaks for 30/90/150/210/270/330 degree offset between an event-angle and the mean grid orientation. Each t-contrast is created by multiplying the parameter estimates for a specific peak-orientation by 1, whereas all other regressors' parameter estimates are multiplied by 0. Again, if the same grid event type is present in multiple runs, a combined t-contrast across all of these runs is created for each peak-orientation by multiplying a peak-orientation's parameter estimates of each run by 1, whereas all other regressors' parameter estimates are multiplied by 0.

Tools and grid code metrics

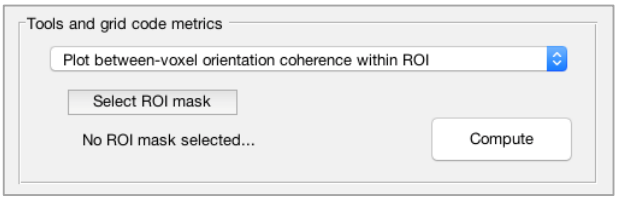

1. The GridCAT offers a set of tools and grid code metrics that generate and help visualize data and results. As these tools access data from the GLM data directories, it is necessary to have specified data directories for GLM1 and GLM2, respectively. Moreover, some tools require you select one or multiple ROI mask(s) for which output is generated or visualized. After specifying one or multiple ROI mask(s), you can double-check their full path by clicking on the textbox next to the button.

    a. Display design
    This tool accesses data from the GLM1 and GLM2 data directories, and allows you to review a model design by showing the design matrix generated by SPM when GLM1 or GLM2 is specified.

    b. Plot between-voxel orientation coherence within ROI
    This tool allows you to visualize the coherence of voxel-wise grid orientations within an ROI. It therefore uses voxel-wise grid orientation data from the GLM1 data directory. In the course of GLM1 calculations, the GridCAT has created images containing voxel-wise grid orientations for each grid event type and run, respectively, and saved them in the GLM1 data directory (named 'voxelwiseOri_*eventName_runNr*_deg.nii'). In order to plot the coherence of voxel-wise grid orientations within an ROI for a specific grid event type and scanning run, specify your ROI mask image, and select the corresponding voxel-wise grid orientation image you are interested in. Selecting multiple ROI mask and/or multiple voxel-wise grid orientation images at the same time is possible, and will lead to separate independent plots for each image and ROI, respectively. The resulting polar histogram plots display the coherence of the grid orientation between voxels in the selected ROIs. The length of each bar indicates the number of voxels that share a similar grid orientation, and the numbers next to the rings indicate the number of voxels represented by each ring of the polar plot. Moreover, the plot displays the number of voxels within the ROI as well as the number of NaN ("not-a-number") voxels, for which a grid orientation could not be estimated. By changing the plot settings and pressing the "Redraw" button, a number of additional features can be added: The mean grid orientation across all voxels can be visualized by arrows (with and/or without using amplitude-based weighting of individual voxels). Furthermore, Rayleigh's test for non-uniformity of the voxel-wise grid orientations within the ROI can be computed, which serves as a measure of between-voxel orientation coherence. The Rayleigh test is carried out using the CircStat 2012a toolbox (https://philippberens.wordpress.com/code/circstats/). Voxel-wise grid orientations within the ROI can be exported, to enable the user to carry out further analyses and/or statistical tests on these data, depending on the specific research question of interest (such as testing for systematic changes of grid orientations between conditions, or applying corrections for smoothness of the data, etc.).

In order to plot between-voxel orientation coherence in the left and right entorhinal cortex for the example dataset, select one or both of these ROI masks

`ROImask_entorhinalCortex_LH.nii`, *and/or*
`ROImask_entorhinalCortex_RH.nii`

from the directory

`[exampleDatasetDirectory]/ROI_masks/`

and select one or multiple of the images containing voxel-wise grid orientations in the GLM1 data directory, e.g.:

`voxelwiseGridOri_translation_run1_deg.nii`

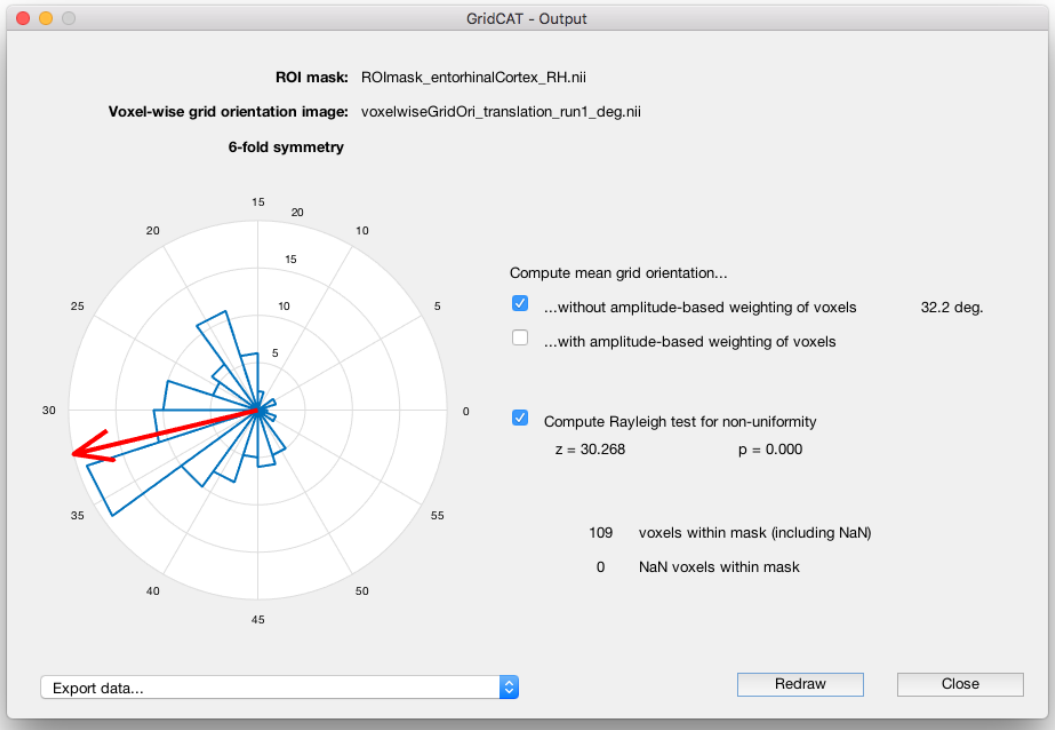

c. Plot within-voxel orientation coherence within ROI
This tool allows you to visualize the voxel-wise coherence of grid orientations between two different conditions within an ROI. For example, different conditions could be two different runs, or two different grid event types. This tool accesses voxel-wise grid orientation data from the GLM1 data directory. Specify your ROI masks, and select two images containing voxel-wise grid orientations that you want to compare (i.e., select one or multiple images for different grid event types and runs, respectively). The tool will visualize and calculate the proportion of stable voxels between the two images within all voxels of the ROI. The two black rings in each plot represent the two different conditions, and each voxel's grid orientation is indicated with a circular marker; a line connects the orientations of each voxel. Whether a voxel's orientation is deemed "stable" depends on whether its estimated orientation differs by more than a given threshold, which is initially set to +/- 15 degrees for 6-fold symmetry analysis (analogous for other symmetry values). This threshold, however, as well as the visual appearance of the plot can be changed manually by adapting the settings in the plot and pressing the "Redraw" button.

Independent calculations are performed for each ROI mask image that you have selected.

In order to plot within-voxel orientation coherence in the left and/or right entorhinal cortex between run 1 and run 2 for the example participant, select one or both of these ROI masks

`ROImask_entorhinalCortex_LH.nii`, *and/or*
`ROImask_entorhinalCortex_RH.nii`

from the directory

`[exampleDatasetDirectory]/ROI_masks/`

and select the following images containing voxel-wise grid orientations in the GLM1 data directory:

`voxelwiseGridOri_translation_run1_deg.nii`, *and*
`voxelwiseGridOri_translation_run2_deg.nii`

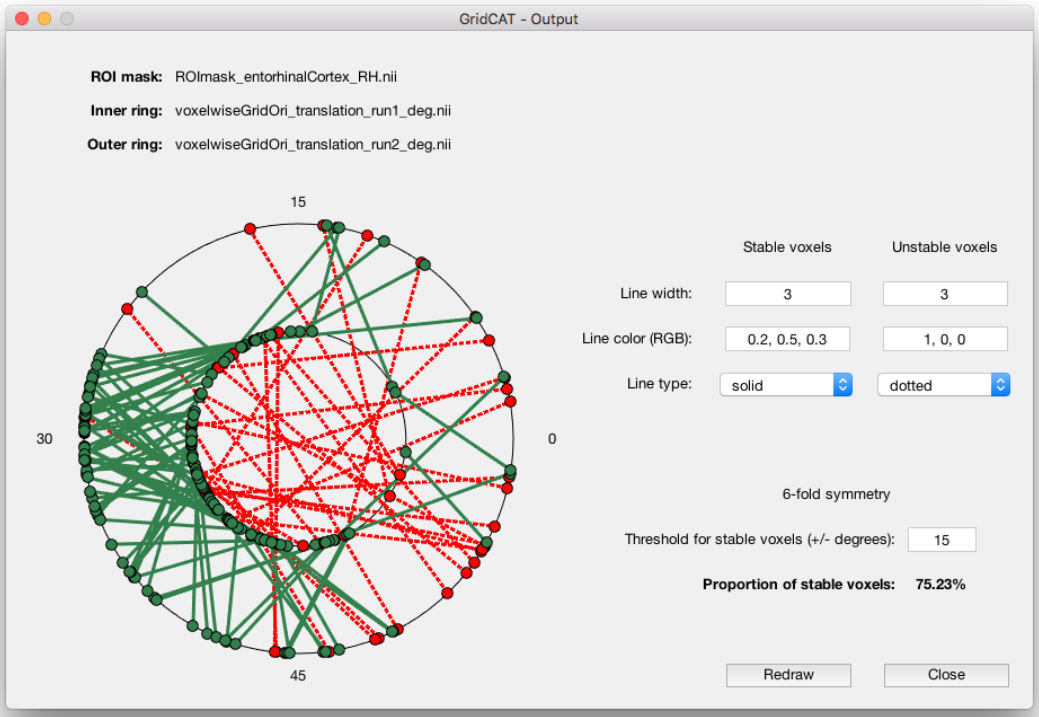

d. Output mean grid orientation within ROI

Using this tool, you can output the mean grid orientation within an ROI. It therefore accesses voxel-wise grid orientation data from the specified GLM1 data directory and calculates the mean grid orientation across all voxels within the specified ROI mask(s). As the mean grid orientation can be calculated either with or without using different weightings for individual voxels (i.e., “amplitude-based” weighting), this tool outputs the mean grid orientation for both options. Independent calculations are performed for each ROI mask image that you have selected.

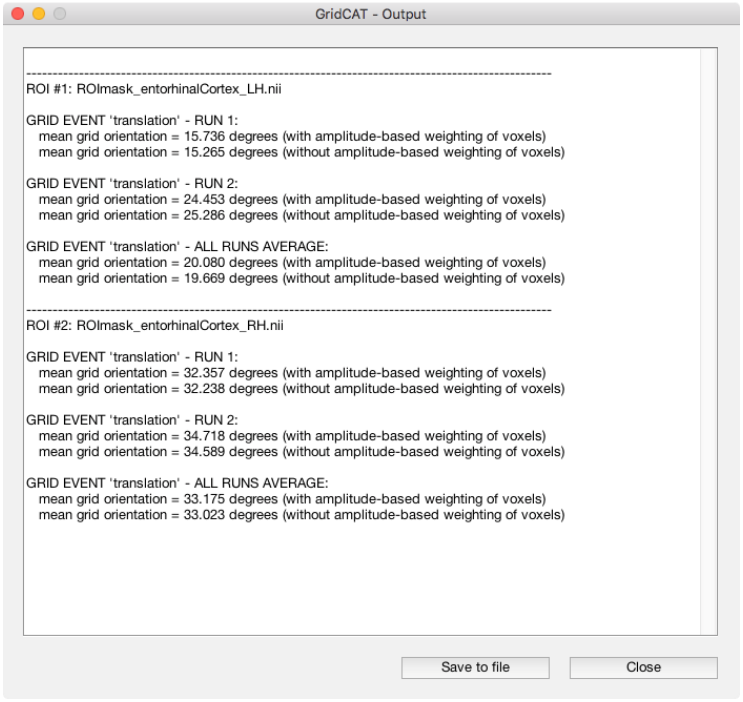

e. Create custom contrasts between GLM2 regressors
If you want to generate results for contrasts that are not specified in the default set of contrasts created by the GridCAT, you can specify additional t-contrasts with this tool by combining individual regressors. This tool accesses data from the GLM2 data directory. In order to create a new t-contrast, just assign a value to any GLM2 regressor you want (which will be used as the multiplication factor for this regressor's parameter estimates), specify a contrast name and press the "OK" button. Parameter estimates of regressors, for which you do not specify a multiplication value, will be multiplied with 0.

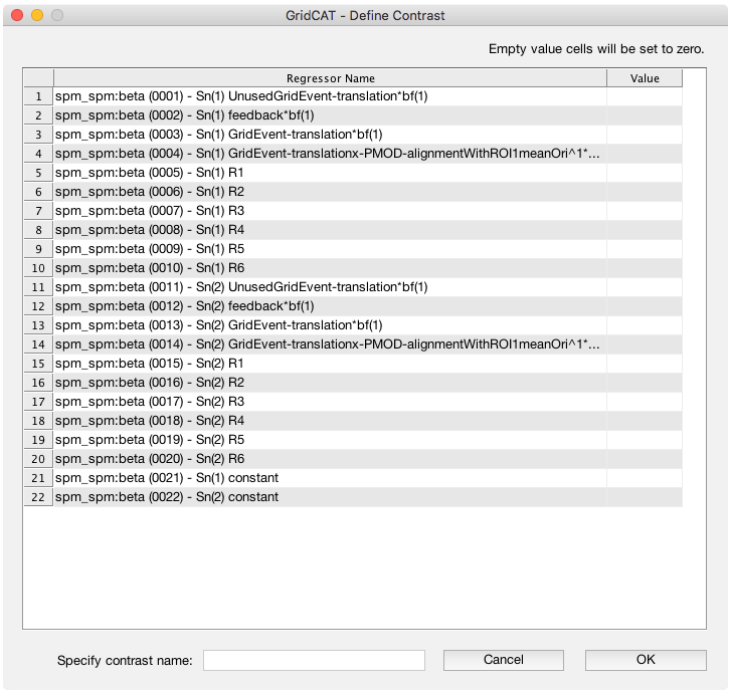

f. Output magnitude of grid code response within ROI
This tool allows you to calculate the magnitude of grid code response in one or multiple ROIs that you have specified by pressing the “Select ROI mask” button. The magnitude of the grid code response can be shown for contrasts that have been specified automatically by the GridCAT (the default set of contrasts) or for additional contrasts between GLM2 regressors that you have created. Here, you need to select the contrasts you want to interrogate and the GridCAT will display the average magnitude of grid code response within each ROI separately for each selected contrast. To generate this grid code metric, this tool accesses data from the GLM2 data directory.

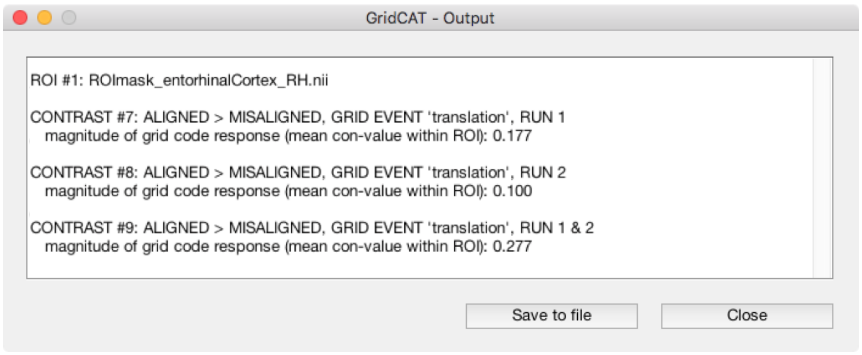

g. Export all grid code metrics
This tool allows you to export a comprehensive list of all grid code metrics that can be calculated based on a given dataset, for example to allow statistical analysis across participants. Therefore, it accesses the specified GLM1 and GLM2 data directories and also requires you select specific ROI masks in which the grid code metrics are calculated.

In order to export all grid code metrics for the example dataset, select both ROI masks
`ROImask_entorhinalCortex_LH.nii`, and
`ROImask_entorhinalCortex_RH.nii`
from the directory
`[exampleDatasetDirectory]/ROI_masks/`
and specify a location on your local hard drive where all the output will be saved.

All output is saved to a textfile, which is formatted in delimited text using a semicolon delimiter. Consequently, the output data can be used with a program of your choice, for example in order to carry out further analysis and statistical tests on the calculated grid metrics, depending on your specific research question. For that purpose, import the textfile into a program that is able to convert (semicolon-)delimited text to separate cells of data, such as Microsoft Excel, SPSS, or others.
The output file includes the following grid code metrics for all specified ROI masks and separately for every grid event type:

- Magnitude of grid code response: This grid code metric is calculated for every contrast specified in the GLM2 data directory (i.e., the default set of contrasts as well as those additionally created by the user).

- Between-voxel orientation coherence within ROI: This grid code metric is calculated for each run individually as well as for the average across all runs. Rayleigh z- and p-values are reported.
- Within-voxel orientation coherence within ROI: This grid code metric is calculated and the proportion of stable voxels is reported between every possible pair of voxel-wise grid orientation images (i.e. all pairs of runs and grid event types, respectively).
- Mean grid orientation within ROI: This grid code metric is calculated for all specified ROI images, for all runs and grid event types separately. The resulting mean grid orientation is reported for both calculation methods (i.e., with and without amplitude-based weighting of voxels).

Save and load design parameters

The GridCAT enables you to save all design parameters (i.e., all changes and settings you have made using the GridCAT's graphical user interface), in order to load them again later. All information is stored in a MATLAB file (*.mat) on your local hard drive. Simply press the "Save design parameters" button and select a location to store the file. Furthermore, whenever you compute a GLM1 or GLM2, the design parameters are automatically stored in the GLM1/GLM2 data directory (named "GridCAT_GLM1.mat", with the same naming convention for GLM2). This option allows you to restore and inspect the settings you have used when computing a GLM.
In order to restore design parameters, press the "Load design parameters" button and select the mat-File containing the relevant design parameters.

Using the example script of the GridCAT

For those who prefer to use and modify the open-source MATLAB code of the GridCAT, rather than the GUI, we provide an example script, which includes all steps of a common grid code analysis pipeline. Detailed comments in the script will guide the user through necessary settings and functions in the code. The example script can be found in:
`DEMO_GridCAT_Script.m`

Appendix 1.1: The GridCAT Selection Dialog

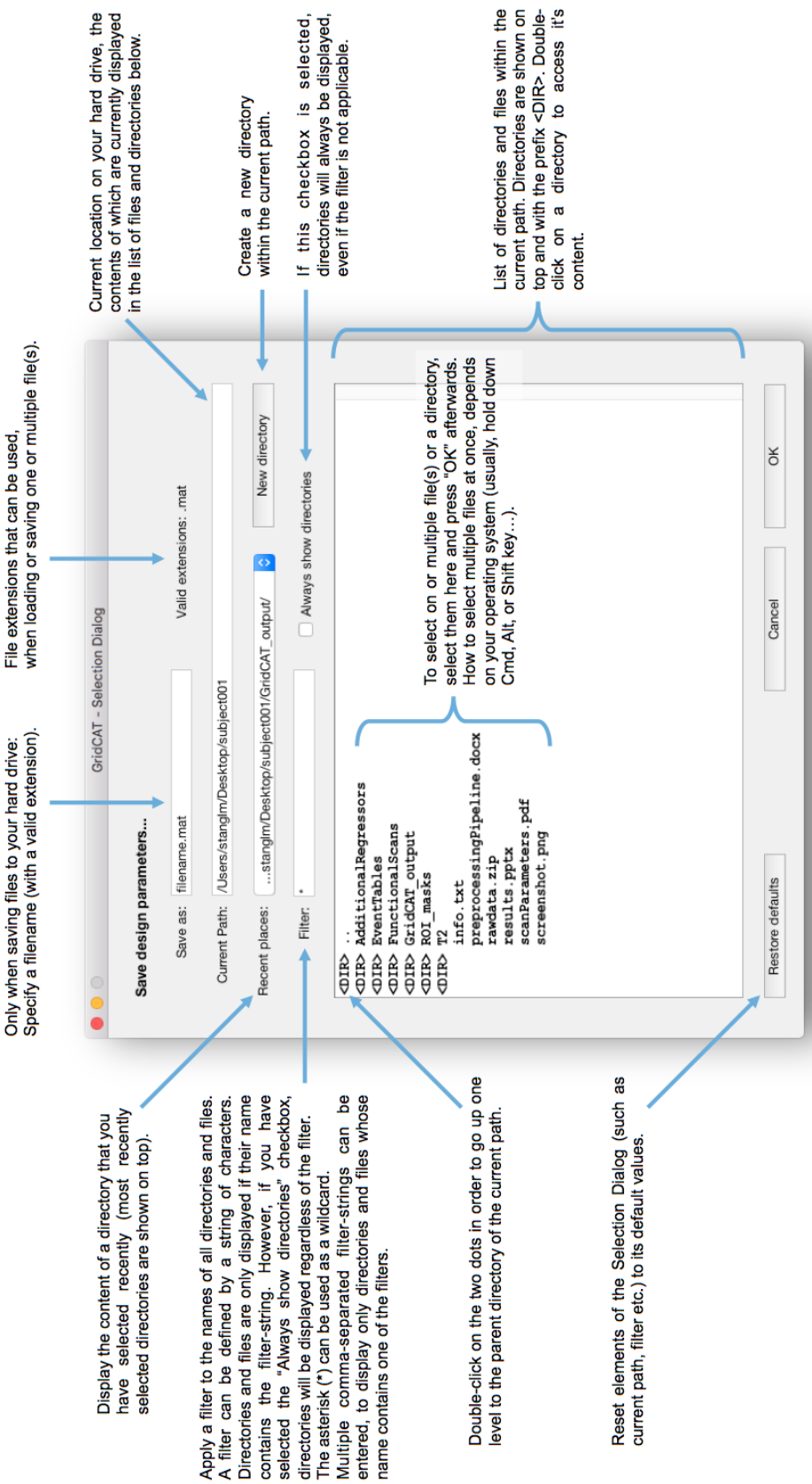

Appendix 1.2: The GridCAT event-table

An event-table is a textfile (*.txt) for each fMRI scanning run, which contains all information about single events during this run. Each line in the event-table defines a single event using the following format:

name	onset	duration

In addition to the three columns per event as shown above, a grid event also has a 4th column defining its event-angle:

name	onset	duration	angle

The following example shows an event-table from a navigation paradigm, in which the subject navigated a virtual environment (like in a 3D computer game). The experimental paradigm allowed the user to perform translational and rotational movements within the environment, as well as to stand still on the spot. In this event-table, translational movements are used as grid events.

stand	0	3.5	
translate	3.5	4	225
rotate	7.5	2.25	
translate	9.75	3.2	192.3
rotate	12.95	2	
translate	14.95	7.05	4.5
stand	22	3.73	
.	.	.	.
.	.	.	.
.	.	.	.

In GLM1 and GLM2, the GridCAT puts all events that are within an event-table and have the same name into one regressor. This is true for normal events as well as for grid events. Consequently, if you want to distinguish between different grid event types within a run, simply use different names for these events. The following example shows an event-table similar to the one above, but now the paradigm includes both active translations (“activeTransl”) and passive translations (“passiveTransl”), which should be used as two different types of grid event (i.e. entered as different regressors) in GLM1 and GLM2.

stand	0	2.2	
rotate	2.2	3	
activeTransl	5.2	4.5	359
stand	9.7	3	
activeTransl	12.7	1.3	359
rotate	14	2.5	
passiveTransl	16.5	5	7.5
rotate	21.5	4.5	
passiveTransl	26	2.3	24
activeTransl	28.3	10.2	24
.	.	.	.
.	.	.	.
.	.	.	.

The GridCAT offers several different ways to partition your grid events for GLM1 and GLM2. However, you may wish to specify yourself which events to include in GLM1 and/or GLM2. To do this, you can add two more columns to an event-table that specify whether a grid event is used in GLM1 (column 5) and/or GLM2 (column 6). If column 5 is set to “1” then this event will be used as a grid event in GLM1. Set column 5 to “0” if you do not want to use this event as a grid event in GLM1; the same method is used for GLM2 in column 6.
The following example shows the content of an event-table in which there are only “translation” and “rotation” events. Translations are used as grid events (i.e., they also have an event-angle) and the event-table also specifies which grid events to use in GLM1 and GLM2.

stand	0	2			
translation	4.3	5.3	22	1	0
stand	9.9	3			
translation	16	2.1	173	1	0
translation	22.4	5	249.4	0	1
translation	28	2	156	0	1
stand	33.91	2.2			
translation	38	9	97	1	0
translation	52.3	0.7	359	1	0
stand	55.2	3.7			
translation	59.1	8	16.34	0	0
stand	72	2			
translation	74.2	1.3	1.7	0	0
translation	75.5	5	1.7	1	1
translation	86	3.2	39	1	1
stand	91.5	8			
translation	107.3	0.72	100	0	1
translation	109	4.6	66.74	1	0
.	.	.	.	.	.
.	.	.	.	.	.
.	.	.	.	.	.

The GridCAT accepts tabstopps, semicolons, and commas as delimiters between columns. Consequently, the three following examples of event-tables all have an appropriate format and an identical content:

stand	0	3.5	
translate	3.5	4	225
rotate	7.5	2.2	
translate	9.7	3.2	192
rotate	12.9	2	
translate	14.9	7.1	4
stand	22	3	

(tabstopp-delimited)

=

```
stand;0;3.5
translate;3.5;4;225
rotate;7.5;2.2
translate;9.7;3.2;192
rotate;12.9;2
translate;14.9;7.1;4
stand;22;3
```

(semicolon-delimited)

=

```
stand,0,3.5
translate,3.5,4,225
rotate,7.5,2.2
translate,9.7,3.2,192
rotate,12.9,2
translate,14.9,7.1,4
stand,22,3
```

(comma-delimited)

Appendix 1.3: Advanced scanning parameters and model settings

The following information provides only an overview of the advanced model settings that are used by SPM12 and can be adapted in the GridCAT. For more detailed information about these settings, please refer to the SPM manual.

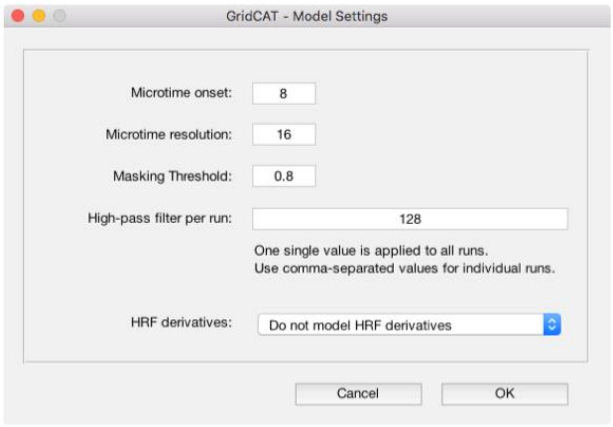

1. Microtime onset is the reference time-bin at which the regressors are resampled to coincide with data acquisition. If you have performed slice-timing correction, you must change this parameter to match the reference slice specified there. Otherwise, you might still want to change this if you have non-interleaved acquisition and you wish to sample the regressors so that they are appropriate for a slice in a particular part of the brain.

2. Microtime resolution is the number of time-bins per scan used when building regressors. If you have performed slice-timing correction, change this parameter to match the number of slices specified there; otherwise, you would typically not need to change this.

3. Masking threshold: By default, SPM uses a proportional threshold to identify these voxels that seem to carry a decent signal in them. If a voxel fails to exceed this threshold (e.g., voxels outside the brain), it will not contribute to the output of a GLM. For example, a masking threshold of 0.8 will only estimate the GLM in voxels whose mean value is at least 80% of the global signal.

4. High-pass filter: Slow signal drifts within a period longer than the value specified here will be removed. Either input one single value, which will be applied for all runs, or input one value per run, separated by commas.

5. HRF derivatives: The canonical HRF combined with time and dispersion derivatives comprise an “informed” basis set, as the shape of the canonical response conforms to the hemodynamic response that is commonly observed. The incorporation of the derivate terms allow for variations in subject-to-subject and voxel-to-voxel responses. The time derivative allows the peak response to vary by plus or minus a second and the dispersion derivative allows the width of the response to vary.

Appendix 2:
Computational modeling details

Participants report their location estimates only at stopping points between path segments. Before we can fit the internal and reporting noise parameters to those estimates we first need to integrate the stochastic differential equation (1) along segments, a calculation that can be performed analytically because eq. (1) describes an Ornstein-Uhlenbeck process (Uhlenbeck & Ornstein, 1930; Pavliotis, 2014) Assuming that participants walk along a trajectory segment for time t with constant velocity $\mathbf{v}$, the conditional distribution of the internal location estimate $\hat{\boldsymbol{x}}_{s+1}$ at the stopping point $s+1$ given the estimate at the previous stopping point $\hat{\boldsymbol{x}}_s$ is given by the Gaussian distribution

$$p(\hat{\boldsymbol{x}}_{s+1}|\hat{\boldsymbol{x}}_s) = \mathcal{N}(\hat{\boldsymbol{x}}_{s+1}|\boldsymbol{\mu}_{s+1}, \sigma_{s+1}^2 I_2)$$

where I_2 is the two-dimensional unity matrix and mean $\boldsymbol{\mu}_{s+1}$ and variance σ_{s+1}^2 are given by

Eq. (3)

$$\boldsymbol{\mu}_{s+1} = \hat{\boldsymbol{x}}_s e^{-\beta t} + \frac{a\mathbf{v} + \mathbf{b}}{\beta}\left(1 - e^{-\beta t}\right)$$

$$\sigma_{s+1}^2 = \frac{\sigma_0^2}{2\beta}\left(1 - e^{-2\beta t}\right)$$

This update equation for the distribution of internal estimates can also be expressed in terms of the true length $|\Delta\mathbf{x}|$ of the trajectory segment:

Eq. (4)

$$\boldsymbol{\mu}_{s+1} = \hat{\boldsymbol{x}}_s e^{-\tilde{\beta}|\Delta\mathbf{x}|} + \left(\alpha\frac{\Delta\mathbf{x}}{|\Delta\mathbf{x}|} + \tilde{\mathbf{b}}\right)\frac{1}{\tilde{\beta}}\left(1 - e^{-\tilde{\beta}|\Delta\mathbf{x}|}\right)$$

$$\sigma_{s+1}^2 = \frac{\tilde{\sigma}_0^2}{2\tilde{\beta}}\left(1 - e^{-2\tilde{\beta}|\Delta\mathbf{x}|}\right)$$

where we have redefined 3 of the 4 internal error parameters using the magnitude of the walking velocity $|\mathbf{v}|$:

Eq. (5)

$$\tilde{\beta} = \frac{\beta}{|\mathbf{v}|} \qquad \tilde{\mathbf{b}} = \frac{\mathbf{b}}{|\mathbf{v}|} \qquad \tilde{\sigma}_0^2 = \frac{\sigma_0^2}{|\mathbf{v}|}$$

Equations (3) and (4) are equivalent if the walking velocity $|\mathbf{v}|$ is truly constant across trajectory segments and trials. If the walking velocity does vary, holding the transformed parameters (5) fixed assumes that the path integration error of the internal location estimate mainly depends on the traveled *distance*, whereas the original model (3)

assumes that the path integration error mainly depends on the elapsed walking *time*. In what follows, we will choose the *distance* model and hold the transformed parameters (5) fixed, in line with previous modeling of human path integration (Lappe et al., 2007, 2011).

Fitting model parameters without reporting noise

In the following we explain how the internal error parameters $\theta = (\tilde{\beta}, \alpha, \tilde{\mathbf{b}}, \tilde{\sigma}_0^2)$ and the reporting noise parameters $\kappa = (\sigma_d^2, \sigma_\phi^2)$ were fit to participants' reports by maximizing the likelihood. For simplicity, consider first a model without reporting noise parameters. In this case the internal location estimate $\hat{\boldsymbol{x}}_s$ can be directly expressed in terms of participants' report of the distance $\hat{d}$ and angle $\hat{\varphi}$ to the starting point $\mathbf{x}_{\text{start}}$ of the current walking trajectory:

Eq. (6)

$$\hat{\mathbf{x}}_s = \begin{pmatrix} \hat{d}\cos(\hat{\varphi}) \\ \hat{d}\sin(\hat{\varphi}) \end{pmatrix} + \mathbf{x}_{\text{start}}$$

Without loss of generality we will set the origin at the starting point for each trial, hence $\mathbf{x}_{\text{start}} = 0$. The log-likelihood of the data as a function of the internal error parameters averaged over trials is given by

Eq. (7)

$$\mathrm{LL}_{\kappa=0}(\theta) = \langle \sum_{s=0}^{3} \log p(\hat{\boldsymbol{x}}_{s+1} | \hat{\boldsymbol{x}}_s ; \theta) \rangle_{trials} = \langle \sum_{s=0}^{3} \log \mathcal{N}(\hat{\boldsymbol{x}}_{s+1} |\, \boldsymbol{\mu}_{s+1}(\hat{\boldsymbol{x}}_s, \theta), \sigma_{s+1}^2(\theta)) \rangle_{trials}$$

where $\boldsymbol{\mu}_{s+1}(\hat{\boldsymbol{x}}_s, \theta)$ and $\sigma_{s+1}^2(\theta)$ are given by the expressions in eq. (4). We can then fit θ to the data by maximizing the log-likelihood numerically:

Eq. (8)

$$\theta_{\mathrm{ML}} = \mathrm{argmax}_\theta \mathrm{LL}_{\kappa=0}(\theta)$$

Fitting model parameters with reporting noise

In the presence of non-zero reporting noise parameters the expression for the log-likelihood as a function of $\Theta = (\theta, \kappa)$ is more involved, since the relationship between the reported estimates $\hat{d}$ and $\hat{\varphi}$ and the internal location estimate $\hat{\boldsymbol{x}}_s$ is both stochastic and non-linear. We can nevertheless make progress by rephrasing the problem in terms of the well-studied Extended Kalman Filter (EKF), a framework that allows to calculate the log-likelihood by locally linearizing the non-linearities (Thrun et al., 2005). The EKF framework encompasses a stochastic state transition of a hidden variable $\hat{\boldsymbol{x}}_s$ whose distribution can be inferred using a noisy observation z_s:

Eq. (9)

$$\hat{\boldsymbol{x}}_{s+1} = \mathrm{f}(\hat{\boldsymbol{x}}_s) + \Sigma_x^{\frac{1}{2}}\boldsymbol{\xi}_{\boldsymbol{x}}$$

$$\mathbf{z}_{\mathrm{s}+1} = \mathrm{h}(\hat{\boldsymbol{x}}_{s+1}) + \Sigma_z^{\frac{1}{2}}\boldsymbol{\xi}_{\boldsymbol{z}}$$

where f and h are arbitrary non-linear functions and Σ_{x} and Σ_{x} are covariance matrices of Gaussian-distributed noise. In our case the state transition is linear in $\hat{\boldsymbol{x}}_s$ and is given as before by eq. (4):

Eq. (10)

$$\mathrm{f}(\hat{\boldsymbol{x}}_s) = \boldsymbol{\mu}_{\mathrm{s}+1}(\hat{\boldsymbol{x}}_s) = \hat{\boldsymbol{x}}_s \mathrm{e}^{-\tilde{\beta}|\Delta\mathbf{x}|} + \left(\alpha\frac{\Delta\mathbf{x}}{|\Delta\mathbf{x}|} + \tilde{\mathrm{b}}\right)\frac{1}{\tilde{\beta}}\left(1 - \mathrm{e}^{-\tilde{\beta}|\Delta\mathbf{x}|}\right)$$

$$\Sigma_{\mathrm{x}} = \sigma_{\mathrm{s}+1}^2 \mathrm{I}_2 = \frac{\tilde{\sigma}_0^2}{2\tilde{\beta}}\left(1 - \mathrm{e}^{-2\tilde{\beta}|\Delta\mathbf{x}|}\right)\mathrm{I}_2$$

To derive the non-linear observation function we need to find a coordinate transformation such that in the transformed frame the noise is added linearly. According to eq. (2), the noise is added linearly in log-polar coordinates. The observation function $\mathrm{h}(\hat{\boldsymbol{x}}_{s+1})$ therefore corresponds to the transformation from cartesian to log-polar coordinates:

Eq. (11)

$$\mathrm{h}(\hat{\boldsymbol{x}}_{s+1}) = \begin{pmatrix} d(\hat{\boldsymbol{x}}_{s+1}) \\ \varphi(\hat{\boldsymbol{x}}_{s+1}) \end{pmatrix} = \begin{pmatrix} log|\hat{\boldsymbol{x}}_{s+1}| \\ atan2((\hat{\boldsymbol{x}}_{s+1})_2, (\hat{\boldsymbol{x}}_{s+1})_1) \end{pmatrix}$$

$$\Sigma_{\mathrm{z}} = \begin{pmatrix} \sigma_{\mathrm{d}}^2 & 0 \\ 0 & \sigma_{\varphi}^2 \end{pmatrix}$$

and the observation $\mathbf{z}_{\mathrm{s}+1}$ is related to the reports $\hat{d}$ and $\hat{\varphi}$ by

Eq. (12)

$$\mathbf{z}_{\mathrm{s}+1} = \begin{pmatrix} log\ \hat{d} \\ \hat{\varphi} \end{pmatrix}$$

The EKF framework allows calculating two important distributions using Gaussian approximations: the posterior distribution of the hidden variable $\hat{\boldsymbol{x}}_{s+1}$ given the observations z_1 to z_{s} (predictive distribution), and the posterior distribution of $\hat{\boldsymbol{x}}_{s+1}$ given z_1 to $\mathrm{z}_{\mathrm{s}+1}$ (updated distribution). We denote the mean and covariance of these posterior distributions as

Eq. (13)

$$\mathrm{p}(\hat{\boldsymbol{x}}_{s+1}|\mathrm{z}_1, \ldots, \mathrm{z}_{\mathrm{s}}) = \mathcal{N}\left(\hat{\boldsymbol{x}}_{s+1}\middle|\boldsymbol{\mu}_{\mathrm{s}+1|\mathrm{s}}, P_{s+1|s}\right) \qquad \text{(predictive distribution)}$$

$$\mathrm{p}(\hat{\boldsymbol{x}}_{s+1}|\mathrm{z}_1,\ldots,\mathrm{z}_{s+1}) = \mathcal{N}(\hat{\boldsymbol{x}}_{s+1}|\boldsymbol{\mu}_{s+1|s+1}, P_{s+1|s+1}) \qquad \text{(updated distribution)}$$

Mean and covariance of both distributions can be calculated recursively over stopping points using the standard EKF update equations (Thrun et al., 2005):

Eq. (14)

$$\boldsymbol{\mu}_{s+1|s} = \mathrm{f}(\boldsymbol{\mu}_{s|s})$$

$$P_{s+1|s} = \mathrm{F}_{s+1} P_{s|s} F_{s+1}^T + \Sigma_x$$

$$\mathrm{S}_{s+1} = H_{s+1} P_{s+1|s} H_{s+1}^T + \Sigma_z$$

$$\mathrm{K}_{s+1} = P_{s+1|s} H_{s+1}^T S_{s+1}^{-1}$$

$$\boldsymbol{\mu}_{s+1|s+1} = \boldsymbol{\mu}_{s+1|s} + \mathrm{K}_{s+1}(\mathbf{z}_{s+1} - h(\boldsymbol{\mu}_{s+1|s}))$$

$$P_{s+1|s+1} = (I_2 - \mathrm{K}_{s+1} H_{s+1}) P_{s+1|s}$$

where the matrices F_{s+1} and H_{s+1} are the Jacobian matrices of transition and observation function evaluated at the previous updated mean $\boldsymbol{\mu}_{s|s}$ and predictive mean $\boldsymbol{\mu}_{s+1|s}$ respectively:

Eq. (15)

$$\mathrm{F}_{s+1} = \left.\frac{\partial \mathrm{f}(\boldsymbol{x})}{\partial \boldsymbol{x}}\right|_{\mathbf{x}=\boldsymbol{\mu}_{s|s}} = \mathrm{e}^{-\tilde{\beta}|\Delta \mathbf{x}|} I_2$$

$$\mathrm{H}_{s+1} = \left.\frac{\partial \mathrm{h}(\boldsymbol{x})}{\partial \mathbf{x}}\right|_{\mathbf{x}=\boldsymbol{\mu}_{s+1|s}} = \frac{1}{|\boldsymbol{\mu}_{s+1|s}|^2} \begin{pmatrix} \mu_{s+1|s,1} & \mu_{s+1|s,2} \\ -\mu_{s+1|s,2} & \mu_{s+1|s,1} \end{pmatrix}$$

At the starting point ($\mathrm{s} = 0$), we initialize $\boldsymbol{\mu}_{s=0|s=0} = \mathbf{x}_{\mathrm{start}} = 0$ and $P_{s=0|s=0} = 0$. Next, we calculate the predicted distribution of the next measurement z_{s+1} given the previous measurements z_1 to z_s by integrating out the internal estimate $\hat{\boldsymbol{x}}_{s+1}$:

Eq. (16)

$$\mathrm{p}(\mathrm{z}_{s+1}|\mathrm{z}_1,\ldots,\mathrm{z}_s) = \int d\,\hat{\boldsymbol{x}}_{s+1} p(\mathrm{z}_{s+1}|\hat{\boldsymbol{x}}_{s+1}) p(\hat{\boldsymbol{x}}_{s+1}|\mathrm{z}_1,\ldots,\mathrm{z}_s)$$

$$= \int d\hat{\boldsymbol{x}}_{s+1}\ \mathcal{N}(\mathrm{z}_{s+1}|h(\hat{\boldsymbol{x}}_{s+1}), \Sigma_z) \mathcal{N}(\hat{\boldsymbol{x}}_{s+1}|\boldsymbol{\mu}_{s+1|s}, P_{s+1|s})$$

$$\approx \int d\hat{\boldsymbol{x}}_{s+1}\ \mathcal{N}(\mathrm{z}_{s+1}|h(\boldsymbol{\mu}_{s+1|s}) + \mathrm{H}_{s+1}(\hat{\boldsymbol{x}}_{s+1} - \boldsymbol{\mu}_{s+1|s}), \Sigma_z) \mathcal{N}(\hat{\boldsymbol{x}}_{s+1}|\boldsymbol{\mu}_{s+1|s}, P_{s+1|s})$$

$$= \mathcal{N}(\mathrm{z}_{s+1}|h(\boldsymbol{\mu}_{s+1|s}), \mathrm{S}_{s+1})$$

where we have used the linearization approximation of the EKF at the 3rd line. This allows us to express the full log-likelihood as:

Eq. (17)

$$\mathrm{LL}(\Theta) = \langle \sum_{s=0}^{3} \log \mathrm{p}(\mathrm{z}_{s+1}|\mathrm{z}_1, \ldots, \mathrm{z}_s\,; \Theta) \rangle_{trials}$$

where the dependency on the parameters Θ is introduced through f, its Jacobian F_{s+1}, Σ_x and Σ_z. In analogy to (8), we find the maximum likelihood (ML) estimate for Θ by numerically maximizing the log-likelihood:

$$\Theta_{\mathrm{ML}} = \mathrm{argmax}_{\Theta} \mathrm{LL}(\Theta)$$

Numerical parameter optimization was performed using the fminunc-function of MATLAB's optimization toolbox.

Incorporating trials without participant responses at intermediate stopping points

For a fraction of the trials, a response is not collected at intermediate stopping points, but only at the end of the trajectory. For these trials the observations $\mathbf{z}_{s+1}$ are missing for $s \in \{0,1,2\}$ and therefore the EKF update equations (14) need to be adapted. This can be achieved using the infinite observation noise limit $\Sigma_\mathrm{z} \to \infty$, under which the predicted and updated posterior distributions become identical:

$$\boldsymbol{\mu}_{s+1|s} = \mathrm{f}(\boldsymbol{\mu}_{s|s})$$

$$P_{s+1|s} = \mathrm{F}_{s+1} P_{s|s} F_{s+1}^T + \Sigma_x$$

$$\boldsymbol{\mu}_{s+1|s+1} = \boldsymbol{\mu}_{s+1|s}$$

$$P_{s+1|s+1} = P_{s+1|s}$$

For $\mathrm{s} = 3$, the observation at the last stopping point $\mathbf{z}_{s+1}$ is defined, and eq. (14) can be used as usual.

Model predictions

We simulated participants' responses by sampling 100 repetitions of model trajectories for each participant and trial from eq. (9) given the fitted parameters $\Theta = \Theta_{\mathrm{ML}}$ and the trajectory parameters $\Delta\mathbf{x}$ for each segment. Each repetition generates stochastic observations $\hat{\mathrm{d}}_{\mathrm{model}}$ and $\hat{\varphi}_{\mathrm{model}}$ via eq. (12) that can be analyzed analogously to the actual data. The model prediction for the square error is calculated by averaging the square error of the simulated data over trials and repetitions. The model prediction for

the bias on individual trials is calculated by averaging the simulated data over repetitions.

Model variants

No reporting noise: The log-likelihood is computed using eq. (7) instead of eq. (17).

Constant reporting noise: This model assumes that the distance reporting error does not follow Weber's law but is independent of the distance reporting value. For this model eq. (2) is replaced by

Eq. (18)

$$\hat{\mathrm{d}} = \mathrm{d} + \sigma_{\mathrm{d}}\eta_{\mathrm{d}}$$

$$\hat{\varphi} = \varphi + \sigma_{\varphi}\eta_{\varphi}$$

The model can be fit in the same way as Weber reporting noise model, with the first component of the observation $\mathbf{z}_{\mathrm{s}}$ defined as the reported distance $\hat{\mathrm{d}}$, instead of its logarithm $\log(\hat{\mathrm{d}})$. In this model, noise is added linearly in polar coordinates instead of log-polar coordinates. Therefore, eq. (12) is replaced by

Eq. (19)

$$\mathbf{z}_{\mathrm{s+1}} = \begin{pmatrix} \hat{d} \\ \hat{\varphi} \end{pmatrix}$$

and we replace the observation function $\mathrm{h}(\hat{\boldsymbol{x}}_{s+1})$ in eq. (11) by the transformation from cartesian to polar coordinates:

Eq. (20)

$$\mathrm{h}(\hat{\boldsymbol{x}}_{s+1}) = \begin{pmatrix} d(\hat{\boldsymbol{x}}_{s+1}) \\ \varphi(\hat{\boldsymbol{x}}_{s+1}) \end{pmatrix} = \begin{pmatrix} |\hat{\boldsymbol{x}}_{s+1}| \\ atan2((\hat{\boldsymbol{x}}_{s+1})_2, (\hat{\boldsymbol{x}}_{s+1})_1) \end{pmatrix}$$

and its Jacobian H_{s+1} in eq. (15) by

$$\mathrm{H}_{\mathrm{s+1}} = \left.\frac{\partial \mathrm{h}(\boldsymbol{x})}{\partial \mathbf{x}}\right|_{\mathbf{x}=\boldsymbol{\mu}_{s+1|s}} = \frac{1}{|\boldsymbol{\mu}_{s+1|s}|^2} \begin{pmatrix} \mu_{s+1|s,1}|\boldsymbol{\mu}_{s+1|s}| & \mu_{s+1|s,2}|\boldsymbol{\mu}_{s+1|s}| \\ -\mu_{s+1|s,2} & \mu_{s+1|s,1} \end{pmatrix}$$

The rest of the calculation of the log-likelihood function is exactly the same as for the Weber-law reporting noise model.

Fitting by age group: Instead of fitting model parameters individually for each participant, participants in each age group are constrained to have the same model parameters.

Model comparison using Bayesian Information Criterion

The Bayesian Information Criterion (BIC) is a scheme to compare models with different numbers of parameters: models with lower BIC are preferred over models with higher BIC (Konishi & Kitagawa, 2008). The BIC corrects for the higher expressibility of models with larger number of parameters using an additive compensation term. The formula for the BIC is given by

$$\mathrm{BIC} = -2\,\mathrm{LL}(\Theta_{ML}) + \log(\mathrm{n})\mathrm{k}$$

where n is the number of observations and k is the number of parameters. The number of parameters for different models is given by:

Model	**Number of parameters k**
Weber model, individually fit, young adults	7 x n = 210
Weber model, individually fit, older adults	7 x n = 182
Weber model, group-level fit	7
Constant noise model, individually fit, young adults	7 x n = 210
Constant noise model, individually fit, older adults	7 x n = 182
No reporting noise model, individually fit, young adults	7 x n = 210
No reporting noise model, individually fit, older adults	7 x n = 182

Relative influence of model parameters on predicted square error

The detailed computational model allows us to measure the influence of each type of bias and noise parameter on the square error predicted by the model. For each parameter type we calculated a reduced square error that is generated by setting this parameter type to its ideal value corresponding to unbiased, noiseless integration, while keeping the remaining parameters at their ML estimates:

- $\mathrm{error}^2_{\tilde{\beta}} = \mathrm{error}^2(\tilde{\beta} = 0, \alpha_{ML}, \tilde{\mathbf{b}}_{ML}, \tilde{\sigma}^2_{0\,ML}, \sigma^2_{d\,ML}, \sigma^2_{\phi\,ML})$
- $\mathrm{error}^2_{\alpha} = \mathrm{error}^2(\tilde{\beta}_{ML}, \alpha = 1, \tilde{\mathbf{b}}_{ML}, \tilde{\sigma}^2_{0\,ML}, \sigma^2_{d\,ML}, \sigma^2_{\phi\,ML})$
- $\mathrm{error}^2_{\tilde{\mathbf{b}}} = \mathrm{error}^2(\tilde{\beta}_{ML}, \alpha_{ML}, \tilde{\mathbf{b}} = 0, \tilde{\sigma}^2_{0\,ML}, \sigma^2_{d\,ML}, \sigma^2_{\phi\,ML})$
- $\mathrm{error}^2_{\tilde{\sigma}^2_0} = \mathrm{error}^2(\tilde{\beta}_{ML}, \alpha_{ML}, \tilde{\mathbf{b}}_{ML}, \tilde{\sigma}^2_0 = 0, \sigma^2_{d\,ML}, \sigma^2_{\phi\,ML})$
- $\mathrm{error}^2_{\sigma^2_d} = \mathrm{error}^2(\tilde{\beta}_{ML}, \alpha_{ML}, \tilde{\mathbf{b}}_{ML}, \tilde{\sigma}^2_{0\,ML}, \sigma^2_d = 0, \sigma^2_{\phi\,ML})$
- $\mathrm{error}^2_{\sigma^2_\phi} = \mathrm{error}^2(\tilde{\beta}_{ML}, \alpha_{ML}, \tilde{\mathbf{b}}_{ML}, \tilde{\sigma}^2_{0\,ML}, \sigma^2_{d\,ML}, \sigma^2_\phi = 0)$

The relative influence of each reduced error in percent is then calculated as:

$$\mathrm{infl}_\mathrm{i} = 100\,\frac{\mathrm{error}^2(\Theta_\mathrm{ML}) - \mathrm{error}^2_\mathrm{i}}{\mathrm{error}^2(\Theta_\mathrm{ML})}$$

Note that the relative influence can be negative if the reduced square error is larger than the square error of the full model. This can be true in particular for the memory leak parameter $\tilde{\beta}$: For example, a memory leak value $\tilde{\beta}_{ML} < 1$ that draws location estimates towards the starting point can partly compensate for a velocity bias $\alpha_{ML} > 1$ that draws location estimates away from the starting point. Setting $\tilde{\beta} = 1$ while keeping $\alpha_{ML} > 1$ can therefore lead to a larger "reduced" square error and a negative relative influence.

Also note that due to the nonlinearity of the model the relative influences do not have to sum to 100%.

LIST OF ABBREVIATIONS

BIC	Bayesian information criterion
BMBF	German ministry of education and research
BOLD	blood oxygenation level dependent
DSST	digit symbol substitution test
EKF	extended Kalman filter
EPI	echo-planar imaging
Eq	equation(s)
fMRI	functional magnetic resonance imaging
FWHM	full width at half maximum
GLM	general linear model
GRAPPA	generalized autocalibrating partial parallel acquisition
GridCAT	grid code analysis toolbox
GUI	graphical user interface
HMD	head mounted display
HRF	hemodynamic response function
M	mean
m	meter(s)
MCI	mild cognitive impairment
mm	millimeter(s)
MoCA	Montreal cognitive assessment
MPRAGE	magnetization-prepared rapid gradient-echo
ms	millisecond(s)
MST	medial superior temporal
MVPA	multi-voxel pattern analysis
NIfTI	neuroimaging informatics technology initiative
NITRC	neuroimaging informatics tools and resources clearinghouse
NMDA	N-methyl-D-aspartate receptor
PET	positron emission tomography
ROI	region of interest
RSA	representational similarity analysis
SBSOD	Santa Barbara sense of direction scale
SD	standard deviation
sec	second(s)
SEM	standard error of the mean
SPM	statistical parametric mapping
TAP	testbattery for attentional performance
TE	echo time
TI	inversion time
TR	repetition time
TSE	turbo-spin-echo
tSNR	temporal signal-to-noise ratio
vm	virtual meter(s)
vol	volume
WAIS	Wechsler adult intelligence scale
2D	two-dimensional
3D	three-dimensional
>>	... is much greater than ...
Δ	difference
#	number(s)
°	degree(s)

DECLARATION / ERKLÄRUNG

I herewith declare that this thesis entitled “Investigating human grid-cell-like representations and path integration in the context of cognitive aging” is the result of my own independent work/investigation, except where otherwise stated. Other sources are acknowledged by explicit references. Additionally, this work has not been submitted in substance for any other degree or award at this or any other university or place of learning, nor is being submitted concurrently in candidature for any degree or other award.

Hiermit erkläre ich, dass ich die von mir eingereichte Dissertation zum Thema “Investigating human grid-cell-like representations and path integration in the context of cognitive aging” selbständig verfasst, nicht bereits als Dissertation verwendet habe und die benutzten Hilfsmittel und Quellen vollständig angegeben wurden. Weiterhin erkläre ich, dass ich weder diese noch eine andere Arbeit zur Erlangung des akademischen Grades doctor rerum naturalium (Dr. rer. nat.) an anderen Einrichtungen eingereicht habe.

Magdeburg, 19.6.2018

Matthias Stangl